# Turbulent boundary layer separation and control

by

Ola Lögdberg

December 2008
Technical Reports from
Royal Institute of Technology
KTH Mechanics
SE-100 44 Stockholm, Sweden

Akademisk avhandling som med tillstånd av Kungliga Tekniska Högskolan i Stockholm framlägges till offentlig granskning för avläggande av teknologie doktorsexamen fredagen den 23 januari 2009 kl 10.15 i F3, Kungliga Tekniska Högskolan, Lindstedtsvägen 26, Stockholm. ©Ola Lögdberg 2008 Universitetsservice US-AB, Stockholm 2008

Ola Lögdberg 2008, **Turbulent boundary layer separation and control** Linné Flow Centre, KTH Mechanics, SE-100 44 Stockholm, Sweden

#### Abstract

Boundary layer separation is an unwanted phenomenon in most technical applications, as for instance on airplane wings, ground vehicles and in internal flow systems. If separation occurs, it causes loss of lift, higher drag and energy losses. It is thus essential to develop methods to eliminate or delay separation.

In the present experimental work streamwise vortices are introduced in turbulent boundary layers to transport higher momentum fluid towards the wall. This enables the boundary layer to stay attached at larger pressure gradients. First the adverse pressure gradient (APG) separation bubbles that are to be eliminated are studied. It is shown that, independent of pressure gradient, the mean velocity defect profiles are self-similar when the scaling proposed by Zagarola and Smits is applied to the data. Then vortex pairs and arrays of vortices of different initial strength are studied in zero pressure gradient (ZPG). Vane-type vortex generators (VGs) are used to generate counter-rotating vortex pairs, and it is shown that the vortex core trajectories scale with the VG height h and the spanwise spacing of the blades. Also the streamwise evolution of the turbulent quantities scale with h. As the vortices are convected downstream they seem to move towards a equidistant state, where the distance from the vortex centres to the wall is half the spanwise distance between two vortices. Yawing the VGs up to 20° do not change the generated circulation of a VG pair. After the ZPG measurements, the VGs where applied in the APG mentioned above. It is shown that that the circulation needed to eliminate separation is nearly independent of the pressure gradient and that the streamwise position of the VG array relative to the separated region is not critical to the control effect. In a similar APG jet vortex generators (VGJs) are shown to as effective as the passive VGs. The ratio VR of jet velocity and test section inlet velocity is varied and a control effectiveness optimum is found for VR = 5. At 40° yaw the VGJs have only lost approximately 20 % of the control effect. For pulsed VGJs the pulsing frequency, the duty cycle and VR were varied. It was shown that to achieve maximum control effect the injected mass flow rate should be as large as possible, within an optimal range of jet VRs. For a given injected mass flow rate, the important parameter was shown to be the injection time  $t_1$ . A non-dimensional injection time is defined as  $t_1^+ = t_1 U_{jet}/d$ , where d is the jet orifice diameter. Here, the optimal  $t_1^+$  was 100–200.

**Descriptors:** Flow control, adverse pressure gradient (APG), flow separation, vortex generators, jet vortex generators, pulsed jet vortex generators.

#### Preface

This doctoral thesis in fluid mechanics is a paper-based thesis of experimental character. The subject of the thesis is turbulent boundary layer separation control by means of longitudinal vortices. The thesis is divided into two parts in where the first part is an overview and summary of the present contribution to the field of fluid mechanics. The second part consists of five papers, which are adjusted to comply with the present thesis format for consistency. In chapter 7 of the first part in the thesis the respondent's contribution to all papers are stated.

December 2008, Stockholm  $Ola\ L\ddot{o}gdberg$ 

# Contents

Abstract	iii
Preface	iv
Part I. Overview and summary	
Chapter 1. Introduction	1
1.1. Truck aerodynamics	2
1.2. Research outline	6
Chapter 2. Separation	7
2.1. The separated region	7
2.2. The Zagarola-Smits velocity scale	9
Chapter 3. Vane-type vortex generators	13
3.1. Vane-type VGs in ZPG	13
3.2. Vane-type VGs in APG	19
Chapter 4. Jet vortex generators	23
4.1. Steady jet VGs	23
4.2. Pulsed jet VGs	27
Chapter 5. Conclusions	31
5.1. The separated region	31
5.2. Vane-type VGs	31
5.3. Jet VGs	32
Chapter 6. Outlook	33
6.1. Practical applications	33
6.2. Further research	33
Chapter 7. Papers and authors contributions	35

Ack	knowledgements	38
Ref	erences	39
Par	t II. Papers	
1.	On the scaling of turbulent separating boundary layers	47
2.	Streamwise evolution of longitudinal vortices in a turbulent boundary layer	61
3.	On the robustness of separation control by streamwise vortices	105
4.	Separation control by an array of vortex generator jets. Part 1. Steady jets.	129
5.	Separation control by an array of vortex generator jets. Part 2. Pulsed jets.	159

# $\begin{array}{c} {\bf Part\ I} \\ {\bf Overview\ and\ summary} \end{array}$

#### CHAPTER 1

## Introduction

With the increase in oil prices and the increased environmental concerns, regarding both toxic exhausts, particulates and green house gases, the reduction of fuel consumption is an important issue both for vehicle manufactures and those who utilise the vehicles. Large improvements have been made over the last decades in terms of engine efficiency, aerodynamic drag etc. but there is still possibilities for future improvements. This thesis deals with a fundamental aerodynamic problem, namely how to control flow separation, a phenomenon that in most cases lead to increased aerodynamic drag. The results may be useful in many engineering situations, but the work is motivated by the possibility to reduce the aerodynamic drag on long haulage trucks.



FIGURE 1.1. The author performing a smoke visualisation on a Scania truck in the German-Dutch LLF wind tunnel in 2001. The largest test section, with a cross sectional area of  $9.5~\mathrm{m} \times 9.5~\mathrm{m}$  is used for this test.

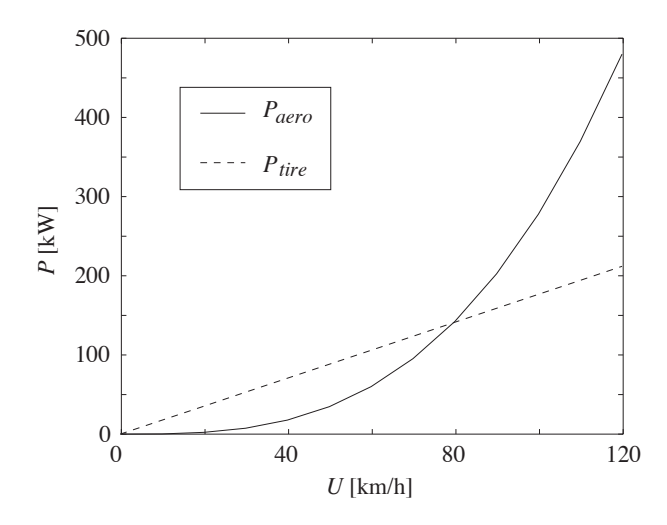


FIGURE 1.2. The engine power needed to overcome aerodynamic drag  $P_{aero}$  and tire rolling resistance  $P_{tire}$ . To produce this approximate plot the coefficients of wind averaged drag and rolling resistance were assumed to be  $C_{D,wa} = 0.6$  and  $f_r = 0.0045$ .

#### 1.1. Truck aerodynamics

The aerodynamic drag is an important part of the total average tractive resistance of a long-haulage truck. A heavy truck (for example the Scania Rseries truck shown in figure 1.1), with warm low resistance tires, at a speed  $U_x = 80 \text{ km/h}$  on a flat dry road has a rolling resistance which is approximately 50% of the total tractive resistance. The remaining 50% is aerodynamic drag. The rolling resistance coefficient  $f_r$  is known to be almost independent of the speed and therefore the drag caused by the tires increases linearly with the speed  $(F_{x,tire} = f_r U_x)$ . Also the aerodynamic drag coefficient  $(C_D)$  is fairly independent of the speed for a truck, which means that the aerodynamic drag  $F_{x,aero} = \frac{1}{2}\rho C_D U_x^2$ , where  $\rho$  is the density of the fluid, increases quadratically with the speed. At speeds above approximately 80 km/h the contribution of the aerodynamic drag to the total drag overshadows that of the tires, as can be seen i figure 1.2.

The analysis above is however oversimplified, since very few long haulage routes in the real world are completely flat. Furthermore, vehicles occasionally have to slow down or even stop. Therefore it is necessary to take into account both "hill climbing" and acceleration. According to simulations performed by the author the aerodynamic drag constitutes around 30% of the total drag on moderately hilly long haulage routes, like Stockholm-Helsingborg. This is for a

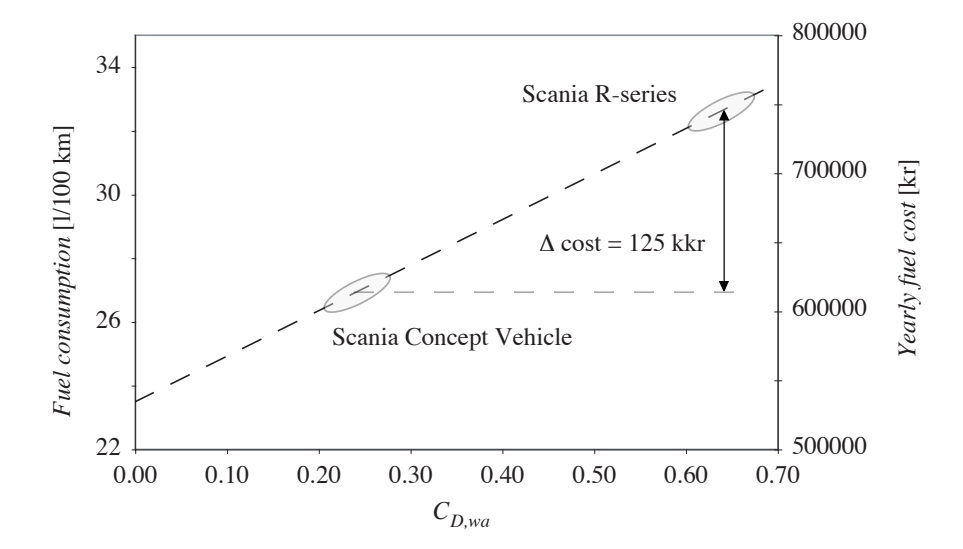


FIGURE 1.3. Fuel consumption and fuel cost for a truck used in long haulage operation. The fuel cost is based on an annual mileage of 200000 km and the price of diesel oil in December 2008 (11.40 kr/l). This is a slight overestimation since all large transport companies get discounts on fuel.

truck trailer combination with a relatively smooth-sided trailer, low resistance tires and a modern 420 hp engine.

Since truck manufacturers do not develop tires and cannot change the topography (although there are systems to store brake energy), or do much about the traffic situation, aerodynamic drag is the component of the tractive resistance that is possible to reduce. Apart from the obvious environmental benefits of bringing down the fuel consumption, the economical gains are substantial. Figure 1.3 demonstrates the relation between aerodynamic drag, fuel consumption and the annual cost of fuel for a long haulage operator. The truck in figure 1.4 was developed at Scania in 1999 as a technology demonstrator and one of the main features was its low  $C_{D,wa}^{-1}$ . In figure 1.3 this concept vehicle is chosen to represent the realistic limit for aerodynamic drag reduction. The Scania R-series in figure 1.1 is typical for an aerodynamically well-designed truck of today and the span of  $C_{D,wa}$  given is a conservative estimation of the variation due to trailer choice.

<sup>&</sup>lt;sup>1</sup>Since  $C_D$  increases with yaw for a normal truck, a wind averaged drag coefficient  $C_{D,wa}$  is calculated by averaging weighted  $C_D$  measurements at different yaw angles.

#### 4 1. INTRODUCTION

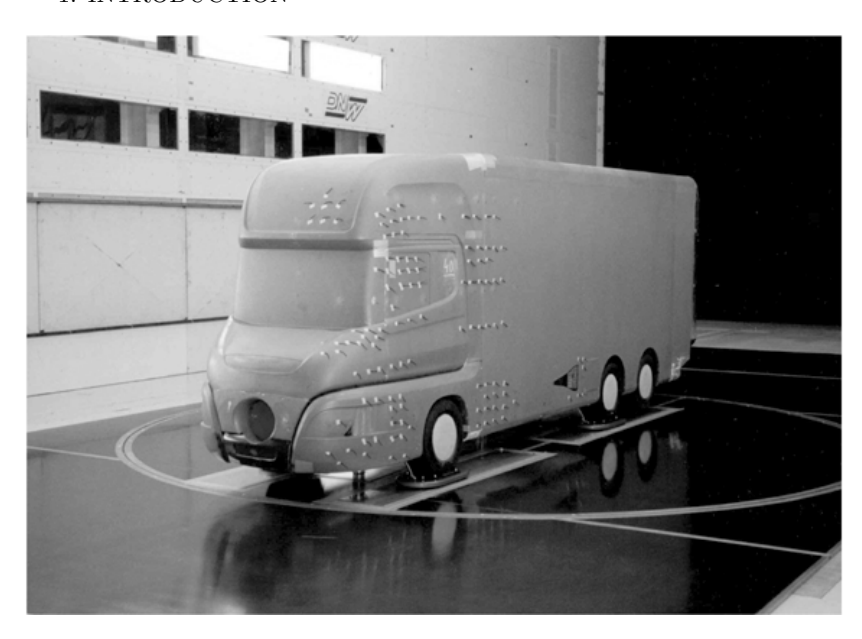


FIGURE 1.4. A Scania low drag concept truck from 1998. The shown configuration is without the accompanying trailer.

A truck is a bluff body and a major part of the drag stems from pressure, which means that friction is less important. In the beginning of time, trucks were shaped like bricks, producing massive separation all around the front. During the 70s and 80s the front of the trucks went from sharp cornered to rounded and air deflectors were fitted to the roof and the sides to smooth the transition from the cab to the body. This is illustrated as the change from (a) to (b) in figure 1.5. When the front radii are greater than 300 mm and the air deflector kit is properly designed, there are no major improvements to be made on the front. However, there are still many areas to improve on the sides, around the wheels and on the underbody, but in order to drastically reduce aerodynamic drag the separation at the end also needs to be addressed.

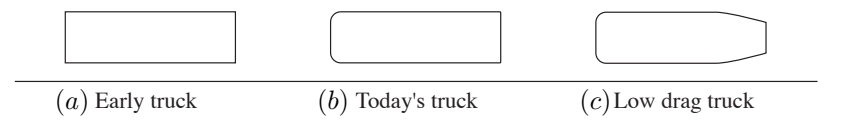


FIGURE 1.5. The aerodynamic development of trucks since the 1970s.



FIGURE 1.6. A 1 m long boat tail attached to the back end of the 1998 Scania concept truck. The tapering angle is  $15^{\circ}$  and the flow is kept attached until the cut off of the boat tail.

The conventional - and very effective - way to reduce the wake is by tapering the rear end. Aerodynamically the best thing would be a full boat tail, like on an airplane, but this would result in a vehicle of illegal length or a vehicle with very limited cargo space. Fortunately the marginal benefit decrease with length and a cut off boat tail (so called Kamm back) like in figure 1.5(c) or figure 1.6 gives much of the benefit of a full boat tail without sacrificing the possibility to actually use the truck on the road. In figure 1.6 a boat tail tested by Scania can be seen. This particular 1 m device reduced  $C_D$  about 0.10.

Unfortunately, even an elongation of only 1 m is very difficult to apply on a European long-haulage truck. This is because of the rigorous legislation on vehicle length in the European Union. Since most of the cargo is box shaped and geometrically adapted to the internal width of a trailer the tapered part must be an add-on device, or at least not a part of the effective cargo volume. Thus, a 1 m boat tail will lead to a loss of about  $3-7\,\%$  of the cargo space in a standard  $13.6\,$  m trailer.

To make a boat tail more attractive the angle must be made much larger. Hence, the air must be made to withstand a steeper pressure gradient without

 $<sup>^2\</sup>mathrm{A}$  Euro pallet is 1200×800 mm and the internal width of a trailer is approximately 2450 mm

#### 6 1. INTRODUCTION

separation. In 2001 the author performed a wind tunnel test on a boat tail, where the boundary layer was energised using slot blowing. The device was mounted on the 1:2 scale model shown in figure 1.4. With the blowing turned on the maximum non-separating tapering angle increased from 15° to 25°. Even though the concept was implemented in a very crude way the principle was shown to work. However, the energy consumption of the fans needed to supply air for the blowing slot was so high that it neutralised the gains from the drag reduction. Furthermore, the fans, valves and tubing needed not only reduces the cargo volume but impede access. Therefore, it would be desirable to find another technical solution for the separation control; one that would have a similar effect but would be easier to implement. Such a possible solution would be to use longitudinal vortices to transport high momentum fluid towards the wall.

#### 1.2. Research outline

This thesis is paper-based, but there is a common storyline.

The theme is separation control and paper 1 describes the separated region that is to be controlled. The scaling of the velocity profiles of the separated region is also discussed.

In paper 2 the use of longitudinal vortices as a flow control method is introduced. The vortices are here produced by vane-type vortex generators (VGs) and the vortex characteristics are thoroughly investigated in a zero pressure gradient (ZPG) flow.

The next step is to apply the vane-type VGs of paper 2 to control the separation bubble of paper 1. These experiments are reported in paper 3 and focus mainly on the robustness of the control method.

In paper 4 and 5 the vane-type VGs are exchanged for jet vortex generators VGJs. The same separation bubble is first controlled by steady jets in paper 4 and then with pulsed jets in paper 5.

#### CHAPTER 2

### Separation

Separation of boundary layers occurs either due to a strong adverse pressure gradient (APG) or due to a sudden change in the geometry of the surface. Typical examples of the latter is obtained where there is a sharp edge or strong curvature such as for a backward facing step, bluff bodies (typical truck geometries etc). For strong adverse pressure gradient flows along flat or mildly curved surfaces the occurrence of separation does however not only depend on the local pressure gradient but also on the local boundary layer state.

#### 2.1. The separated region

The separation point and the so called "separated region" or "separation bubble" are not well defined quantities in a turbulent boundary layer. The separation point  $x_s$  is usually defined as the point where the wall shear stress  $\tau_w = 0$ . However in a turbulent boundary layer this means that part of the time the fluctuating wall shear stress is positive and part of the time negative. Another definition of  $x_s$  uses the backflow coefficient  $(\chi)$ , i.e. the fraction of time the flow is in the backward direction. The separation point is then defined as the point on the wall where  $\chi = 0.5$ . This position does only correspond to the position where  $\tau_w = 0$  in case the probability density distribution of the fluctuating wall shear stress is symmetric around zero. The reattachment point, i.e. the position where the boundary layer reattaches to the surface (if it does), can be defined in a similar way as for the separation point. The value of the shape factor  $H_{12} = \delta_1/\delta_2$ , where  $\delta_1$  is the displacement thickness and  $\delta_2$  is the momentum loss thickness, can be used as an indication of how close the boundary layer is to separation.

The separated region can be defined as the region where the flow is recirculating in a time averaged sense. The demarcation line is hence called the dividing or separation streamline. Other definitions of the demarcation line is the contour line where the streamwise velocity is equal to zero or the contour line on which  $\chi=0.5$ . The two latter definitions usually give regions of similar size whereas the dividing streamline definition naturally gives a larger separated region.

Many papers and reviews have been written on APG separation and only a few are mentioned here for further reference. Simpson (1989) reviews the field

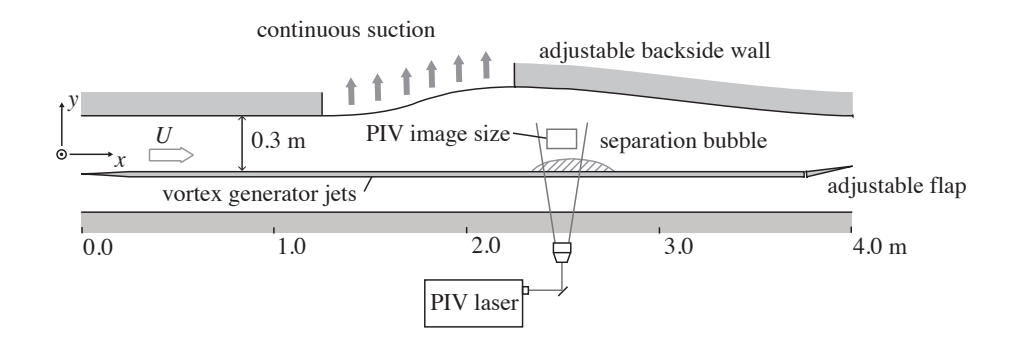


FIGURE 2.1. Schematic of the test section seen from above.

up to 1989 and also references his own extensive research. Later work was done by Fernholz and co-workers on an axisymmetric body and Kalter & Fernholz (2001) also contain an up-to-date review of the literature.

In the present work, all APG experiments were performed in the KTH BL wind-tunnel, with a free stream velocity of 26.5 m/s at the inlet of the test section. The test section, which can be seen in figure 2.1 is 4.0 m long and has a cross-sectional area of  $0.75 \text{ m} \times 0.50 \text{ m}$  (height×width). A vertical flat plate made of Plexiglas, which spans the whole height and length of the test section, is mounted with its back surface 0.3 m from the back side wall of the test section. The back side wall diverge in order to decelerate the flow and suction is applied on the curved wall to prevent separation there. The induced APG on the flat plate can be varied by adjusting the suction rate through the curved wall. All measurements are made with particle image velocimetry (PIV) and for a detailed description of the experimental set-up the reader is referred to Angele & Muhammad-Klingmann (2005a,b).

The three pressure gradients shown in figure 2.2(a) are compared in the experiment. Case I is a weak separation bubble similar to the case of Dengel & Fernholz (1990), whereas case III is the strongest APG and the strength of case II is approximately in between case I and case III. The separation bubble is here defined as the region where the backflow coefficient is  $\chi > 0.5$ . Figure 2.2(b) shows the evolution of the shape factor in the three flow cases and figure 2.3 shows the separation bubble for case II. Upstream of x=1.8 m (before separation in all cases) there are no notable differences between the cases, but the maximum value of  $H_{12}$  in the separation bubble varies between 4.1 for case I to more than 7 in case III. Furthermore, the value of  $H_{12}$  at the point of separation increases with the size of the separation bubble.

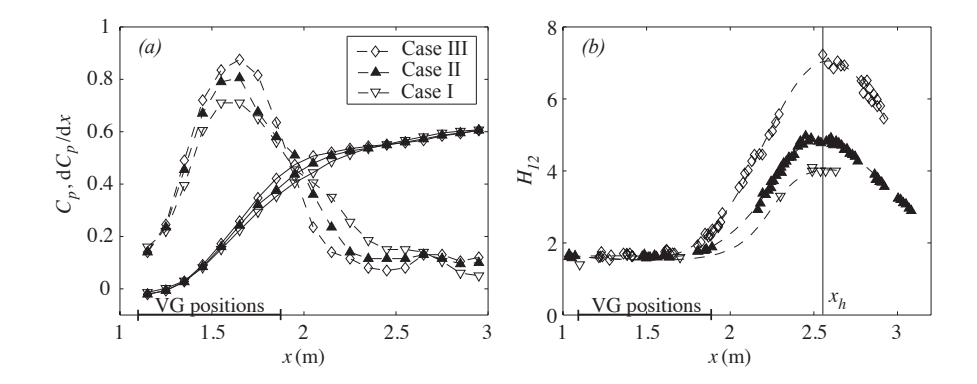


FIGURE 2.2. (a) The pressure distribution  $(C_p)$  and its gradient in the streamwise direction  $(\mathrm{d}C_p/\mathrm{d}x)$ . The region where the VGs are applied is indicated on the x-axis. (b) The shape factor.

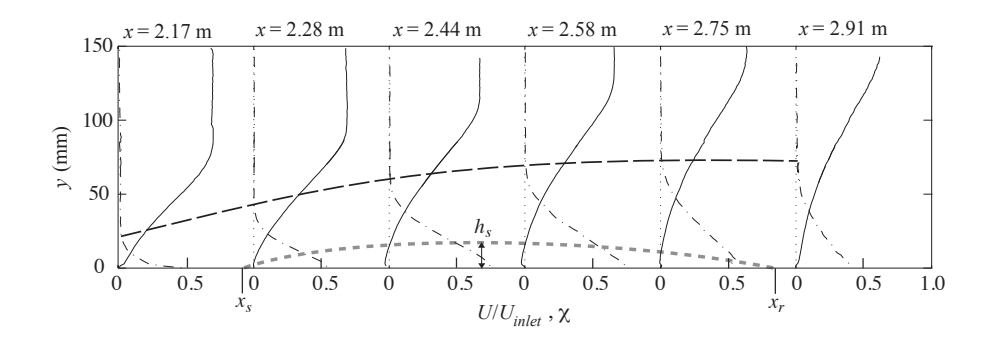


FIGURE 2.3. The separation bubble for the APG case II. The full lines show  $U/U_{inlet}$ , the dash-dotted lines show the backflow coefficient  $\chi$ . The separation bubble, defined as the region where  $\chi > 0.5$ , is the area below the lower dashed line. The region of  $\chi > 0$  is below the higher dashed line.

#### 2.2. The Zagarola-Smits velocity scale

There is still no consensus on the proper mean velocity scaling of the outer region in a strong APG and separated turbulent boundary layers. According to Townsend (1961), the criterion for similarity to exist in the mean velocity profile is that the ratio between the pressure gradient in the streamwise direction and  $\tau_w$  is constant. This ratio is constant when  $H_{12}$  is constant. The validity of

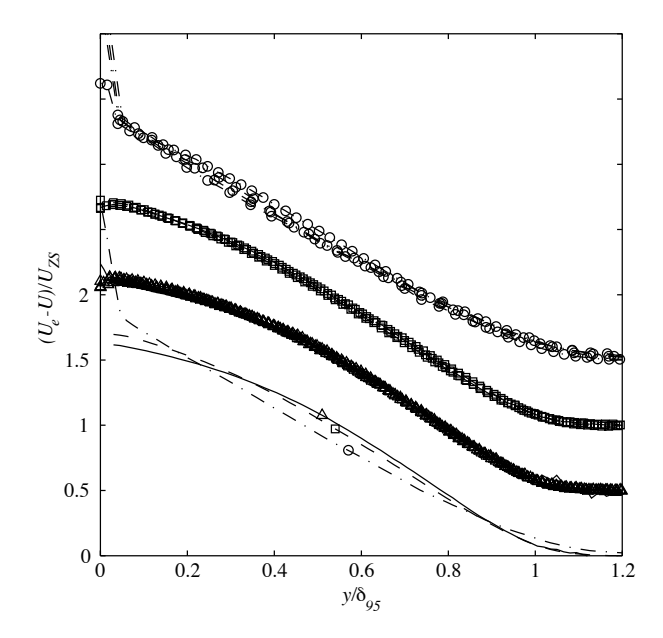


FIGURE 2.4. Mean velocity profiles for case II. The top three sets of curves show velocity profiles upstream of separation  $(\bigcirc)$ , between the separation point and the position of the maximum in  $H_{12}$   $(\square)$  and after the maximum in  $H_{12}$   $(\triangle)$ , respectively. The lower three curves show the average of the above three sets.

Townsend's criterion has been experimentally verified by Clauser (1954) and Skåre & Krogstad (1994).

Turbulent boundary layers developing towards separation clearly do not fulfill this criterion, as  $\tau_w$  decreases towards zero and then changes sign, while  $H_{12}$  monotonically increases. Usually the friction velocity,  $u_\tau = \sqrt{\tau_w/\rho}$  is used as the velocity scale. However to avoid the singularity at separation Mellor & Gibson (1966) suggested to instead use the scale  $u_p$  based on the pressure gradient and  $\delta_1$ . A different velocity scale,  $u_s$ , which explicitly depends on the maximum Reynolds shear-stress was suggested by Perry & Schofield (1973) and Schofield (1981). Here  $u_s$  is determined from a fit to the velocity profile. However Angele & Muhammad-Klingmann (2005a) showed that, for their data,  $u_p$  and  $u_s$  scale the same data-set upstream and downstream of separation equally well.

Recently, Maciel  $et\ al.\ (2006b)$  proved the usefulness of the Zagarola-Smits velocity scale (Zagarola & Smits (1998)), which is defined as

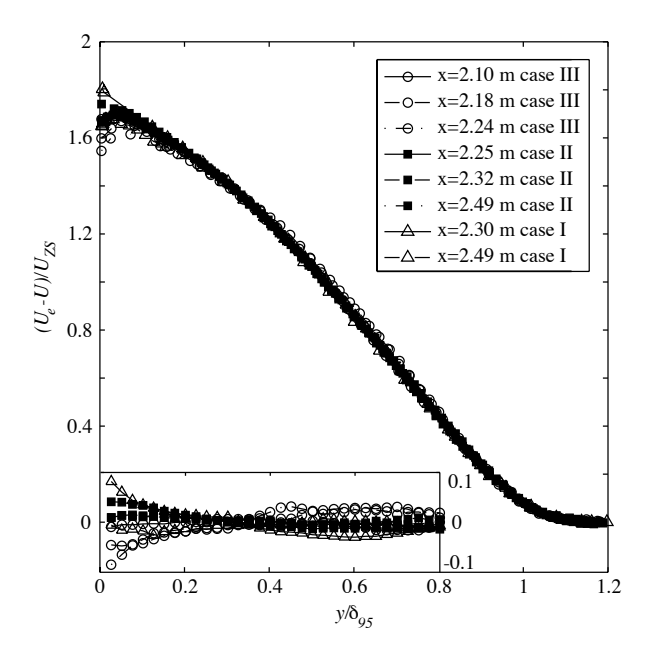


FIGURE 2.5. Mean velocity profiles in the region between the separation point and the position of the maximum in  $H_{12}$  for cases I, II and III. The insert shows how the velocity profiles deviate from an average of all profiles. Note that the scale of the ordinate is increased in the insert.

$$U_{ZS} = U_e \frac{\delta_1}{\delta}, \tag{2.1}$$

where  $U_e$  is the free-stream velocity and  $\delta$  is the boundary layer thickness. Their data before and after separation show similarity for the outer layer mean velocity distribution. Panton (2005) points out that  $u_{\tau}$  is proportional to the Zagarola-Smits velocity scale for high Reynolds numbers. Maciel et~al.~(2006~a) reviewed APG data from Perry (1966), Maciel et~al.~(2006~b), Skåre & Krogstad (1994), Dengel & Fernholz (1990) and others and showed that the Zagarola-Smits scaling works well.

In figure 2.4, the scaled mean velocity profiles of APG cases I-III are presented in three sets: upstream of  $x_s$ , in the separated region upstream of the position of maximum in  $H_{12}$ , denoted  $x_h$ , and after the position of the maximum in  $H_{12}$ . In the region upstream of  $x_s$ , the four plotted profiles do not show self-similarity. However, the three profiles between  $x_s$  and  $x_h$  are self-similar when scaled with  $U_{ZS}$ . The four velocity profiles for  $x > x_h$  are also self-similar, but only within that set of profiles, *i.e.* they are not self-similar when

#### 12 2. SEPARATION

they are plotted together with the profiles from upstream of  $x_h$ , as is shown at the bottom of figure 2.4. Thus, there seem to be two different self-similar regions in the separated region: before and after  $x_h$ .

To investigate whether the similarity holds between different sized separation bubbles, velocity profiles from the region  $x_s < x < x_h$  for flow cases I, II and III are scaled by  $U_{ZS}$  and plotted together in figure 2.5. In the outer region all profiles collapse, which is noteworthy since the differences in size of the separation bubbles are quite large.

In the recent study of Maciel et al. (2006a), it is shown that the meanvelocity defect profiles display self-similarity at some streamwise positions, but that data from the different experiments do not collapse. They suggest that the reason is the difference in the pressure gradients. The present results on the other hand, show velocity profiles that are self-similar in all three pressure gradient cases. Both the streamwise positions and the ranges of  $H_{12}$  differ between the cases. Thus, it is rather the streamwise position relative to the point of separation and the bubble maximum that determines the similarity.

#### CHAPTER 3

# Vane-type vortex generators

Control of separation of boundary layer flows can be achieved through different approaches. One common method, that has proved to be effective, is to introduce longitudinal vortices in the boundary layer. The vortices enhance mixing and transport high momentum fluid towards the wall.

The vortices are normally produced by vane-type VGs, *i.e.* short wings attached to the surface with the wingspan in the wall-normal direction and set at an angle  $\alpha$  towards the mean flow direction. Such devices are commonly seen on the wings of commercial aircraft and their blade height (h) are often slightly larger than  $\delta$ . The first experiments on conventional vane-type passive VGs were reported by Taylor (1947).

A VG array can be designed to produce different vortex configurations. The three basic types are shown in figure 3.1. The main geometrical parameters of a VG array are shown in figure 3.2.

#### 3.1. Vane-type VGs in ZPG

Pearcy (1961) published a comprehensive VG design guide. Here the vortex trajectories are also analysed, using the inviscid model from Jones (1957).

The evolution of a single vortices and vortex pairs embedded in a turbulent boundary layer was thoroughly investigated by Shabaka, Mehta & Bradshaw (1985) and later Mehta & Bradshaw (1988). They show that single vortices produce opposite sign vorticity around the vortex and that vortex pairs with common upflow are lifted out of the boundary layer. Another study of a single vortex in a boundary layer was performed by Westphal, Pauley & Eaton (1987). The overall circulation, when the vortex evolved downstream, either decreased slowly or remained almost constant depending on the case.

Pauley & Eaton (1988) examined the streamwise development of pairs and arrays of longitudinal vortices embedded in a zero pressure gradient (ZPG) turbulent boundary layer. In this study the blade spacing of VGs and the blade angle were varied, and the difference between counter-rotating vortices, with common upflow and downflow, and co-rotating vortices were examined. The proximity of other vortices does not affect circulation decay, but increases the diffusion of vorticity.

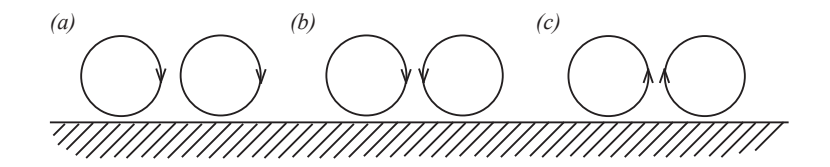


FIGURE 3.1. Different types of vortex pairs: (a) co-rotating, (b) counter-rotating with common downflow and (c) counter-rotating with common upflow.

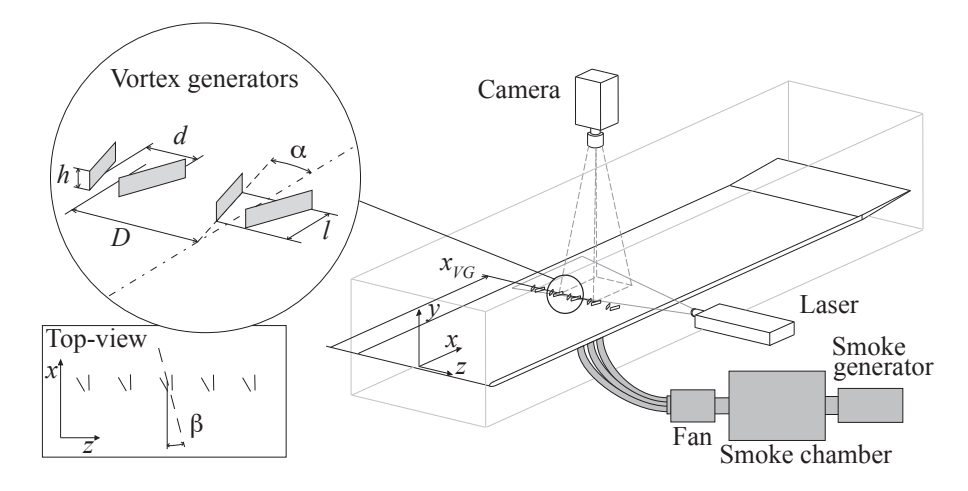


FIGURE 3.2. Sketch of the experimental setup, flow visualisation arrangement and VG geometry.

Wendt (2001) studied the initial circulation of an array of VGs. The vortex strength was observed to be proportional to  $U_e$ ,  $\alpha$  and the ratio  $h/\delta$ . Thus the circulation can be accurately modeled by a modified version of Prandtl's relation between circulation and airfoil geometry.

In most of the earlier studies VGs with  $h/\delta > 1$  have been used. However to reduce the drag penalty caused by the VGs, work has been done to reduce their size, without sacrificing efficiency. The comprehensive review on low-profile VGs by Lin (2002) shows that small  $(h/\delta \sim 0.2)$  VGs can be as effective in preventing separation.

An experimental investigation of the streamwise evolution of longitudinal vortices in ZPG was carried out in the MTL low-turbulence wind tunnel at KTH Mechanics. A horizontal 5.8 m long flat plate, which spans the whole 1.2 m width of the test-section, was mounted with its upper surface 0.51 m from

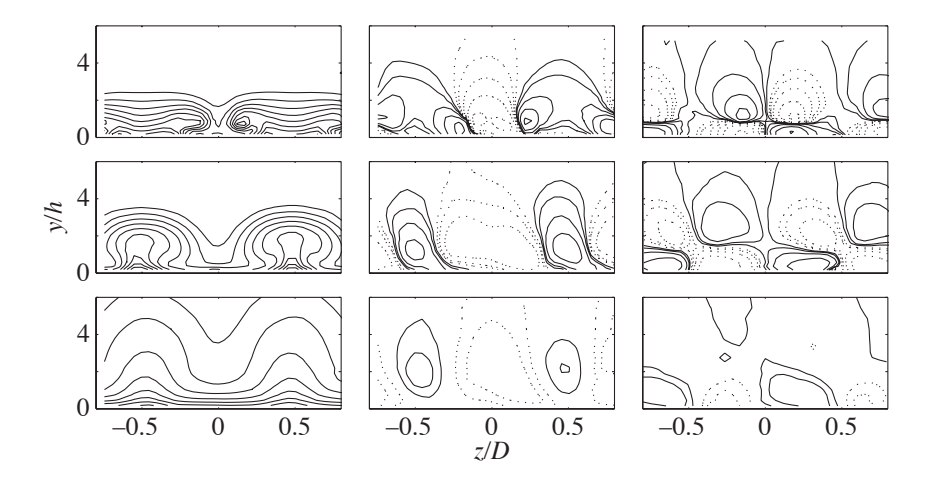


FIGURE 3.3. All three mean velocity components (from left to right, streamwise, wall-normal and spanwise) in the boundary layer in the  $VG_{10}^a$  configuration. From top to bottom the rows correspond to  $(x - x_{VG})/h = 6$ , 42, and 167, respectively.

the test-section ceiling at the leading edge. The ceiling was adjusted to give a zero streamwise pressure gradient at the nominal free stream velocity. At all velocity measurements  $U_e$  was set to 26.5 m/s and the temperature was kept constant at 18.1 °C. The velocity measurements were performed using hot-wire X-probes with the anemometer operating in constant-temperature mode.

In order to set up the streamwise vortices inside the turbulent boundary layer traditional vane-type VGs were used (see figure 3.2). Three different sizes of the VGs were used and arranged both as single spanwise pairs  $(^p)$  as well as spanwise arrays  $(^a)$  to create counter-rotating vortices inside the boundary layer. The design follows the criteria suggested by Pearcy (1961) and uses  $\alpha=15^{\circ}$ . The different VG sizes are geometrically "self-similar".

The vortices modify the base flow and in figure 3.3 the three mean velocity components of the  $VG_{10}$  array configuration are contour plotted. The U- and W-components are symmetric, however the asymmetry in the V-component is due to the large velocity gradients which affect the cooling velocities of the two wires of the X-probe differently. The maximum magnitude of the cross-flow components are approximately 15-25 % of  $U_e$  in the measurement plane closest to the VG array.

In figure 3.4(a) the vortex centre paths from VG pairs are projected on the y-z plane. The paths of the vortices behind the VG $_{10}^p$  and the VG $_{18}^p$  seem to collapse on each other. The downward motion in the beginning is caused by the induced velocity by the neighbouring vortex. However, as the two vortices

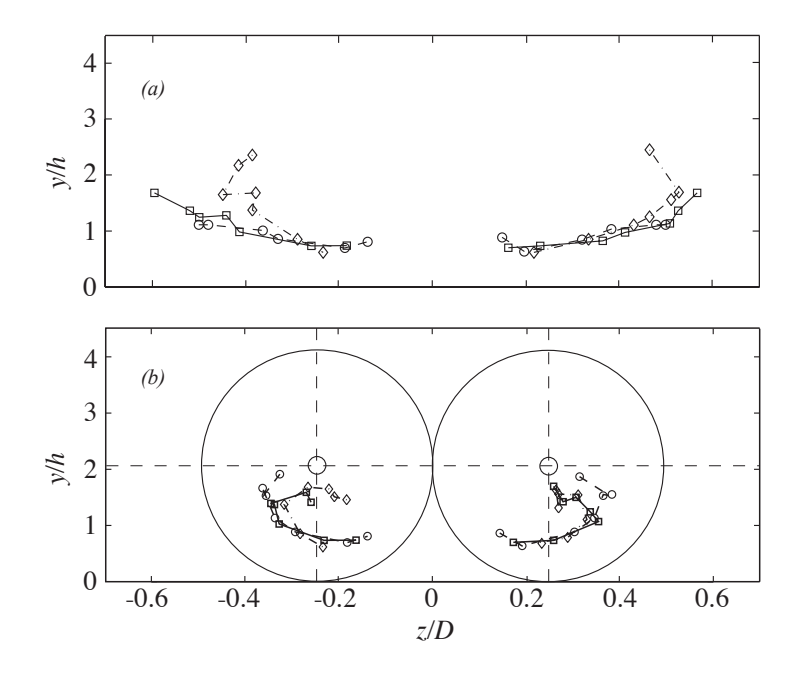


FIGURE 3.4. Vortex centre paths plotted in a y-z-plane normal to the stream.  $(-\cdot \lozenge \cdot -, -\square -, -- \bigcirc -)$  denote VG<sub>6</sub>, VG<sub>10</sub>, and VG<sub>18</sub>, respectively. (a) The paths downstream of a VG pair. (b) The same planes for an array of VGs .

move away from each other the influence from neighbouring vortex becomes weaker and the growth of the vortex causes the vortex centre to move away from the wall. An interesting behaviour of the  $VG_6^p$  vortex path is that it turns back towards the centre line.

The corresponding vortex paths of the VG arrays are shown in figure 3.4(b). In the case of the array, when the vortices move away from each other they are moving closer to the vortex from the neighbouring vortex pair and eventually form a new counter-rotating pair – this time with common upflow. The induced velocities in the new pair will tend to lift the vortices and according to inviscid theory (Jones 1957) they will continue to rise from the wall. However, the measurements show that the vortex centre paths of the original pair, while still rising, start to move towards each other again. This is probably due to vortex growth; when the area of the vortex grows the vortices are forced to a spanwise equidistant state. The maximum vortex radius in an equidistant system of circular vortices is D/4, where D is the spanwise distance between the VG pairs. If the distance from the vortex centre to the wall is D/4 (2.08h), the induced velocities from the real vortices and the three closest mirrored vortices

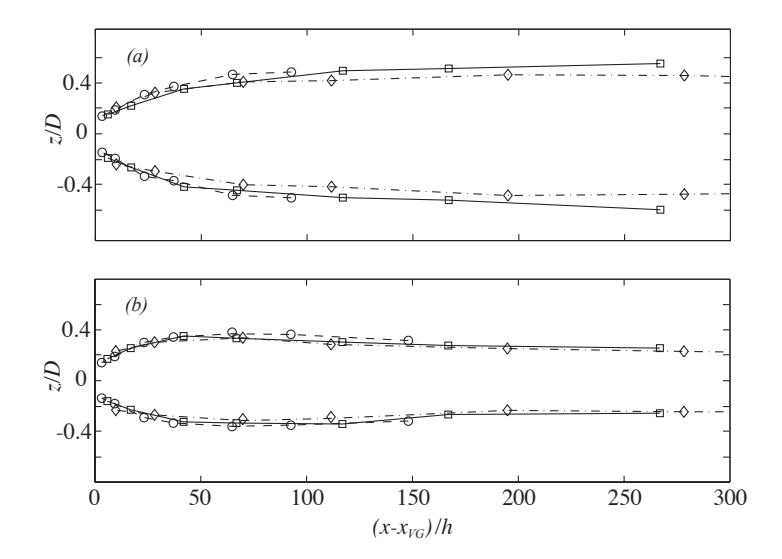


FIGURE 3.5. Vortex centre paths plotted in plan view (the x-z plane).  $(-\cdot \diamond \cdot -, -\Box -, -- \bigcirc --)$  denote h=(6, 10, 18) mm. (a) The paths downstream of a pair of VGs. (b) The same planes for a VG array. Note that for the array the paths of the neighboring vortices are actually within the figure area, but for the sake of clarity they are not shown.

all cancel. Hence, if the assumption holds, the vortex centres should approach  $(y/h,\ z/D)=(2.08,\pm0.25)$ . In figure 3.4(b), these coordinates are marked with small circles, and there seem to be a tendency for the vortex centres to move towards the predicted position.

Now, it is possible to explain the peculiar vortex centre path produced by the VG<sub>6</sub><sup>p</sup> in figure 3.4(a). In analogy to the paths of the vortices generated by the array, the curving back motion indicates the existence of secondary vortices, outside of the primary pair. At  $(x-x_{VG})/h=445$  the circulation of the secondary vortices is about 55% of the primary vortices. The secondary vortices probably originate from the very thin layer of stress-induced opposing  $\omega_x$  under the primary vortex.

In figure 3.5(a) the vortex paths from the single VG pair are shown in plan view. A divergence of the paths, from all VG sizes, caused by the mirrored images can be observed. The angle of divergence increases with vortex strength. Vortex centre paths downstream of VG arrays are plotted in figure 3.5(b). In plan view it is easy to see how the paths first move apart, roughly at the same rate as in the case of the single pairs, up to about  $(x - x_{VG})/h = 50$  and then

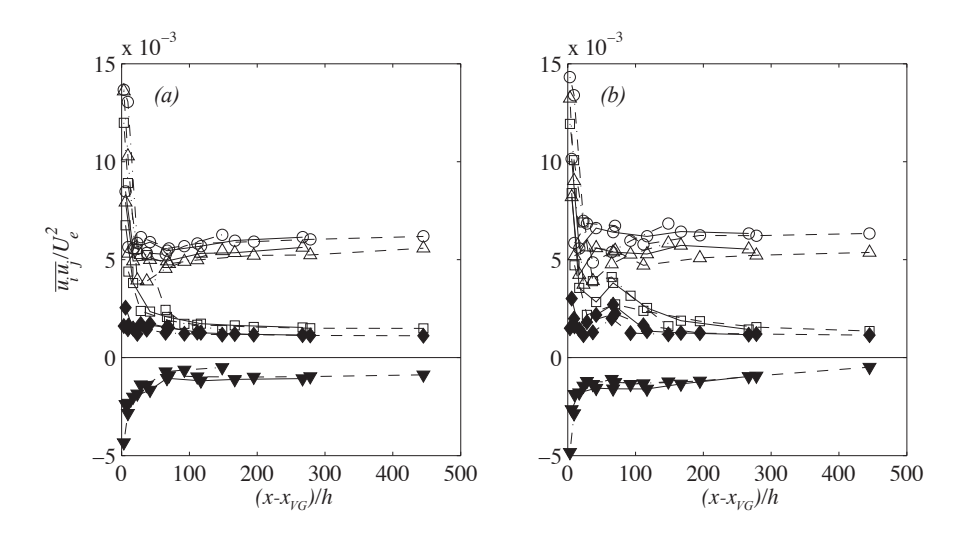


FIGURE 3.6. Streamwise evolution of the maximum values of the measured turbulence quantities for all VG heights. (a) and (b) show to the pair and the array configurations, respectively. ( $\bigcirc$ ,  $\square$ ,  $\triangle$ ,  $\blacklozenge$ ,  $\blacktriangledown$ ) correspond to  $\max_{yz} \{\langle u^2 \rangle/U_\infty^2, \, \langle v^2 \rangle/U_\infty^2, \, \langle w^2 \rangle/U_\infty^2, \, -\langle uv \rangle/U_\infty^2, \, -\langle uw \rangle/U_\infty^2 \}$ , respectively.

how they converge towards the asymptotic spanwise location of  $z/D=\pm 0.25$  as discussed earlier.

Also the turbulence quantities were measured and in figure 3.6 it is striking how well their maxima scale with h. Note, that here all three VG sizes have been plotted.

In many practical applications, especially on ground vehicles, the VGs operate in yaw most of the time. Therefore it is of interest to study vortex generation and decay under such non-ideal conditions.

When a VG pair is yawed the angle of attack of one blade is increasing while the angle of attack of the other blade is decreasing and therefore it is difficult to predict the total circulation generated by the VG pair. Figure 3.7(a) shows that the total circulation, up to a VG pair yaw angle of  $\beta=20^\circ$ , is almost constant and that the circulation decay (seen vertically in the figure) also seems to be independent of yaw. In figure 3.7(b) the effect of yaw on the individual vortices in a VG pair is shown. When the yaw angle increases (one blade angle is increasing, while the other is is decreasing) the circulation of both vortices changes linearly and according to the figure the blade that is parallel to the flow at  $\beta=15^\circ$  is still producing a vortex. The reason for this could be that

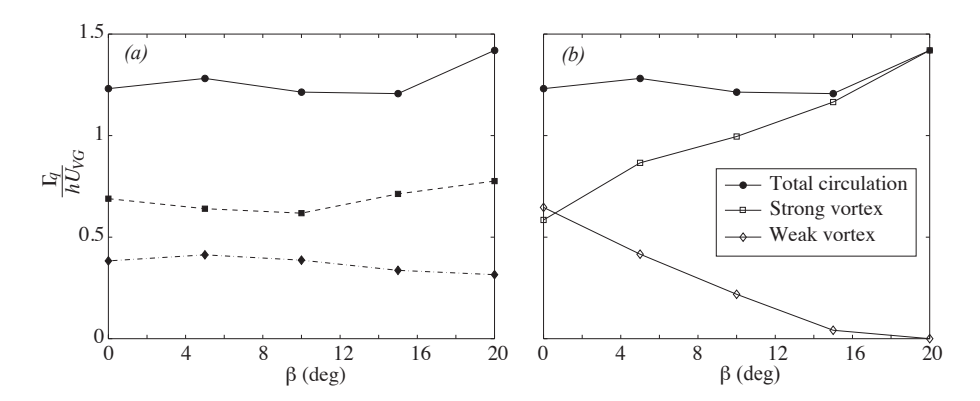


FIGURE 3.7. (a) The total circulation, *i.e.* the contribution from both the vortices, in the  $VG_{10}^p$  case versus the yaw angle at  $(x-x_{VG})/h=6$ , 41, 116 shown by  $(\circ, \Box, \diamondsuit)$ , respectively. (b) The individual contribution from the two vortices for the  $VG_{10}^p$  case at  $(x-x_{VG})/h=6$ .

the strong vortex is deflecting the flow to reach the parallel blade at some angle or that this is caused by vorticity induced by the larger vortex.

#### 3.2. Vane-type VGs in APG

Much research on VGs have been done in ZPG, but their real use is in APG. Schubauer & Spangenberg (1960) tried a variety of wall mounted devices to increase the mixing in the boundary layer. They did this in different APGs and they concluded that the effect of mixing is equivalent to a decrease in pressure gradient.

Godard & Stanislas (2006) made an optimisation study on co- and counterrotating VGs submerged in a APG boundary layer. They found that the counter-rotating set-up was twice as effective as the co-rotating in increasing the wall shear stress. In another recent experiment Angele & Muhammad-Klingmann (2005a) made extensive PIV measurements to show the flow and vortex development inside a turbulent boundary layer with a weak separation bubble.

In the present study the VG arrays of section 3.1 were positioned upstream of the separation bubbles described in section 2.1. Due to the rapidly growing boundary layer in that region, which causes the velocity at y = h to vary, four different VG arrays could be used to produce any vortex strength up to  $\gamma_e^{-1} = 4.0$  m/s by placing them at different streamwise positions  $(x_{VG})$ . The effect of the VGs on the separated region was studied with PIV.

 $<sup>^{1}\</sup>gamma_{e}$  is the circulation per unit width, calculated from h and the velocity at y=h.

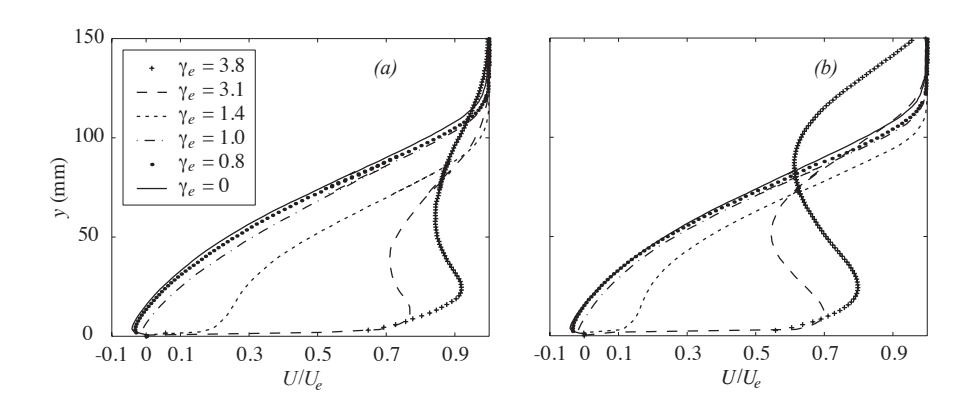


FIGURE 3.8. Mean velocity profiles at (a) the spanwise position of inflow and (b) the position of outflow.

In figure 3.8 the streamwise mean velocity profiles at the positions of inflow and outflow are shown for different VG configurations at  $x_h$  in APG case II. The uncontrolled case is shown for comparison. At the position of inflow, more streamwise momentum is transported down, and a larger effect of the VGs can be seen. The two VGs which produce the smallest amount of circulation have negligible influence on U, but when the circulation is increased to  $\gamma_e = 1.4$  separation is prevented. This is the most efficient VG configuration for eliminating separation in this particular flow case, in the sense that the drag generated by the VGs is expected to be less than that generated by the larger VGs. Even though this gives a pronounced efficiency maximum it could also cause a system designed for maximum efficiency to be sensitive to changes in the flow conditions.

Figure 3.9 summarizes the separation control effectiveness, in terms of  $H_{12}$ , of all examined VG configurations. Here  $H_{12}$  at  $x_h$  for cases I, II and III are compared for different magnitudes of  $\gamma_e$ . In the uncontrolled case,  $H_{12}$  is about 4, 5 and 7 in the respective cases. The value of  $\gamma_e$  at which the flow stays attached seems to be fairly insensitive to the pressure gradient, even though the difference in size of the separated region is quite large in the uncontrolled cases. When  $\gamma_e$  is further increased, the average  $H_{12}$  seems to asymptotically approach 1.4, which is the value of a ZPG turbulent boundary layer.

In order to investigate the influence of  $x_{VG}$ , the same level of circulation was produced at four different x positions. This was accomplished by applying differently sized VGs at different streamwise positions so that Uh at y=h is constant. Two arrays are placed before the pressure gradient peak, one is placed at the peak-position and one is positioned right after the maximum. In figure 3.10(a) the resulting mean streamwise velocity profiles at  $x_h$ 

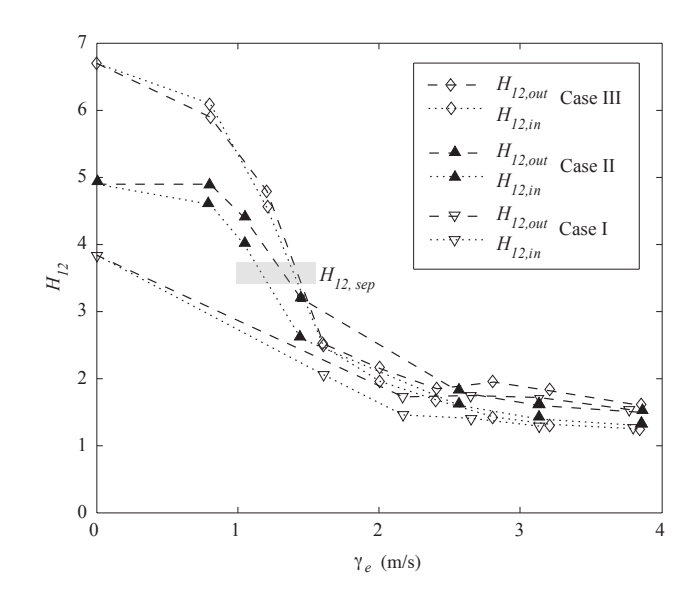


FIGURE 3.9. The shape factor  $H_{12}$  at the position of inflow and the position of outflow plotted against  $\gamma_e$  in case I, II and III. The measurements were made at  $x_h$ .

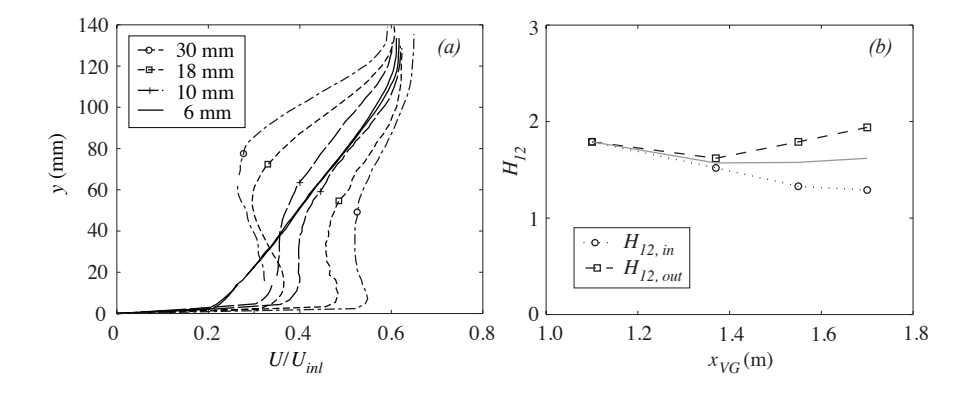


FIGURE 3.10. (a) Mean velocity profiles at the spanwise positions of inflow and outflow for four different VG configurations. The four rightmost profiles are measured at the position of inflow and the others at the position of outflow. (b)  $H_{12}$  measured at  $x_h$  for a generated  $\gamma_e$  of 3.1 m/s. The upper curve is  $H_{12}$  at the position of outflow and the lower curve is  $H_{12}$  at the position of inflow. The grey line shows the average  $H_{12}$ .

#### 22 3. VANE-TYPE VORTEX GENERATORS

are presented. For the case of 6 mm high VGs the boundary layer seems two-dimensional, but the 10 mm VG array shows a fuller profile at the position of inflow. For the next two cases of larger VGs, the shift of the profiles increases. However, if an average of the profiles at the inflow and outflow positions is taken for each VG size, the curves of the three largest VGs are similar. Hence, the shape factor of the average mean velocity profiles will be similar. This is shown in figure 3.10(b), where  $H_{12}$  at the inflow and outflow positions are plotted versus the upstream distance to the VG arrays. From this figure one can conclude that  $H_{12}$  at  $x_h$ , i.e. the control effect, is quite insensitive to the streamwise position of the VGs.

#### CHAPTER 4

# Jet vortex generators

An alternative way of producing the vortices is by jets originating from the wall. Flow control by vortex generator jets (VGJs) was first described by Wallis (1952). He claimed that an array of VGJs could be as effective as passive VGs in suppressing separation on an airfoil. In the following the jet direction is given by the skew and pitch angle, see figure 4.1 for a definition of the geometry.

#### 4.1. Steady jet VGs

A study by Johnston & Nishi (1990) demonstrated how streamwise vortices are produced by a VGJ array. A pitch angle of less than 90° was needed in order to generate vortices effectively. Some success in reducing the size of a separated region in an APG, was also demonstrated when the velocity ratio VR, which is the ratio of jet speed to free stream velocity, was 0.86 or higher. Compton & Johnston (1992) studied VGJs pitched at 45°. A skew between 45 and 90° was found to give the strongest vortices. The circulation of the vortices was also found to increase as the VR was increased.

In a study on a backward facing 25° ramp, where the flow separates, Selby, Lin & Howard (1992) measured the pressure for different VGJ array configurations. The pressure recovery increased up to the highest tested VR ratio of 6.8. It was shown that a small pitch angle (15° or 25°) is beneficial and that the optimum skew angle appears to be between 60° and 90°.

According to the review by Johnston (1999) the VR is the dominant parameter in generating circulation. The exact streamwise location of the VGJ row seems less important since the boundary layer reacts likewise independent of where it is energised. Khan & Johnston (2000) performed detailed measurements downstream of one VGJ and showed that the flow field is similar to that of solid VGs.

Zhang (2000) showed that a rectangular jet can produce higher levels of vorticity and circulation compared to a circular jet of equal hydraulic diameter and VR. Another experiment on the jet orifice shape by Johnston, Moiser & Khan (2002) showed that the inlet geometry affects the near-field but not the far-field. Zhang (2003) studied co-rotaing vortices produced by a spanwise array of VGJs, where both skew and pitch are set to  $45^{\circ}$ , and described the complex

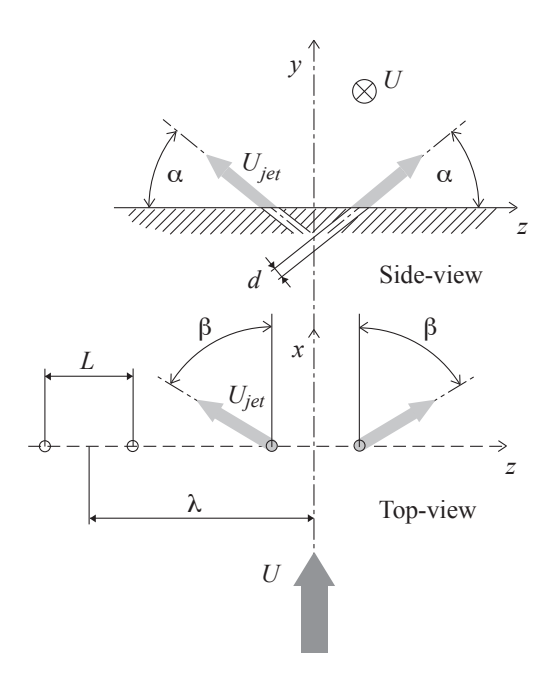


FIGURE 4.1. Schematic of a VGJ device producing counterrotating vortices. U is the free stream mean direction and  $U_{jet}$ is the jet velocity. The direction of the jet is defined by the pitch angle  $\alpha$  and the yaw angle  $\beta$ . The jet exit diameter is named d, the distance between the jets of a VGJ pair L and the distance between the pairs in an array  $\lambda$ . For a co-rotating array there is no L and thus  $\lambda$  is the distance between the jets.

near field. The ratio of the vortex strength of the primary and secondary vortices (cf. Rixon & Johari (2003)) are shown to depend on VR.

In all previous reports the vortex strength has been reported to increase monotonically with VR, but Milanovic & Zaman (2004) find a maximum in the region of VR = 2.0–2.8.

The most extensive investigation in recent years is the one by Godard & Stanislas (2006). They measure the skin friction increase for different VGJ configurations producing co-rotating and counter-rotating vortices. Their data shows that optimised VGJs produce results comparable to passive vane-type VGs in terms of skin friction increase. For a counter-rotating pair their optimal set of parameters are:  $\beta = 45 - 90^{\circ}$ ,  $\alpha = 45^{\circ}$  and L/d = 15. They show a strong increase in skin friction with jet velocities up to VR = 3.1. Above that

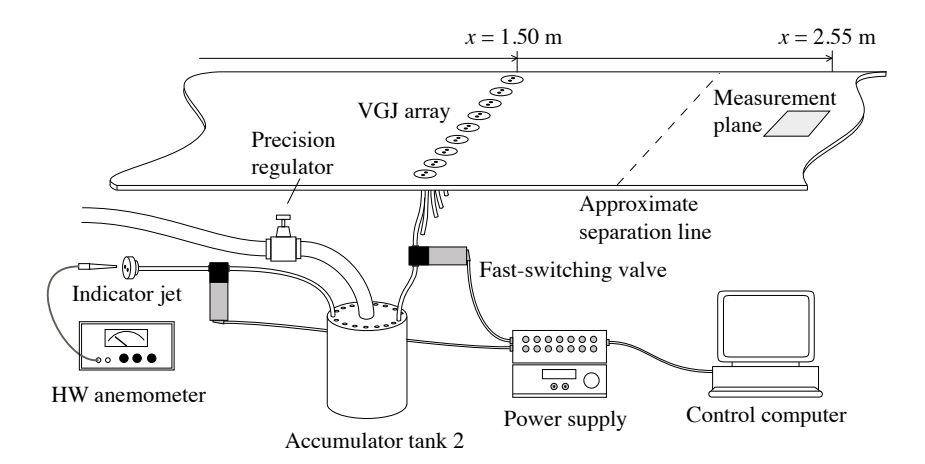


FIGURE 4.2. Schematic of VGJ set-up.

there is almost no increase. They also reported that the counter-rotating VGJ pair is still effective at free stream yaw angles up to  $20^{\circ}$ .

Here a counter-rotating configuration was chosen for the VGJ array and the geometry was chosen in agreement with the results of the above mentioned studies. The skew and pitch angles are chosen as 90° and 45°, respectively, and the jet spacing is L=16d. In figure 4.2 the set-up of the VGJ system is shown. The 9 unit (18 jets) array spans the full width (0.75 m) of the wind tunnel and deliver VR=8–9 at a test section inlet velocity  $U_{inl}$  of 26.5 m/s. One of the VGJ devices is placed outside the wind tunnel and a hot wire probe is used to continuously monitor the jet velocity during the experiments.

PIV is used to measure a 150 mm  $\times$  150 mm plane at y=5 mm, parallel to the wall. Since the small gradient makes it possible to average the data in the streamwise direction the accuracy of the spanwise velocity profile is increased. The streamwise-averaged velocity, normalised by  $U_{inl}$ , is called  $U_5$  in the following. From  $U_5$  a scalar effect measure can be calculated by averaging the velocity over one period  $\lambda$  in the spanwise direction. This scalar is termed  $\overline{U}_5$ .

Between the two counter-rotating vortices, at z/D=0, the vortices produce a downflow that transport streamwise momentum towards the wall. The effect of this can be seen for VR=3 in figure 4.3(a), where the velocity contours have a U-shape around z/D=0. At z/D=0.5 the vortices instead produce upflow and transport of low streamwise momentum from the wall. If VR is increased to 6 the U distribution in the cross-plane changes as can be seen when comparing figures 4.3(a,b). The velocity increases near the wall, but a high speed streak, unconnected to the free stream, is also formed at z/D=0.

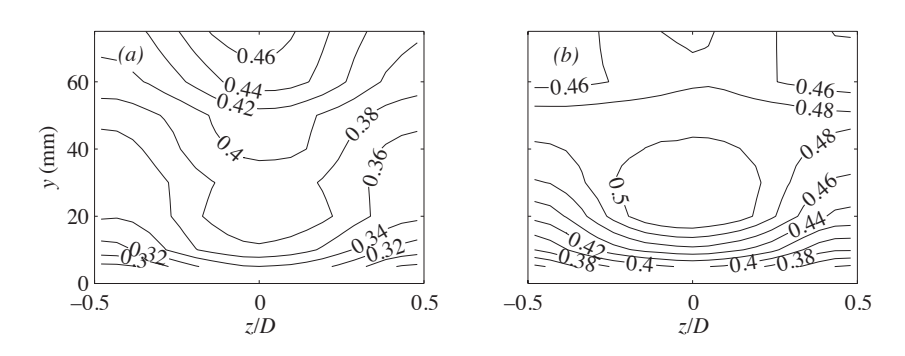


FIGURE 4.3. Contours of (a)  $U/U_{inl}$  at VR=3, (b)  $U/U_{inl}$  at VR=6. All measurements are taken at  $x_h$ .

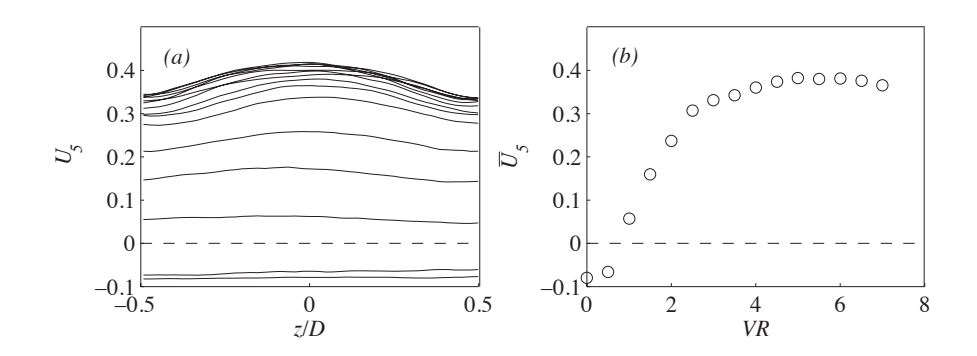


FIGURE 4.4. (a) Velocity profiles at y=5 mm for different VR and (b) the corresponding mean velocities  $\overline{U}_5$ .

With a fixed geometry the only variable parameter of the VGJs is VR. In figure 4.4(a) the velocity profiles at different jet velocities are shown and in figure 4.4(b) the corresponding  $\overline{U}_5$  is shown. There is almost no change when the jets are activated at VR=0.5. This is possibly because the jets are still too weak to produce any vortices. A further velocity increase to VR=1.0 eliminates the mean backflow. Thus, there are now longitudinal vortices present in the boundary layer. From VR=0.5 to VR=2.0 the increase in  $\overline{U}_5$  with VR is nearly linear. After that and up to VR=5.0 the control effectiveness is still increasing, but at a lower rate. Above VR=5.0 there is a decrease in  $\overline{U}_5$ .

The VGJ array is also tested at yaw. The VGJ devices of the array are yawed individually, at  $\theta=0^{\circ}-90^{\circ}$ , and the resulting  $\overline{U}_5$  is shown in figure 4.5.  $\overline{U}_5$  decreases slowly with  $\theta$ , down to a minimum at  $\theta=60^{\circ}$ . For increasing  $\theta>$ 

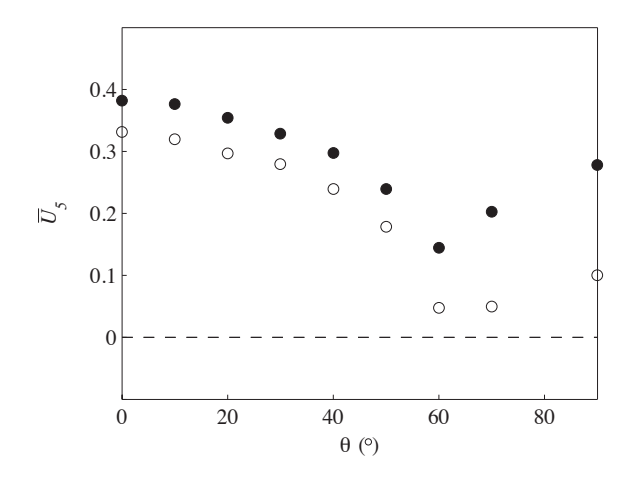


FIGURE 4.5. Effectiveness at different yaw angles. The open circles show VR=3 and the filled circles show VR=5.

 $60^{\circ}~\overline{U}_{5}$  increases to a second maximum at  $\theta=90^{\circ}.$  This is more pronounced for VR=5

#### 4.2. Pulsed jet VGs

The flow control effect of pulsed VGJs can be due to several different physical mechanisms. They can influence the flow by amplifying natural frequencies in the boundary layer, like the shedding of a stalled airfoil. Furthermore, they can function like steady VGJs and produce longitudinal vortices that transport high momentum fluid towards the wall. In the experiment presented in this article pulsed VGJs of the last category are applied. If the VGJ geometry is set, there are three main parameters that decide the performance of a pulsed VGJ. It is the velocity ratio, the pulsing frequency f and the duty cycle  $\Omega$ .

For steady VGJs the generated circulation depend strongly on VR and the same is valid for for pulsed VGJs. This has been shown for arrays of VGJs by McManus  $et\ al.\ (1995)$  and Kostas  $et\ al.\ (2007)$ . Also similar to steady jets is the occurrence of an circulation optimum in VR above which the vortex is translated out of the boundary layer.

In McManus et al. (1995) and Scholz et al. (2008) the frequency had little effect on lift and drag, but in McManus et al. (1996) the magnitude of the upper side suction peak was strongly dependent on the pulsing frequency. The optimum frequency Strouhal number was found to be of the same order as that characterizing the natural eddy shedding behind blunt objects.

The duty cycle was shown by Scholz *et al.* (2008) to be important in increasing post-stall lift on an airfoil. They found  $\Omega \leq 0.25$  to be most beneficial.

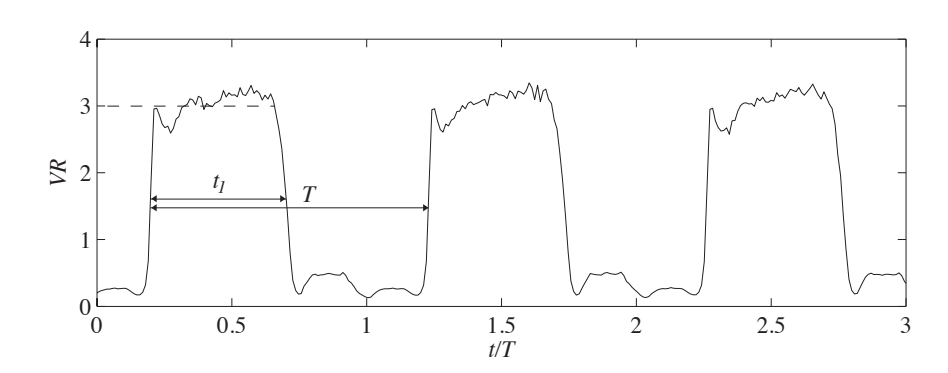


FIGURE 4.6. Jet pulses at VR = 3 and f = 100 Hz. The data is averaged over 30 cycles.

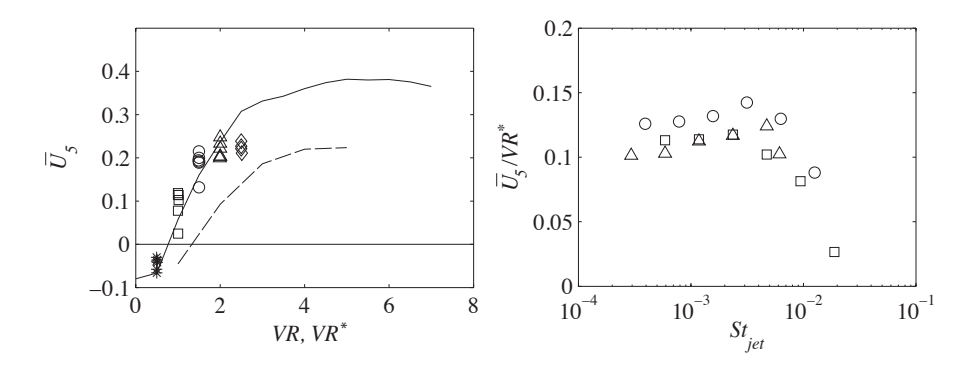


FIGURE 4.7. (a)  $\overline{U}_5$  vs VR and  $VR^*$ . The full line show steady jet results, the dashed line show average pulsed jet results and the symbols indicate  $\overline{U}_5$  vs  $VR^*$ . (b)  $\overline{U}_5/VR^*$  vs  $St_{jet}$  at VR=2,3 and 4.

In the study by Kostas et~al.~(2007) the wall shear stress increases nearly linearly with increasing  $\Omega$ . Johari & Rixon (2003) suggested that the maximum jet penetration determines the maximum circulation produced by a pulsed VGJ and suggested that the optimum injection time is 4–8  $d/U_{jet}$ .

In the same VGJ array as in figure 4.2 the jets were pulsed at f=12.5-400 Hz. A typical jet pulse train is shown in figure 4.6. The nominal injection velocity is the average of the pulse plateau. T is the period time and  $t_1$  is the injection time. Thus  $\Omega=t_1/T$ . There is a leakage flow when the valve is closed, but the volume and impulse of the leakage flow is low.

In figure 4.7(a) the control effect variation with VR is compared for steady and pulsed jets. The two lines show that the rate of increase of  $\overline{U}_5$  decreases

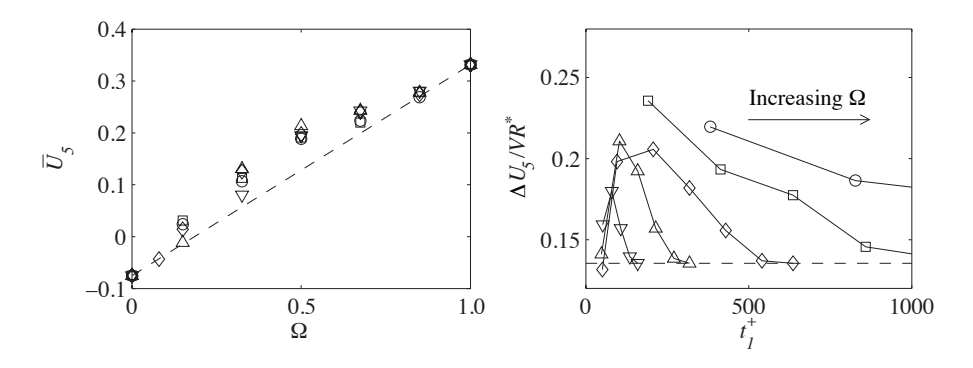


FIGURE 4.8. (a)  $\overline{U}_5$  vs  $\Omega$  for f=12.5 Hz ( $\circ$ ), f=25 Hz ( $\square$ ), f=50 Hz ( $\diamond$ ), f=100 Hz ( $\triangle$ ) and f=200 Hz ( $\nabla$ ) at VR=3. (b)  $\Delta \overline{U}_5/VR^*$  vs  $t_1^+$  for the same data as in (a)

at  $VR \approx 2.5-3$  for both configurations. The symbols show the data points at different frequencies and VRs plotted against  $VR^* = \Omega VR$ . When the pulsed data is compensated for the lower mass flow by using  $VR^*$  as measure, the control effect is similar to that of the steady jets. In order to study whether there is an maximum volume efficiency, the control effect is recalculated as  $\overline{U}_5/VR^*$ . If  $\overline{U}_5/VR^*$  is plotted against the jet based Strouhal number  $St_{jet} = fd/U_{jet}$ , there seems to be an optimum, as can be seen in figure 4.7(b).

The frequency and  $\Omega$  were varied at a constant VR=3. In figure 4.8(a) the resulting  $\overline{U}_5$  is shown. Compared to  $\Omega$ , the influence of f is small. A non-dimensional injection time is defined as  $t_1^+=t_1U_{jet}/d$ , and the variation of the control efficiency  $\Delta\overline{U}_5/VR^*$  with  $t_1^+$  is shown in figure 4.8(b). There seems to be a maximum at  $t_1^+=100-200$ 

At a constant f=50 Hz, the VR and  $\Omega$  is varied. As expected, figure 4.9(a) shows that a higher velocity ratios and longer duty cycles produce more control effect. If instead, the variation of  $\Delta \overline{U}_5/VR^*$  with  $t_1^+$  is studied, as shown in figure 4.9(b), it is possible to identify a maximum at  $t_1^+=100-150$  for VR=2,3 and 4.

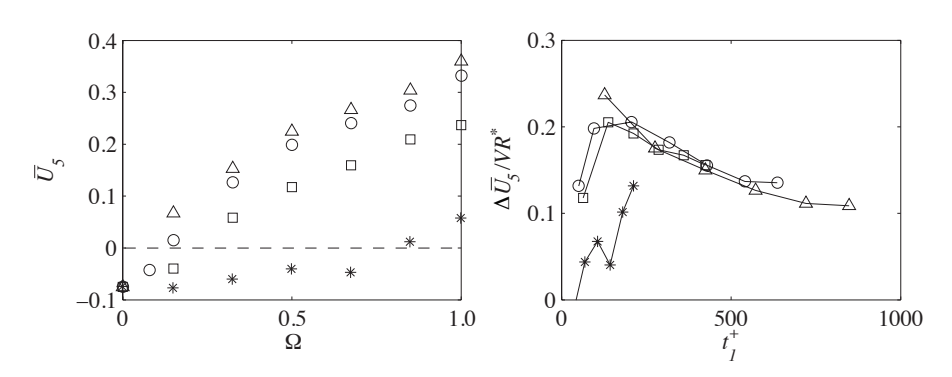


FIGURE 4.9. (a)  $\overline{U}_5$  vs  $\Omega$  for VR=1 (\*), VR=2 ( $\square$ ), VR=3 ( $\circ$ ) and VR=4 ( $\triangle$ ). (b)  $\Delta\overline{U}_5/VR^*$  vs  $t_1^+$  for the same data as in (a).

## CHAPTER 5

## Conclusions

In this chapter the main conclusions from the different investigations are summarised.

## 5.1. The separated region

- In the separated region the Zagarola-Smits velocity scaling was found to better scale the mean-velocity defect profiles than the methods suggested by Mellor & Gibson (1966), Perry & Schofield (1973) and Schofield (1981).
- There were two regions of similarity: before and after the maximum of  $H_{12}$  and  $\chi_w$  in the separation bubble. In these two regions velocity defect profiles are independent of the pressure gradient.
- $H_{12}$  increases linearly with increasing  $\chi_w$  in the separated region. Downstream of their maxima,  $H_{12}$  decreases linearly with decreasing  $\chi_w$ , but at a higher level of  $H_{12}$ .

## 5.2. Vane-type VGs

- The vortex core paths in plan view as well as in the plane normal to the flow, scale with the VG size in the downstream and spanwise directions.
- In this paper an asymptotic limit hypothesis of the vortex array path is stated and is shown to hold reasonable well. The limiting values for vortices far downstream are  $(y/h, z/D) = (2.08, \pm 0.25)$ , which the experimental data seems to approach.
- It is here shown, in the VG pair case, that the vortices are able to induce opposite sign vorticity, which is rolled up into a secondary vortex and strongly affect the primary vortex path.
- For VG arrays of different sizes, but with self-similar geometry, the generated circulation increases linearly with the vane tip velocity.
- In both the pair and the array configurations, the circulation decays exponentially at approximately the same rate.
- ullet The maxima of the turbulence quantities scale with h in the streamwise direction.
- The spanwise-averaged shape factor and circulation are unaffected by yaw.

- In order to capture the evolution of vortex core paths in the far region behind an array of counter-rotating vortices it has been shown through a pseudo-viscous vortex model that circulation decay and streamwise asymptotic limits have to be taken into account.
- For three separation bubbles of different size, separation was prevented at approximately the same  $\lambda_e$ . For higher  $\lambda_e$ ,  $H_{12}$  for all APGs approach a asymptotic value of 1.4.
- The streamwise position of the vortex generating devices is, within a certain range, of minor importance, which makes separation control by VGs robust and less sensitive to changing boundary conditions.

#### 5.3. Jet VGs

- VGJs have been shown to be as effective as vane-type VGs. Furthermore, there seems to be a maximum possible value of  $\overline{U}_5 \approx 0.4$ , that is common for both systems.
- The maximum  $\overline{U}_5$  is reached at VR = 5. The maximum volume flow efficiency and the maximum kinetic energy efficiency is obtained at VR = 2.0 and VR = 1.0, respectively.
- At yaw the control effect is decreasing slowly up to  $\theta = 40^{\circ}$ , where it is still 70–80% of the non-yawed level. Thus, the system robustness for yaw is good.
- When VR is in the maximum efficiency range and more control is needed, the VGJ array should, if possible, be made denser instead of increasing VR. Similarly, to reduce control the VGJ array is made more sparse.
- The basic mechanism of pulsed VGJs is pulse-width modulation. The control effectiveness is primarily a function of  $VR^* = \Omega VR$ . Thus, for maximum effectiveness at constant VR the duty cycle should be  $\Omega = 1$ .
- If they can be run at the optimum VR, pulsed jets can be more efficient than steady jets for a required level of  $\overline{U}_5$ .
- For a given  $\Omega$  there is a optimum  $St_{jet}$ . The optimum  $St_{jet}$  can be seen as a limit for a robust system, due to the rapid decrease in control effect at frequencies higher than the optimum.
- The injection time, and not  $\Omega$ , is the relevant parameter. Here the optimal injection time span is  $100 < t_1^+ < 200$ . The optimum  $St_{jet}$  mentioned above can be expressed in  $t_1^+$ . Thus, there are only two non-geometry parameters that determine the efficiency: VR and  $t_1^+$ .
- Johari & Rixon (2003) suggested that the optimal injection time for pulsed VGJs is in the range of 4–8  $d/U_{jet}$ . In the present experiment the optimal  $t_1$  has been shown to be approximately 25 times longer.

#### CHAPTER 6

## Outlook

## 6.1. Practical applications

Flow control systems utilising vane-type VGs, steady VGJs or pulsed VGJs have been shown to be effective and robust. This make them suitable for use on ground vehicles. As mentioned earlier an array can be utilised to energise the boundary layer upstream of a steep tapering of the vehicle rear end and thus prevent separation. The effectiveness of VGs and VGJs are equal and therefore the choice can be based on which system is the most practical. Passive VGs are of course simpler, but sharp blades cannot be mounted on a ground vehicle due to safety reasons. Furthermore they can not be turned off while braking or when driving in a convoy<sup>1</sup>.

There are other areas on a ground vehicle that can benefit from flow control, as for example the underbody. The internal flow systems can also be improved. The air inlet to the engine should have a low pressure drop even though the pipes are bent. Also the important cooling air flow can be increased if the pressure drop is reduced.

An obvious application of VGJs is on airplanes. Vane-type VGs are already used on wings and in engine air intakes, however also on an airplane it is useful to be able to turn of the flow control system.

#### 6.2. Further research

There are two main areas of interest that needs to be pursued: the application of the VGJ system on a bluff body and the exchange of pulsed jets for synthetic jets.

It would be valuable to study the effect of VGJs on a truck-like bluff body and analyse how the energy consumption will change. If the energy consumption of the jets is larger than the decrease in energy consumption caused by the drag reduction the system is less useful.

Synthetic jets are very attractive since they require no air supply and thus make the installation simple. Since a synthetic jet has little influence on the boundary layer during its suction phase their flow control mechanisms are the

 $<sup>^{1}</sup>$ The total drag of a convoy of trucks can probably be reduced if all vehicles except the last turn off their flow control systems to increase the wake size.

## 34 6. OUTLOOK

same as for non-synthetic jets. One example of a study using synthetic jets is the investigation by Amitay  $et\ al.\ (2001)$ . Synthetic jets are probably the way ahead, but injection times in the order of 100–200  $d/U_{jet}$  requires actuators with large reservoirs.

#### CHAPTER 7

## Papers and authors contributions

## Paper 1

On the scaling of turbulent boundary layers.
Ola Lögdberg (OL), K. P. Angele (KA) & P. H. Alfredsson (HAL).
Phys. Fluids **20**, 075104, 2008.

The experiments on APG case I was performed by KA and has already been reported in Angele & Muhammad-Klingmann (2006). APG cases II and III were measured by OL. The data analysis was done by OL and the writing was done by OL and KA jointly, in cooperation with HAL.

## Paper 2

Streamwise evolution of longitudinal vortices in a turbulent boundary layer. Ola Lögdberg, J. H. M. Fransson (JF) & P. H. Alfredsson. J. Fluid Mech. (In press).

The experiment was set up by OL, under the supervision of JF. The experiments and the data analysis were performed by OL. The writing was done by OL and JF jointly, in cooperation with HAL. Parts of this work was presented at the 6th European Fluid Mechanics Conference 2006, Stockholm. Some of the results have also been reported in Stillfried, Lögdberg, Wallin & Johansson (2009).

## Paper 3

On the robustness of separation control by streamwise vortices. Ola Lögdberg, K. P. Angele & P. H. Alfredsson

The experiments on APG case I was performed by KA and has already been reported in Angele & Muhammad-Klingmann (2005a). APG cases II and III were measured by OL. The data analysis was done by OL and the writing was done by OL, in cooperation with KA and HAL. Parts of this work was presented at the 4th International Symposium of Turbulence and Shear Flow Phenomena 2005, Williamsburg.

## 36 7. PAPERS AND AUTHORS CONTRIBUTIONS

## Paper 4

Separation control by an array of vortex generator jets. Part 1. Steady jets. Ola Lögdberg

## Paper 5

Separation control by an array of vortex generator jets. Part 2. Pulsed jets. Ola Lögdberg



## Acknowledgements

First I would like to thank my supervisor Prof. Henrik Alfredsson for accepting me as his student and for his guidance.

I would also like to thank my assistant supervisor Dr. Jens Fransson for teaching me how to set up and perform a nice experiment. Everything is so much easier if you are well organised.

Furthermore, I would like to thank Dr. Kristian Angele for introducing me to PIV and for his unlimited enthusiasm.

Special thanks to Dr. Olle Törnblom, Tek. Lic. Timmy Sigfrids and Dr. Claes Holmqvist for sharing lots of practical and theoretical knowledge on fluid mechanics. Thanks to Thomas Kurian for helping me with X-probe soldering. Tek. Lic. Ramis Örlü also assisted me with my probes, but he is also acknowledged for being the most helpful person in the lab. Thanks to Dr. Nils Tillmark for nice discussions and for his quest to bring some order to the lab.

I would like to thank my office-mates Dr. Thomas Hällqvist, Bengt Fallenius and Malte Kjellander for providing a cosy atmosphere. I also thank all other colleagues in lab for being nice and helpful.

Marcus Gällstedt, Ulf Landén, Joakim Karlström and Göran Rådberg in the work shop are all highly acknowledged for good advice and help with my experimental set-ups.

Scania CV AB is acknowledged for giving me the opportunity to carry out my doctorial work at KTH Mechanics within the Linné Flow Centre. Many thanks to Per Jonsson and Dr. Per Elofsson for their support.

Tack Cecilia! Livet vore så mycket tråkigare utan dig.

## References

- AMITAY, M., SMITH, D., KIBENS, V., PAREKH, D. E. & GLEZER, A. 2001 Aerodynamic flow control over an unconventional airfoil using synthetic jet actuators.  $AIAA\ J.\ 39,\ 361-370.$
- Angele, K. P. & Muhammad-Klingmann, B. 2005a The effect of streamwise vortices on the turbulence structure of a separating boundary layer. *Eur. J. Mech.* B **24**, 539–554.
- Angele, K. P. & Muhammad-Klingmann, B. 2005b A simple model for the effect of peak-locking on the accuracy of boundary layer statistics in digital PIV. Exp. Fluids  ${\bf 38},\ 341–347.$
- Angele, K. P. & Muhammad-Klingmann, B. 2006 PIV measurements in a weakly separating and reattaching turbulent boundary layer. *Eur. J. Mech.* B **25**, 204–222.
- Clauser, F. 1954 Turbulent boundary layers in adverse pressure gradients. *J. Aero. Sci.* 21, 91–108.
- COMPTON, D. & JOHNSTON, J. 1992 Streamwise vortex production by pitched and skewed jets in a turbulent boundary layer. AIAA J. 30, 640–647.
- Dengel, P. & Fernholz, H. 1990 An experimental investigation of an incompressible turbulent boundary layer in the vicinity of separation. *J. Fluid Mech.* **212**, 615–636.
- Godard, G. & Stanislas, M. 2006 Control of a decelerating boundary layer. Part 1: Optimization of passive vortex generators. *Aero. Sci. Tech.* **10**, 181–191.
- Godard, G. & Stanislas, M. 2006 Control of a decelerating boundary layer. part 3: Optimization of round jets vortex generators. *Aero. Sci. Tech.* **10**, 455–464.
- Johari, H. & Rixon, G. S. 2003 Effects of pulsing on a vortex generator jet. AIAA J. 41, 2309–2315.
- JOHNSTON, J. & NISHI, M. 1990 Vortex generator jets, means for flow separation control. AIAA J. 28, 989–994.
- Johnston, J. 1999 Pitched and skewed vortex generator jets for control of turbulent boundary layer separation: a review. In 3rd ASME/JSME Joint Fluids Eng. Conf.
- JOHNSTON, J., MOISER, B. & KHAN, Z. 2002 Vortex generating jets; effects of jethole inlet geometry. Int. J. Heat Fluid Flow 23, 744-749.

- Jones, J. P. 1957 The calculation of the paths of vortices from a system of vortex generators, and a comparison with experiment. *Tech Rep.* C. P. No. 361. Aeronautical Research Council.
- Kalter, M. & Fernholz, H. H. 2001 The reduction and elimination of a closed separation region by free-stream turbulence. *J. Fluid Mech.* 446, 271–308.
- KHAN, Z. U. & JOHNSTON, J. 2000 On vortex generating jets. Int. J. Heat Fluid Flow 21, 506–511.
- Kostas, J., Foucaut, J. M. & Stanislas, M. 2007 The flow structure produced by pulsed-jet vortex generators in a turbulent boundary layer in an adverse pressure gradient. Flow, Turbul. Combust. 78, 331–363.
- LIN, JOHN C. 2002 Review of research on low-profile vortex generators to control boundary-layer separation. *Prog. Aero. Sci.* **38**, 389–420.
- MACIEL, Y., ROSSIGNOL, K.-S. & LEMAY, J. 2006a Self-similarity in the outer region of adverse-pressure-gradient turbulent boundary layers. AIAA J. 44, 2450–2464.
- MACIEL, Y., ROSSIGNOL, K.-S. & LEMAY, J. 2006b A study of a turbulent boundary layer in stalled-airfoil-type flow conditions. *Exp. Fluids* 41, 573–590.
- McManus, K., Joshi, P., Legner, H. & Davis, S. 1995 Active control of aerodynamic stall using pulsed jet actuators, AIAA paper 95-2187.
- McManus, K., Ducharme, A., Goldey, C. & Magill, J. 1996 Pulsed jet actuators for surpressing flow separation, AIAA paper 96-0442.
- Mehta, R. D. & Bradshaw, P. 1988 Longitudinal vortices imbedded in turbulent boundary layers, part 2. vortex pair with 'common flow' upwards. *J. Fluid Mech.* **188**, 529–546.
- Mellor, G. L. & Gibson, D. M. 1966 Equilibrium turbulent boundary layers. J. Fluid Mech. 24, 225–253.
- MILANOVIC, I. & ZAMAN, K. 2004 Fluid dynamics of highly pitched and yawed jets in crossflow. AIAA J. 42 (5), 874–882.
- Panton, R. 2005 Review of wall turbulence as described by composite expansions. Appl. Mech. Rev.  ${\bf 58},\,1\text{--}36.$
- Pauley, Wayne R. & Eaton, John K. 1988 Experimental study of the development of longitudinal vortex pairs embedded in a turbulent boundary layer. AIAA J. 26, 816–823.
- Pearcy, H. H. 1961 Boundary Layer and Flow Control, its Principle and Applications, Vol 2, chap. Shock-Induced Separation and its Prevention, pp. 1170–1344. Pergamon Press, Oxford, England.
- Perry, A. 1966 Turbulent boundary layers in decreasing adverse pressure gradients. J. Fluid Mech. 26, 481–506.
- Perry, A. & Schofield, W. 1973 Mean velocity and shear stress distribution in turbulent boundary layers. *Phys. Fluids* **16**, 2068–2074.
- RIXON, S. G. & JOHARI, H. 2003 Development of a steady vortex generator jet in a turbulent boundary layer. J. Fluids Eng. 125, 1006–1015.
- Schofield, W. 1981 Equilibrium boundary layers in moderate to strong adverse pressure gradient. J. Fluid Mech. 113, 91–122.
- Scholz, P., Casper, M., Ortmanns, J., Kähler, C. J. & Radespiel, R. 2008

- Leading-edge separation control by means of pulsed vortex generator jets. AIAA J. 46, 837–846.
- Schubauer, G. B. & Spangenberg, W. G. 1960 Forced mixing in boundary layers. J. Fluid Mech. 8, 10–32.
- Selby, G., Lin, J. & Howard, F. 1992 Control of low-speed turbulent separated flow using jet vortex generators. *Exp. Fluids* **12**, 394–400.
- Shabaka, I. M. M. A., Mehta, R. D. & Bradshaw, P. 1985 Longitudinal vortices imbedded in turbulent boundary layers. Part 1. Single vortex. *J. Fluid Mech.* **155**, 37–57.
- SIMPSON, R. 1989 Turbulent boundary-layer separation. Annu. Rev. Fluid Mech. 21, 205–234.
- SKÅRE, P. & KROGSTAD, P. 1994 A turbulent equilibrium boundary layer near separation. J. Fluid Mech. 272, 319–348.
- VON STILLFRIED, F., LÖGDBERG, O., WALLIN, S. & JOHANSSON, A. 2009 Statistical modelling of the influence of turbulent flow separation control devices, AIAA paper 2009-1501.
- Taylor, H.D. 1947 The elimination of diffuser separation by vortex generators. Report R-4012-3. United Aircraft Corporation.
- TOWNSEND, A. A. 1961 Equilibrium layers and wall turbulence. *J. Fluid Mech.* 11, 97–120.
- Wallis, R. 1952 The use of air jets for boundary layer control. Aero note 110. Aerodynamics Research Laboratories, Australia.
- Wendt, Bruce J. 2001 Initial circulation and peak vorticity behavior of vortices shed from airfoil vortex generators. Tech Rep. NASA/CR 2001-211144. NASA.
- Westphal, R.V., Pauley, W.R. & Eaton, J.K. 1987 Interaction between a vortex and a turbulent boundary layer. Part 1: Mean flow evolution and turbulence properties. Tech Rep. TM 88361, NASA.
- ZAGAROLA, M. & SMITS, A. 1998 Mean-flow scaling of turbulent pipe flow. J. Fluid Mech. 373, 33–79.
- ZHANG, X. 2000 An inclined rectangular jet in a turbulent boundary layer-vortex flow. Exp. Fluids 28, 344–354.
- ZHANG, X. 2003 The evolution of co-rotating vortices in a canonical boundary layer with inclined jets. *Phys. Fluids* **15**, 3693–3702.

Part II

Papers

## Paper 1

# On the scaling of turbulent separating boundary layers

By O. Lögdberg<sup>1,2</sup>, K. Angele<sup>3</sup> and P. H. Alfredsson<sup>1</sup>

<sup>1</sup>Linné Flow Centre, KTH Mechanics, S-100 44 Stockholm, Sweden <sup>2</sup>Scania CV AB, S-151 87 Södertalje, Sweden <sup>3</sup>Vattenfall Research and Development AB, S-162 87 Stockholm, Sweden

Published in Phys. Fluids 20 075104, 2008

This study focuses on the mean velocity distribution of turbulent boundary layers near, at and after separation. The proper mean velocity scaling of the outer region in strong adverse pressure gradients and separated turbulent boundary layers is still under debate and over the years various different velocity scales have been proposed. Here the scaling proposed by Zagarola and Smits (J. Fluid Mech., 373, 33) is applied to data from three different separated flows. In all cases the mean velocity defect profiles are self-similar in the region between separation and the position of maximum mean reverse flow. Downstream of the reverse flow maximum the profiles change, but they are still self-similar within that region. It was also found that the mean velocity defect profiles of all three pressure gradients show similarity in the region between separation and the position of maximum mean reverse flow.

## 1. Introduction

The proper mean velocity scaling of the outer region in strong adverse pressure gradient (APG) and separated turbulent boundary layers is still under debate. According to Townsend (1961), the criterion for similarity to exist in the mean velocity profile is that the ratio between the pressure gradient in the streamwise direction (dP/dx) and the wall shear-stress  $(\tau_w)$  expressed as  $\beta = (\delta_1/\tau_w)(dP/dx)$ , is constant. This ratio is constant when the shape-factor,  $H_{12} = \delta_1/\delta_2$ , is constant  $(\delta_1)$  is the displacement thickness and  $\delta_2$  is the momentum loss thickness). The validity of Townsend's criterion has been experimentally verified by Clauser (1954) and Skåre & Krogstad (1994).

Turbulent boundary layers developing towards separation clearly do not fulfill this criterion, as the wall shear-stress decreases towards zero and then changes sign, while  $H_{12}$  monotonically increases. Usually the friction velocity,  $u_{\tau} = \sqrt{\tau_w/\rho}$ , where  $\rho$  is the density of the fluid, is used as the velocity

scale. However to avoid the singularity at separation Mellor & Gibson (1966) suggested to use instead the scale  $u_p$  defined as follows

$$u_p = \beta^{1/2} u_\tau = \sqrt{\frac{\delta_1}{\rho} \frac{dP}{dx}} \tag{1}$$

A different velocity scale,  $u_s$ , which explicitly depends on the maximum Reynolds shear-stress was suggested by Perry & Schofield (1973) and Schofield (1981). Here  $u_s$  is determined from a fit to the velocity profile in a similar manner as  $u_\tau$  is obtained from a Clauser plot. However Angele & Muhammad-Klingmann (2005a) showed that, for their data,  $u_p$  and  $u_s$  scale the same data-set before and after separation equally well.

Recently, Maciel *et al.* (2006b) proved the usefulness of the Zagarola-Smits velocity scale Zagarola & Smits (1998), which is defined as

$$U_{ZS} = U_e \frac{\delta_1}{\delta},\tag{2}$$

where  $U_e$  is the free-stream velocity and  $\delta$  is the boundary layer thickness (defined in a suitable way). Their data before and after separation show similarity for the outer layer mean velocity distribution, and also for the Reynolds stresses. Panton (2005) points out that  $u_{\tau}$  is proportional to the Zagarola-Smits velocity scale for high Reynolds numbers. Maciel et al. (2006a) reviewed APG data from Perry (1966), Maciel et al. (2006b), Skåre & Krogstad (1994), Dengel & Fernholz (1990) and others and showed that the Zagarola-Smits scaling works well.

In the present work, we apply the Zagarola-Smits scaling on two newly acquired pressure gradient cases as well as the data-set reported in Angele & Muhammad-Klingmann (2005a) (referred to as case I herein). The results show that the Zagarola-Smits velocity scaling is useful not only for the region near separation, but also for cases of different adverse pressure gradients.

## 2. Experimental setup

All experiments were performed in the KTH BL wind-tunnel, with a free stream velocity of 26.5 m/s at the inlet of the test section. The test section is 4.0 m long and has a cross-sectional area of  $0.75\times0.50$  m<sup>2</sup> (height×width). For a detailed description of the wind tunnel, the reader is referred to Lindgren & Johansson (2004). A vertical flat plate made of Plexiglas, which spans the whole height and length of the test section, is mounted unsymmetrically with its back surface 300 mm from the back side wall of the test section. The plate is equipped with pressure taps ( $\Delta x = 0.1$  m) along the centreline. At 1.25 m from the beginning of the test section, the back side wall diverge in order to decelerate the flow. Suction is applied on the curved wall to prevent separation there. The induced APG on the flat plate can be varied by adjusting the

TABLE 1. Separation bubble size. In the table,  $x_s$  denotes the position of separation,  $x_r$  is the position of reattachment,  $l_s$  is the length of the separated region,  $h_s$  is the maximum height of the separation bubble and  $H_{12,sep}$  is the shape factor at the position of separation.

	Case I	Case II	Case III
$(\mathrm{d}C_p/\mathrm{d}x)_{max} \ (\mathrm{m}^{-1})$	0.70	0.78	0.87
$x_s$ (m)	2.4	2.24	2.09
$x_r$ (m)	2.7	2.85	3.1
$l_s$ (m)	0.3	0.6	1.0
$h_s \; (\mathrm{mm})$	7	17	35
$H_{12,sep}$	3.45	3.52	3.75

suction rate through the curved wall. The measurements are made with PIV and for a detailed description of the experimental setup the reader is referred to Angele & Muhammad-Klingmann (2005a,b).

#### 3. Results

Three pressure gradients of different strengths are compared here. Case I is a weak separation bubble similar to the case of Dengel & Fernholz (1990), whereas case III is the strongest APG and the strength of case II is approximately in between case I and case III. In table 1 the main parameters of the three flow cases are given. We define the region of separated flow as where the backflow coefficient  $\chi_w$  is larger than 0.5. Note that with increasing APG the separation point moves upstream and the reattachment point downstream.

Figure 1 shows the evolution of the shape factor in the three flow cases. Upstream of x=1.8 m (before separation in all cases) there are no notable differences between the cases, but the maximum value of  $H_{12}$  in the separation bubble varies between 4.1 for case I to more than 7 in case III. Furthermore, the value of  $H_{12}$  at the point of separation increases with the size of the separation bubble, see table 1.

In figure 2, the scaled mean velocity profiles are presented in three sets: before the point of separation  $(x < x_s)$ , labeled with the index a in figure 1), in the separated region before the maximum in  $H_{12}$   $(x_s < x < x_h)$ , labeled with the index b in figure 1), and after the position of the maximum in  $H_{12}$   $(x > x_h)$ , labeled with the index c in figure 1). Here  $\delta_{95}$  is used as the outer length scale. The different sets of curves are offset to make the figure more readable. In the region upstream of separation,  $x < x_s$ , the four plotted profiles do not show

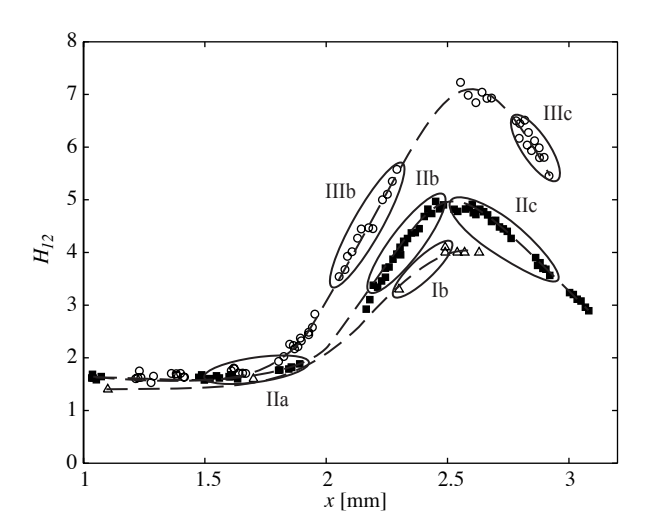


FIGURE 1. The evolution of the shape factor for the three different pressure gradient cases. I (open triangle), II (filled square) and III (open circle). Region **a** in the streamwise direction is upstream of separation, region **b** is between the separation point and the position of maximum in  $H_{12}$  and region **c** is downstream of the position of the maximum in  $H_{12}$ .

self-similarity. However, the three profiles for  $x_s < x < x_h$  are self-similar when scaled with  $U_{ZS}$ . In this self-similar region the boundary layer thickness  $\delta_{95}$  grows from 70 to 110 mm and  $\delta_1$  increases from 40 to 70 mm, over a streamwise distance of 240 mm.

The four velocity profiles for  $x>x_h$  are also self-similar, but only within that set of profiles, *i.e.* they are not self-similar when they are plotted together with the ones upstream of  $x_h$ , as is shown at the bottom of figure 2. Thus, there seems to be two different self-similar regions in the separated region, before and after  $x_h$ . For case II there are no data in between the two regions, but for case III there is an intermediate region where the velocity profile seems to be an average of the ones in regions b and c.

In the study of Dengel & Fernholz (1990) a linear relationship between  $H_{12}$  and the backflow coefficient,  $\chi_w$  was claimed. In their experiment the value of  $H_{12}$  is the same at separation and reattachment. A similar linear relationship between  $H_{12}$  and  $\chi_w$  is found in this study, but here there are two separate linear regions before and after  $x_h$ , as can be seen in figure 3. The transition between the two linear regions seems abrupt, but it takes place over a region of approximately  $\Delta x{=}0.2$  m. It is tempting to connect the respective linear regions to the different regions of self-similarity before and after  $x_h$ , but note that the linearity extends to  $\chi_w{=}0$ , where the velocity profiles no

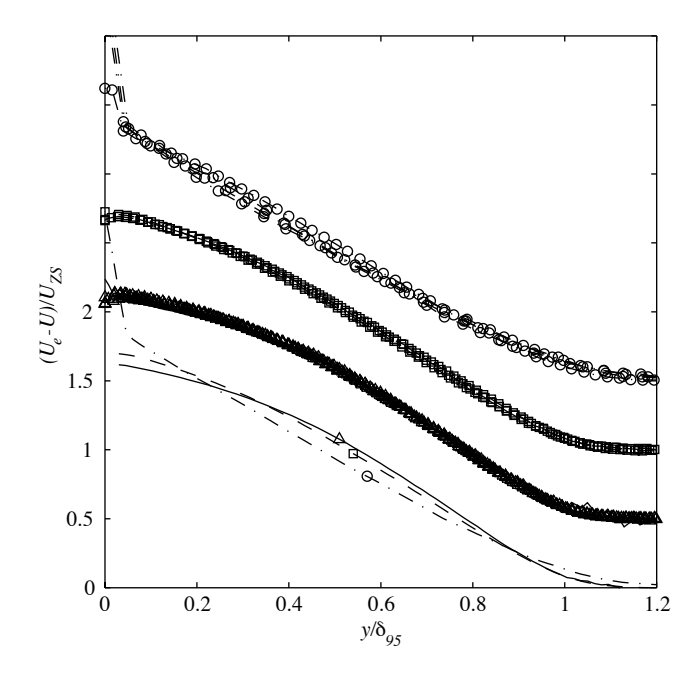


FIGURE 2. Mean velocity profiles scaled with  $U_{ZS}$  and  $\delta_{95}$  for case II. The top three sets of curves show velocity profiles upstream of separation (a, circles), between the separation point and the position of the maximum in  $H_{12}$  (b, squares) and after the maximum in  $H_{12}$  (c, triangles), respectively. The lower three curves show the average of the above three sets.

longer collapse. Figure 3 also shows that  $H_{12}$  and  $\chi_w$  both reach their extreme values at the same streamwise position. The shape factor at reattachment has increased by  $\Delta H_{12} \approx 0.5$  compared to the separation point, contradicting the results obtained by Dengel & Fernholz (1990).

To investigate whether the similarity holds between separation bubbles of different size, velocity profiles from the respective region upstream of the maximum in  $H_{12}$  for flow cases I, II and III are scaled by  $U_{ZS}$  and plotted together in figure 4. For  $y/\delta_{95}>0.15$  all profiles collapse. This is noteworthy since the differences in size of the separation bubbles are quite large. There are no data available downstream of the maximum in  $H_{12}$  for case I, but the profiles of case II and case III show similarity in region c as well.

We should also point out that the scalings based on  $u_s$  and  $u_p$ , which rendered self-similarity for case I in Angele & Muhammad-Klingmann (2005a), do not show the same extent of similarity as the Zagarola-Smits scaling showed here.

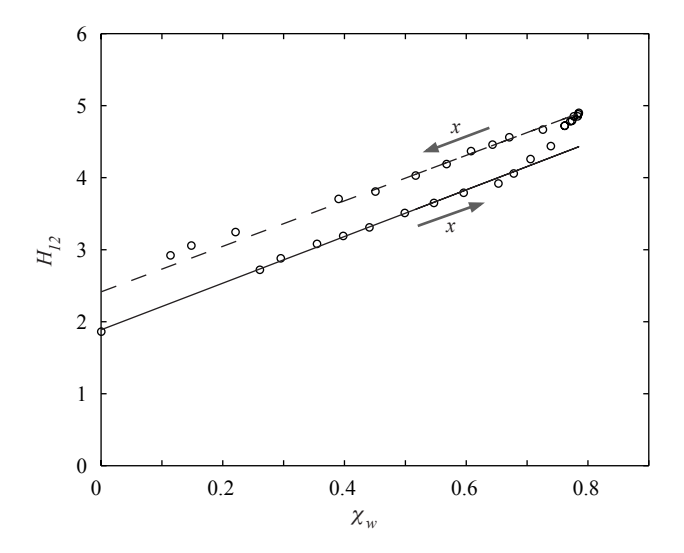


FIGURE 3. The shape factor  $H_{12}$  as a function of the back flow coefficient  $\chi_w$  for case II. The arrows indicate the direction of increasing x.

## 4. Discussion

In the recent study of Maciel et al. (2006a), where a number of experiments are compared, it is shown that the mean-velocity defect profiles display self-similarity at some streamwise positions, but that data from the different experiments do not collapse. The reason for this is said to be the difference in the pressure gradients. The present results on the other hand, show that the velocity profiles are self-similar in all three pressure gradient cases. Both the streamwise positions and the ranges of  $H_{12}$  differ between the cases, however, it is rather the streamwise position relative to the point of separation and the bubble maximum that determines the similarity.

According to the similarity analysis presented by Maciel  $et\ al.\ (2006a)$ , there are three necessary conditions for self-similarity, namely that the following parameters are constant

$$\beta_{ZS} = \frac{\delta_{95}^2}{\delta_1 \rho U_e^2} \frac{dP}{dx}, \ \gamma_{ZS} = \frac{\delta_1}{\delta_{95}} = \frac{U_{ZS}}{U_e}, \ \frac{d\delta_{95}}{dx}$$
 (3)

The latter two criteria leads to the conclusion that both the length scales  $\delta_{95}$  and  $\delta_1$  should increase linearly in the streamwise direction and that both  $\delta_{95}$  and  $\delta_1$  work equally well as the outer length scale. Also,  $U_e$  can be used instead of  $U_{ZS}$  as the velocity scale.

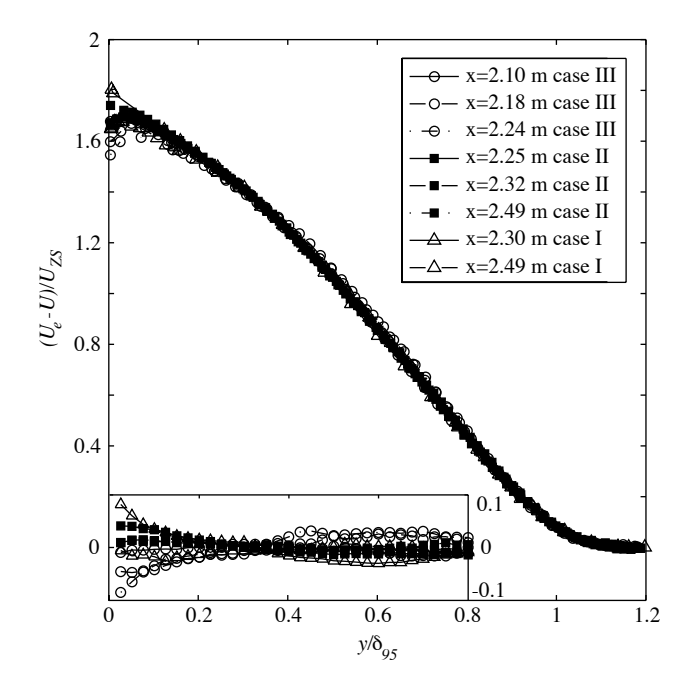


FIGURE 4. Mean velocity profiles scaled with  $U_{ZS}$  and  $\delta_{95}$  in the region between the separation point and the position of the maximum in  $H_{12}$  for cases I, II and III. The insert shows how the velocity profiles deviate from an average of all profiles. Note that the scale of the ordinate is increased in the insert.

These consequences are the same as the ones for the theory presented by Townsend (1961). These were not fulfilled in the cases by Maciel et~al.~(2006b) and Dengel & Fernholz (1990) even though  $\beta_{ZS}$  and  $\gamma_{ZS}$  do not change very much in the regions where the mean-velocity profiles are self-similar. In the case reported in Skåre & Krogstad (1994), however, they are constant, but in that case also  $\beta$  and  $H_{12}$  are constant, which fulfills the criteria of the classical equilibrium. For the present case  $\beta_{ZS}$  and  $\gamma_{ZS}$  are shown in figure 5 and 6. Neither parameter is constant in the self-similar regions.  $\beta_{ZS}$  decreases when  $\chi_w$  increases and vice versa.  $\gamma_{ZS}$  behaves in the opposite way and since  $(U_e-U)/U_{ZS}=1/\gamma_{ZS}$  on the wall, it can also be seen from figure 4 that despite the self-similarity of the velocity profiles  $\gamma_{ZS}$  is not constant. Note that in the separated region,  $\beta_{ZS}$  is larger and  $\gamma_{ZS}$  is smaller for the weaker separation bubbles.

As pointed out by Maciel et al. (2006a), mean-velocity defect profiles scaled with  $U_{ZS}$  can exhibit an apparent similarity, due to the fact that the scaling forces the area under the curve to be equal to one. In the present case the

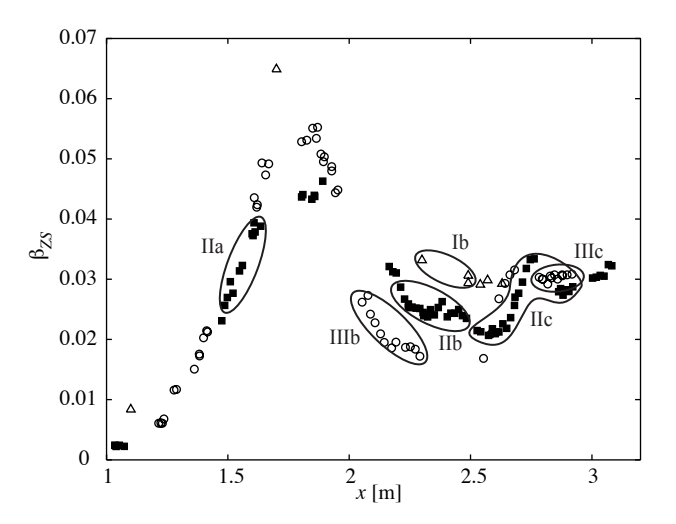


FIGURE 5. The downstream development  $\beta_{ZS}$ . Symbols as in figure 1.

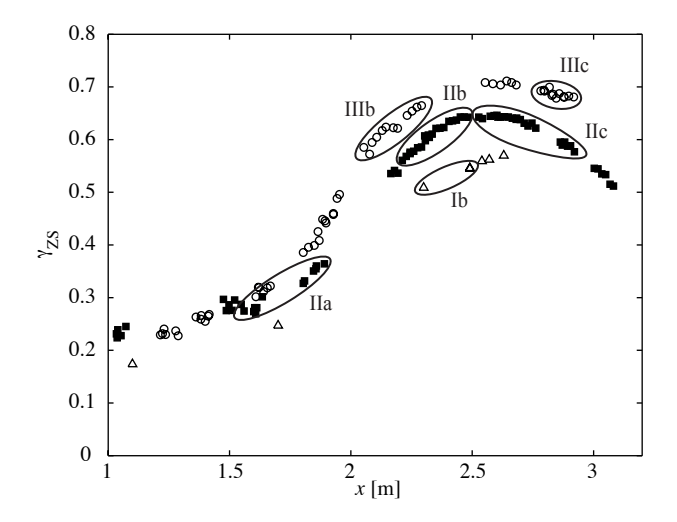


FIGURE 6. The downstream development  $\gamma_{ZS}$ . Symbols as in figure 1.

average velocity profiles from the different sets of curves in figure 2, show that differences in shape are still possible to detect.

To conclude we have found that the Zagarola-Smits velocity scaling for mean-velocity defect profiles is useful not only for the region around separation but also for cases of different pressure gradients. There seem to be two distinct regions of similarity before and after the maximum of  $H_{12}$  and  $\chi_w$  in the separation bubble. In these two regions velocity defect profiles are independent of the pressure gradient.

## Acknowledgements

This work is part of a cooperative research program between KTH and Scania CV.

## References

- Angele, K. P. & Muhammad-Klingmann, B. 2005a The effect of streamwise vortices on the turbulence structure of a separating boundary layer. *Eur. J. Mech.* B/Fluids **24**, 539–554.
- Angele, K. P. & Muhammad-Klingmann, B. 2005b A simple model for the effect of peak-locking on the accuracy of boundary layer statistics in digital PIV. Exp. Fluids 38, 341–347.
- CLAUSER, F. 1954 Turbulent boundary layers in adverse pressure gradients. *J. Aero. Sci.* 21, 91–108.
- Dengel, P. & Fernholz, H. 1990 An experimental investigation of an incompressible turbulent boundary layer in the vicinity of separation. *J. Fluid Mech.* **212**, 615–636
- LINDGREN, B. & JOHANSSON, A. V. 2004 Evaluation of a new wind-tunnel with expanding corners. *Exp. Fluids* **36**, 197–203.
- MACIEL, Y., ROSSIGNOL, K.-S. & LEMAY, J. 2006a Self-similarity in the outer region of adverse-pressure-gradient turbulent boundary layers. AIAA J. 44, 2450–2464.
- MACIEL, Y., ROSSIGNOL, K.-S. & LEMAY, J. 2006b A study of a turbulent boundary layer in stalled-airfoil-type flow conditions. *Exp. Fluids* 41, 573–590.
- Mellor, G. L. & Gibson, D. M. 1966 Equilibrium turbulent boundary layers. J. Fluid Mech. 24, 225–253.
- Panton, R. 2005 Review of wall turbulence as described by composite expansions. Appl. Mech. Rev.  $\bf 58, \, 1\text{--}36.$
- Perry, A. 1966 Turbulent boundary layers in decreasing adverse pressure gradients. J. Fluid Mech. 26, 481–506.
- Perry, A. & Schofield, W. 1973 Mean velocity and shear stress distribution in turbulent boundary layers. *Phys. Fluids* **16**, 2068–2074.
- Schofield, W. 1981 Equilibrium boundary layers in moderate to strong adverse pressure gradient. *J. Fluid Mech.* **113**, 91–122.
- Skåre, P. & Krogstad, P. 1994 A turbulent equilibrium boundary layer near separation. J. Fluid Mech. 272, 319–348.
- TOWNSEND, A. A. 1961 Equilibrium layers and wall turbulence. *J. Fluid Mech.* 11, 97–120.

ZAGAROLA, M. & SMITS, A. 1998 Mean-flow scaling of turbulent pipe flow. J. Fluid Mech.  $\bf 373$ ,  $\bf 33-79$ .

## Paper 2

# Streamwise evolution of longitudinal vortices in a turbulent boundary layer

By O. Lögdberg<sup>1,2</sup>, J. H. M. Fransson<sup>1</sup> and P. H. Alfredsson<sup>1</sup>

<sup>1</sup>Linné Flow Centre, KTH Mechanics, S-100 44 Stockholm, Sweden
<sup>2</sup>Scania CV AB, S-151 87 Södertalje, Sweden

Accepted in J. Fluids Mech.

In this experimental study both smoke visualisation and three component hotwire measurements have been performed in order to characterize the streamwise evolution of longitudinal counter-rotating vortices in a turbulent boundary layer. The vortices were generated by means of vortex generators (VGs) in different configurations. Both single pairs and arrays in a natural setting as well as in yaw have been considered. Moreover three different vortex blade heights h, with the spacing d and the distance to the neighbouring vortex pair D for the array configuration, were studied keeping the same d/h and D/h ratios. It is shown that the vortex core paths scale with h in the streamwise direction and with D and h in the spanwise and wall-normal directions, respectively. A new peculiar "hooklike" vortex core motion, seen in the cross-flow plane, has been identified in the far region, starting around 200h and 50h for the pair and the array configuration, respectively. This behaviour is explained in the paper. Furthermore the experimental data indicate that the vortex paths asymptote to a prescribed location in the cross-flow plane, which first was stated as a hypothesis and later verified. This observation goes against previously reported numerical results based on inviscid theory. An account for the important viscous effects is taken in a pseudo-viscous vortex model which is able to capture the streamwise core evolution throughout the measurement region down to 450h. Finally, the effect of yawing is reported, and it is shown that spanwiseaveraged quantities such as the shape factor and the circulation are hardly perceptible. However, the evolution of the vortex cores are different both between the pair and the array configuration and in the natural setting versus the case with yaw. From a general point of view the present paper reports on fundamental results concerning the vortex evolution in a fully developed turbulent boundary layer.

## 1. Introduction

## 1.1. Background and motivation

This work deals with the development of streamwise vortices in turbulent boundary layers. Vortices are introduced in a controlled way by vortex generators (VGs) and their downstream development is investigated. The interest in such development is twofold: firstly because of the appearance of streamwise vortices in many natural flow situations and secondly because of the use of VGs to control separation.

In laminar and turbulent boundary layers along concave surfaces streamwise-oriented vortices develop, usually called Görtler vortices (see e.g. Swearingen & Blackwelder 1987). Also boundary layers influenced by spanwise rotation may develop streamwise-oriented vortices (Watmuff  $et\ al.\ 1985$ ). In these two cases centrifugal and Coriolis forces, respectively, give rise to the vortices.

Surface roughness in laminar boundary layers may also generate streamwise vortices, which develop into longitudinal streaks of high and low velocities. Depending on the roughness height Reynolds number and spanwise distribution they may either promote or delay transition (Fransson *et al.* 2005, 2006). In turbulent boundary layers streamwise-oriented streaky structures of low and high velocities are well documented and are believed to be associated with streamwise vortices (Blackwelder & Eckelmann 1979).

As mentioned above the introduction of streamwise vortices through VGs can be used in order to delay or even avoid separation in adverse pressure gradient (APG) flows. Such devices are commonly observed on aircraft wings, diffusers and other APG surfaces but also have a potential to be used on ground vehicles. The work presented here is partly motivated by the possibility to reduce drag on trucks, by adding a boat tail to the rear and hence reducing the pressure drag. However, there is a restriction, prescribed by law, on how long the tail can be, and hence the deflection angle becomes an important parameter. Too large angles would give flow separation, which may be avoided by means of passive VGs. For design optimization fundamental knowledge of vortex evolution and induced drag is therefore needed. Here, we have chosen a fundamental study philosophy by idealizing the flow geometry to a zero pressure gradient (ZPG) turbulent boundary layer over a flat plate. This less complex flow geometry, compared to practical flow situations, allows us to focus on the fluid physics to a higher degree. One should however be careful in drawing conclusions for the APG case based on the present ZPG investigation, since the results are believed to depend on the pressure gradient to some degree.

Although naturally developing vortices are of interest in their own right we will only review the literature in which vortices are introduced into the boundary layer with some kind of vane-type VG, either to study the effect on separation directly or to study the vortex development in itself.

#### 1.2. Review of streamwise vortex development work

The first experiments on conventional vane-type passive VGs were reported by Taylor (1947). This type of VG normally consists of a row of blades or airfoils mounted perpendicular to the surface and with an angle against the oncoming flow. The height (h) of these blades is often slightly higher than the boundary layer thickness  $(\delta)$ .

Schubauer & Spangenberg (1960) tried a variety of wall-mounted devices to increase the mixing in the boundary layer. They did this in different adverse pressure gradients and concluded that the effect of mixing is equivalent to a decrease in pressure gradient. One year later Pearcy (1961) published a VG design guide. The focus of this work was primarily on shock-wave boundary layer interaction and how to reduce the separation strength behind the shock wave. However, the study also deals with the basics of VGs, such as co- and counter-rotating vortex pairs (see figure 1 for definitions) as well as various geometrical parameters and shapes. In general, the co-rotating arrays are more efficient in preventing separation, however, for blade spacings greater than three times their height Pearcy (1961) showed that the counter-rotating arrays are equally good.

Pearcy (1961) also analysed the movement of the streamwise vortices inside the boundary layer, using the inviscid analysis of Jones (1957). That analysis, which takes into account the mirror imaging of the vortex at the wall, shows that the vortices move away from the wall infinitely as they are convected downstream. Vortices in a counter-rotating pair with a common downflow, arranged in a larger array, will first move away from each other and towards the wall. As the vortex is getting closer to the next vortex originating from the neighbouring vortex pair it will be lifted away from the wall and asymptote to a constant in the spanwise direction. A new counter-rotating pair with common upflow is formed, which will continue to move away from the wall.

The evolution of a single vortex embedded in a turbulent boundary layer was thoroughly investigated by Shabaka, Mehta & Bradshaw (1985). The experimental results show that close to the wall the vortex induces vorticity, whose sign is opposite to that of the primary vortex. This induced vorticity was observed to be convected to the upwash side of the vortex. It is also stated that since turbulence is responsible for the diffusion of both the boundary layer and the vortices, their size ratio stays constant when moving downstream over the plate.

In a continuation Mehta & Bradshaw (1988) reported experiments with a counter-rotating vortex pair in the same basic set-up. The vortices had a common upflow from the surface and were initially embedded in the boundary layer, but due to the lift up motion the vortex centres had moved to around twice the boundary layer thickness from the wall at a certain downstream distance. Compared to the single vortex configuration the circulation of each vortex is

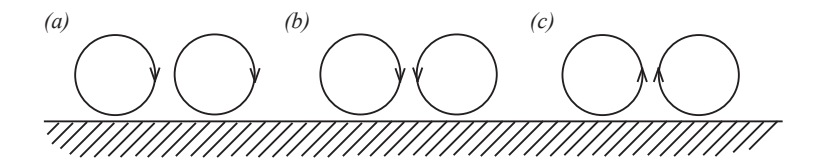


FIGURE 1. Different types of vortex pairs: (a) co-rotating, (b) counter-rotating with common downflow and (c) counter-rotating with common upflow.

about 20% stronger, which may be attributed to the constraint imposed of vortices acting as mirror images of each other. Throughout the test region there was little direct interaction between the vortices. Both in this study as well as in the study of the single vortex configuration the lateral meandering was shown to be small.

Another study of a single vortex in a boundary layer was performed by Westphal, Pauley & Eaton (1987). The vortex was produced by a delta wing that was slightly higher than the boundary layer thickness. They examined the vortex core area growth and showed that when the core radius reaches a certain fraction of the height of the vortex centre to the wall, the vorticity contours become elliptic in shape. This was hypothesized to be a sign of meandering, but no evidence of any lateral movement of the vortices was found. The overall circulation, when the vortex evolved downstream, either decreased slowly or remained almost constant, depending on the case. The APG results are reported both in Westphal, Eaton & Pauley (1985) and Westphal et al. (1987) and show an increased diffusion of vorticity and hence a more rapid vortex centre growth. The onset of vorticity contour flattening was accelerated by the pressure gradient. To investigate more thoroughly whether the ellipticity was caused by vortex meandering an experiment with a laterally oscillating VG was carried out by Westphal & Mehta (1989). The results indicate that the unforced vortex is laterally stable and also show that the initial meandering caused by the moving VG is damped as the vortex is convected downstream.

Pauley & Eaton (1988) examined the streamwise development of pairs and arrays of longitudinal vortices embedded in a ZPG turbulent boundary layer. In this study the blade spacing of VGs and the blade angle were varied, and the difference between counter-rotating vortices, with common upflow and downflow, and co-rotating vortices were examined. All configurations use blade heights well above the boundary layer thickness. The researchers state that the interaction of the secondary flow and the wall produces negative vorticity below the vortex. This vorticity is swept up on the side of the primary vortex to create a small region of opposite vorticity. The vortex centre movements in

the cross-plane are as expected from inviscid theory, although the paths are slightly modified by secondary flow structures. The proximity of other vortices does not affect circulation decay, but increases the diffusion of vorticity.

In most experiments the first measurements are taken at more than 10hdownstream of the VGs. In order to study the initial circulation and peak vorticity Wendt (2001) measured as close as one chord length downstream of the blade trailing edge of an array of VGs. Several counter- and co-rotating configurations were investigated by varying the aspect ratio, the blade length and the blade angle. The vortex strength was observed to be proportional to the free stream velocity, the blade angle and the ratio of the blade height and boundary layer thickness. With these three parameters held constant an increasing blade aspect ratio reduces circulation. In the study counter-rotating vortices show greater magnitudes of circulation than a single vortex produced with the same blade parameters. For co-rotating vortices the produced circulation is lower than for the single vortex. The circulation is shown to be accurately modelled by modified version of Prandtl's relation between circulation and airfoil geometry. In a previous work Wendt et al. (1995) studied the decay of counter-rotating vortices in approximately the same set-up. The vortices had their common flow directed upwards, and their distance to the wall increased as they evolved downstream. Thus the wall friction decreased, and the decay also decreased. The circulation decay is almost linear until a distance of 70h downstream the VG.

In most of the earlier studies VGs with  $h/\delta > 1$  have been used. However to reduce the drag penalty caused by the VGs, work has been done to reduce their size, without sacrificing efficiency. The comprehensive review of low-profile VGs by Lin (2002) shows that small  $(h/\delta \sim 0.2)$  VGs are just as effective in preventing separation as the normal-sized  $(h/\delta \sim 1)$  devices. It was concluded that low-profile VGs should be applied when the detachment point is relatively fixed, and the VGs can be positioned close to the separated region. Yao, Lin & Allan (2002) used stereoscopic particle image velocimetry (PIV) to compare a low-profile VG  $(h/\delta = 0.2)$  with a conventional one. In that study it was shown that the maximum vorticity generated increases as the angle of attack increases, from  $10^{\circ}$ , for the small VG, but it decreases with angle of attack for the large VG due to stall. Apart from this result there are no fundamental differences between the two VGs.

Godard & Stanislas (2006) made an optimization study of co- and counterrotating VGs submerged in the boundary layer. They concluded that triangular blades are better than rectangular blades, both in terms of vortex strength and drag. They also found that the counter-rotating set-up is twice as effective as the co-rotating in increasing the wall shear stress and that the optimum angle of attack is about 18°.

In another recent experiment Angele & Muhammad-Klingmann (2005) made extensive PIV measurements to show the flow and vortex development inside a turbulent boundary layer with a weak separation bubble. The bubble was controlled by VG arrays with different sizes (but all with  $h < \delta$ ). They concluded that the important parameter with respect to the efficiency of the VG is the circulation of the streamwise vortices. Although the circulation of the vortex may be hard to determine experimentally they found that it scales with the height of the generator blade and the velocity at its upper edge. Lögdberg (2006) later confirmed their findings and also showed that the separation is avoided altogether after only a small increase in circulation.

## 1.3. Layout of the paper

The present study complements earlier studies with embedded VGs in ZPG boundary layers through extensive hot-wire mapping of the flow field, for both for VGs giving a pair of counter rotating vortices and arrays of VGs. The flow behind yawed VGs, with respect to the base flow, was also investigated. An extended vortex model taking viscous effects into account was shown to give good agreement with the measured vortex motion.

Section 2 describes the wind tunnel set-up, the measurement technique and the VG family used. In  $\S 3$  the results regarding the downstream vortex development are given, and in  $\S 4$  results with yawed VGs with respect to the base flow are shown. The extended model for the vortex development is presented in  $\S 5$ , and the paper ends with conclusions in  $\S 6$ .

# 2. Experimental setup and flow condition

In this section the experimental setup in the MTL ("minimum turbulence level" or Mårten Theodore Landahl after its late initiator) wind tunnel is presented together with the VGs that were used and the techniques for flow visualization as well as velocity measurements. The section also treats the characterization of the base flow, i.e. a ZPG turbulent boundary layer, in which the streamwise evolution of vortices have been studied.

#### 2.1. Wind tunnel

The experimental investigation of the streamwise evolution of longitudinal vortices was carried out in the MTL wind tunnel, which is located at KTH Mechanics in Stockholm. This wind tunnel is of closed-circuit type and was designed with the aim to have a low background disturbance level. At the nominal velocity of  $U_0 = 25 \text{ m s}^{-1}$  the high pass filtered root mean square velocity values are less than 0.025%, 0.035% and 0.035% of the free stream velocity

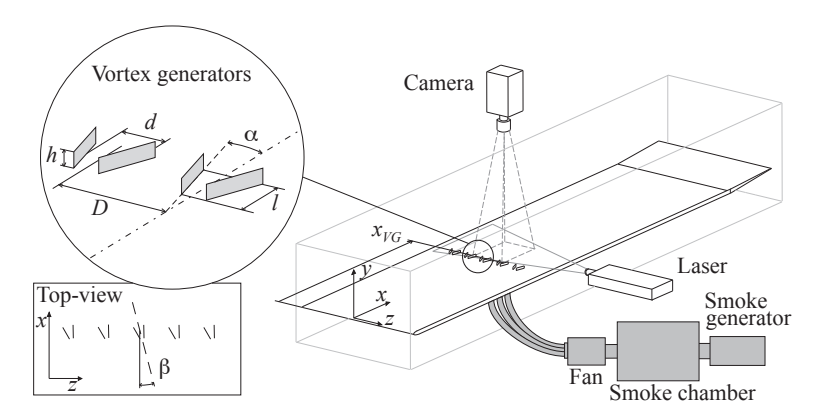


FIGURE 2. Sketch of the experimental setup, flow visualization arrangement and VG geometry.

in the streamwise, wall-normal and spanwise directions, respectively<sup>1</sup>. The air temperature can be regulated within  $\pm 0.05^{\circ}\mathrm{C}$  by means of a heat exchanger, which is located just upstream of the first corner after the axial fan (DC 85 kW). At the nominal velocity the total pressure variation is less than  $\pm 0.06\%$ . For further information regarding the flow quality in the MTL wind tunnel the interested reader is referred to Lindgren & Johansson (2002).

The test section is 7.0 m long and has a cross-sectional area of 1.2 m  $\times$  0.8 m (width  $\times$  height). A horizontal 5.8 m long flat plate, which spans the whole width of the test section, was mounted with its upper surface 0.51 m from the test section ceiling at the leading edge. The ceiling is adjustable in order to make compensating for the boundary layer growth possible and was here adjusted to give a zero streamwise pressure gradient at the nominal free stream velocity. The boundary layer was tripped by means of eight rows of Dymo tape embossed with the letter "V" at the flat plate leading edge to ensure a spanwise homogenous boundary layer transition. The plate was waxed to make it smooth, but no measurement of the surface roughness was performed, since this parameter was considered insignificant in this particular experiment.

A sketch of the experimental set-up is shown in figure 2. The coordinate system is chosen with the origin at the leading edge centreline of the plate, and the coordinates x, y and z correspond to the streamwise, wall-normal and spanwise directions, respectively.

<sup>&</sup>lt;sup>1</sup>The applied cutoff frequency was defined as  $f_c = U_0/\lambda_s$ , where  $\lambda_s$  is the sum of the two test-section side lengths, assuring that all disturbances with wavelengths fitting in the cross-sectional area are conserved.

The MTL wind tunnel is equipped with five degrees of freedom (x, y, z) and two angles  $\alpha$ ,  $\varphi$ ) traversing system operated with computer-controlled DC motors. This together with the feature of computer-controlled wind tunnel speed allow for fully automatic *in situ* X-probe calibration (§ 2.3). In the present set-up the probe was traversable in the following measurement volume:  $200 \lesssim x \lesssim 5300, \ 0 \leqslant y \leqslant 130 \ \text{and} \ -72.5 \leqslant z \leqslant 72.5 \ \text{(mm)}.$ 

#### 2.2. Flow visualization technique

The near flow development behind a spanwise pair and array of vortices was first investigated through smoke visualization. The smoke was obtained by heating a glycol-based liquid with a disco smoke generator (JEM ZR20 Mk II) and then led through ventilation tubing to a stagnation chamber (80 litre in volume). Two small DC regulated fans (12 V) were used to drive the smoke from the stagnation chamber to the 1 mm slot (205 mm in the spanwise extent) in the plate through five vinyl hoses creating a steady leakage of smoke through the slot. The smoke was illuminated by a laser sheet, approximately 2.5 mm thick, using a continuous Argon-ion laser (LEXEL 95–4) with a laser beam of 1.5 W and a cylindrical lens. The sheet was adjusted parallel to the plate, spanning the region 3.0 mm < y < 5.5 mm. At each visualized configuration 300 images were captured through the traversing system slit in the test-section ceiling with a CCD camera (1280 pixels × 1024 pixels). The image size in the physical x-z plane was 205 mm × 102 mm (cf. figure 2).

#### 2.3. Measurement technique

The velocity measurements were performed using hot-wire probes manufactured in-house with the anemometer operating in constant-temperature mode. Both a single-wire probe and X-probes were used for the measurements and were made from 5.0  $\mu$ m platinum wire with about 1 mm between the prongs. The probes were calibrated in situ, far outside the boundary layer, against a Prandtl tube. For the single-wire probe a modified King's law calibration function was used (cf. Johansson & Alfredsson 1982), and for the X-probe an angle calibration (-40° to +40°) was performed in the velocity range 7–28 m s<sup>-1</sup>. A surface fit, in the least squares sense, was applied to the data and used as a transfer function (see e.g. Österlund 1999). All three velocity components (U, V, W) could be measured through double grid-point traverse by using two boundary layer X-probes, one oriented for U-V and the other for U-W.

In the single-wire probe case the wall position was determined by decreasing the speed until a laminar boundary layer was achieved. Six wall-normal traverses, close to the wall, measuring the mean velocity in each position were used to linearly extrapolate the velocity down to zero, in that way determining the position of the wall with an estimated accuracy of 0.02 mm. In the case of the X-probe measurements the probe was photographed next to a precision

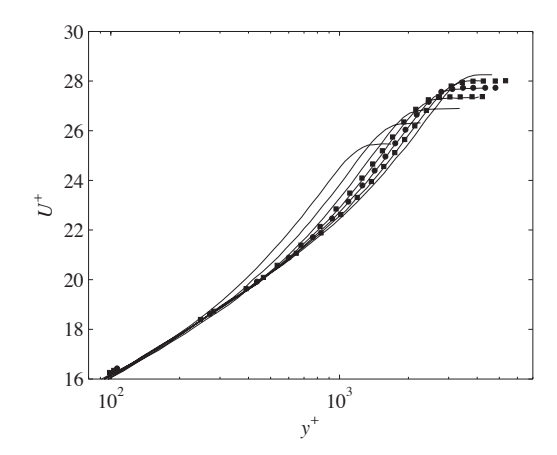


FIGURE 3. Mean streamwise velocity profiles in inner-law scaling for  $Re=3670,\ 5100,\ 6370,\ 7540,\ 8710,\ 9780$  and 10770 in the present ZPG turbulent boundary layer. Solid lines correspond to single-wire probe data and symbols to X-wire probe data, corresponding to  $Re=7540,\ 8710$  and 9780.

manufactured  $777 \pm 1~\mu m$  long cylinder, and then the wall distance was determined by measuring the probe position relative to the top of the cylinder on the photograph. With this method the wall position, relative the vertical centre of the probe, was determined with an estimated accuracy of 0.01 mm.

Normally seven y-z planes were measured downstream of each test configuration. In each measurement plane there were either 266 (19×14) or 322 (23×14) grid points. The traversing and collection of data were automatic and took approximately 14 hours for seven planes. Before every 14 hour run the calibration was checked against the wind tunnel Prandtl tube. Usually a new calibration had to be performed after two runs of seven planes.

The velocity data from an X-wire probe in a gradient perpendicular to the wires need to be corrected because the simplifying assumption of uniform velocity in the probe measurement volume is not fully valid. In this experiment the worst case appears when the probe is oriented to measure the U and W velocity components in the boundary layer. In this case the wires are at different y positions that causes the wire-normal velocities and hence the cooling velocities to differ considerably. Normally this does not produce any significant error in the U component which is proportional to  $E_1 + E_2$  (i.e. the sum of the voltages from wires 1 and 2) and thus a function of the mean cooling velocity in the measurement volume. The wall-normal/spanwise velocity component (V/W), on the other hand, is proportional to  $E_1 - E_2$ . This means that any velocity gradient in z/y will produce an erroneously measured velocity in V/W.

x	$U_{\infty}$	$u_{\tau}$	$1000  c_f$	Re	$\delta_1$	$\delta_2$	$H_{12}$	$\delta_{99}$
(mm)	$({\rm m}\ {\rm s}^{-1})$	$({\rm m}\ {\rm s}^{-1})$			(mm)	(mm)		(mm)
500	26.4	1.09	3.41	2260	1.88	1.28	1.47	10.4
1000	26.4	1.04	3.09	3670	3.02	2.08	1.45	17.2
1500	26.4	1.00	2.89	5100	4.01	2.89	1.39	23.7
2000	26.4	0.98	2.77	6370	5.04	3.60	1.40	29.9
2500	26.4	0.97	2.68	7540	5.97	4.26	1.40	35.9
3000	26.5	0.96	2.61	8710	6.78	4.90	1.38	41.6
3500	26.5	0.95	2.55	9780	7.66	5.51	1.39	47.5
4000	26.5	0.94	2.50	10770	8.63	6.07	1.42	53.2
4500	26.6	0.93	2.45	12200	9.62	6.86	1.40	60.2

TABLE 1. Description of the zero pressure gradient turbulent boundary layer. Here Re is based on  $\delta_2$ .

In the experiments reported here the data are corrected using the procedure described by Cutler & Bradshaw (1991). Only the mean velocity components V and W and the covariances  $\langle uv \rangle$  and  $\langle uw \rangle$  are corrected. In U the error is very small, and the correction terms of the velocity variances  $\langle u^2 \rangle$ ,  $\langle v^2 \rangle$  and  $\langle w^2 \rangle$  include terms not known from the measurements.

In figure 3 mean velocity profiles for different Reynolds numbers are shown for both single-wire (seven Reynolds numbers) and X-wire probes (three Reynolds numbers). The figure has been cut at about  $y^+=80$  in order to emphasize the comparison between the two probes. In order to assess an estimated error of the X-probe data compared to the single-wire data the standard deviations of the mean and root mean square values of the X-probe values as compared to the single-wire data, normalized by the respective maxima, were calculated. The results are  $(0.0011,\ 0.0012,\ 0.0014)$  and  $(0.0086,\ 0.0097,\ 0.0087)$  for the three Reynolds numbers in exceeding order, for the mean and root mean square standard deviations, respectively. This means that the mean values are measured within  $0.2\,\%$  of accuracy, and the root mean square values are measured within  $1\,\%$  of accuracy with the applied sampling time.

## 2.4. ZPG base flow

In this subsection it is shown that the present turbulent boundary layer that develops on the flat plate in the MTL wind tunnel has the characteristics that are typical of a ZPG turbulent boundary layer. For these measurements a single-wire probe was used (cf. § 2.3).

At all velocity measurements the free stream velocity  $U_{\infty}$  was set to 26.5 m s<sup>-1</sup>, and the temperature was kept constant at 18.1 °C. The variation of the free stream velocity was measured by traversing the probe along the test-section

VG	h  (mm)	d  (mm)	l  (mm)	D  (mm)	l/h	D/h	$h/\delta_{99}$	$U_h/U_\infty$
$VG_6$	6	12.5	18	50	3	8.33	0.22	0.74
$VG_{10}$	10	21	30	83	3	8.33	0.36	0.81
$VG_{18}$	18	37.5	54	150	3	8.33	0.65	0.92

TABLE 2. Physical dimensions of the VG sets used in the experiment together with some relative boundary layer measures. The last two columns are based on  $U_{\infty}=26.5~\mathrm{m~s^{-1}}$  and  $x=1830~\mathrm{mm}$  where  $\delta_{99}=27.8~\mathrm{mm}$ .  $U_h$  is the velocity at the tip of the VG. See figure 2 for a clarification of the parameters. Note that the subindex in VG stands for the height (h) of the vortex generator.

centreline at y=120 mm. The test-section ceiling was adjusted to give a velocity variation of less than 0.5%.

Wall-normal velocity profile measurements were performed at nine different streamwise positions from x=500 mm to x=4500 mm. According to Österlund (1999) the boundary layer is fully developed, in the sense that there exists a significant logarithmic overlap region, when the Reynolds number Re based on the momentum thickness ( $\delta_2$ ) is larger than 6000, and at  $Re \gtrsim 7000$  even the second-order moment of the pressure seems to be fully developed in a turbulent boundary layer (see Tsuji et~al.~2007). In the present experiment Re reaches a value of 6000 a small distance upstream of x=2000 mm.

The skin friction was not measured independently but calculated from Re using the equation

$$c_f = 2\left[\frac{1}{\kappa}\ln(Re) + C\right]^{-2} , \qquad (1)$$

which is derived from the logarithmic skin friction law. Österlund et al. (2000) fitted this relation to a large set of data obtained using oil-film and near-wall methods in the MTL wind tunnel. The values of the constants reported by Österlund et al. (2000) in this way are  $\kappa = 0.384$ , C = 4.08. When the skin friction is known the friction velocity can be calculated as  $u_{\tau} = U_{\infty} \left(c_f/2\right)^{1/2}$ . The main features of the streamwise evolution of the turbulent boundary layer are collected in table 1, and some quantities will be used for later comparison. Here, the so far non-defined boundary layer thicknesses are the displacement thickness ( $\delta_1$ ) and the thickness at which the velocity reaches 99 % of  $U_{\infty}$  ( $\delta_{99}$ ). The shape factor  $H_{12}$  is defined as  $\delta_1/\delta_2$ .

	Comment	ı	ı	1	1	•	1	1	1	1	U and $V$ comp.	U and $W$ comp.	1	U and $V$ comp.	U and $W$ comp.		1
	2.67	×	×	×					×		×			×		×	×
(m)	1.67	×	×	×					×		×			×		×	×
lanes (	1.17	×	×	×	×	×	×	×	×		×			×		×	×
x position of $yz$ -planes (m)	0.67	×	×	×					×		×			×		×	×
	0.42	×	×	×	×	×	×	×	×		×			×		×	×
$\int \int dx$	0.17	×	×	×					×					×		×	×
Į	90.0	×	×	×	×	×	×	×	×	×	×	×	×	×	×	×	×
	$\beta$ (°)	0	0	0	5	10	15	20	0	5	10	10	15	20	20	0	0
	Vortex generator	$VG_6^p$	$\mathrm{VG}^a_6$	$\mathrm{VG}_{10}^p$					$V{ m G}_{10}^a$							$VG_{18}^p$	${\rm VG}_{18}^a$

TABLE 3. All tested vortex generator configurations. The x-positions of the measured yz-planes correspond to the distance from the trailing edge of the vortex generator. Unless anything else is stated all three velocity components have been measured. Note that the supindices p and a in VG stand for the pair and the array configuration, respectively.

## 2.5. VGs and test configurations

In order to set up the streamwise vortices inside the turbulent boundary layer traditional square bladed VGs were used (see figure 2). Three different sizes of the VGs were used and arranged as both single spanwise pairs  $(^p)$  and spanwise arrays  $(^a)$  to create counter-rotating vortices inside the boundary layer. A summary of the dimensions and relative boundary layer measures are found in table 2. The blade angle  $\alpha$  was kept at 15°, and the design followed the criteria suggested by Pearcy (1961) for persistent streamwise existence of the vortices. The different VG sizes were geometrically "self-similar".

The spanwise extension of the arrays was between 660 mm and 750 mm, thus, they did not span the whole width of the test section, only 55%–63%. For the 6 mm, 10 mm, and 18 mm arrays (VG<sub>6</sub><sup>a</sup>, VG<sub>10</sub><sup>a</sup>, VG<sub>18</sub><sup>a</sup>) 13, 9 and 5 VGs were used, respectively. The vortex generators were mounted with the trailing edge of the blades at  $x_{VG} = 1830$  mm, where the boundary layer had reached an Re of approximately 6000 at the prescribed free stream velocity. This was to ensure a fully developed turbulent boundary layer and thus to avoid any peculiarities from the transition process.

The VG<sub>10</sub>, in both pair and array, was also tested varying the yaw angle  $\beta$  between 0° to 20° with an increment of 5°. In these experiments the yawing as performed on the individual VG pair, resulting in the VG tips in an array configuration being exposed to the same local velocity  $(U_h)$  (see figure 2). All tested configurations are summarized in table 3.

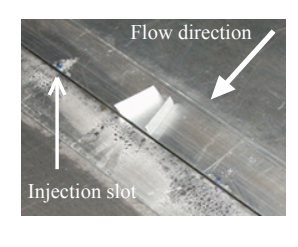
# 3. The flow field downstream of VGs: pairs vs arrays

# 3.1. Smoke visualization

The set-up for the smoke visualization is described in § 2.2 and was here used in the VG<sub>6</sub> configuration. Both a pair and an array of VGs were tested, which were mounted immediately upstream of the smoke slot (figure 4(a)). The free stream velocity was  $25 \text{ m s}^{-1}$ , and the camera exposure time was set to 0.10 ms for a good compromise between sensitivity and resolution. The bright vertical line, which can be seen in the figures 4(b) and 5 at  $(x - x_{VG})/h$  around 4, originated from the joint between the smoke injection insert and the flat plate, and was due to reflection of light. The case without vortex generators is seen in figure 4(b). The lower limit of the laser sheet was at y = 3 mm, and it was clear from the figure that the smoke was not diffused high enough from the plate to be illuminated by the laser until  $(x - x_{VG})/h$  about 7. Turbulent structures were seen in the interval  $(x - x_{VG})/h = 10$ –30, as would have been in a regular turbulent boundary layer.

A single image of the smoke visualization, taken of the configuration  $VG_6^p$  shown in figure 4(a), can be seen in figure 5(a). Since the smoke was lifted up to the laser sheet by the vortices, it could be seen instantly after the smoke injection slot. The vortices produced clear bands of smoke that are fairly steady

(a)



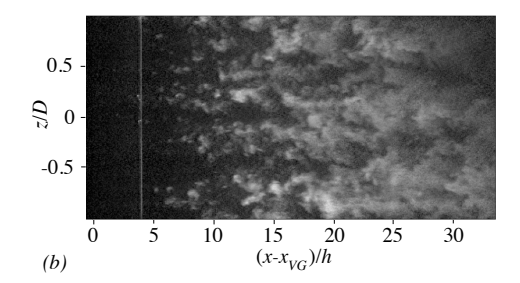


FIGURE 4. (a) A VG pair,  $VG_6^p$ , mounted upstream of the smoke injection slot. The flow direction is diagonal, from the upper right corner to the lower left. (b) An instantaneous image without VG. The smoke is injected at  $(x - x_{VG})/h = 0$  but is not visible until approximately  $(x - x_{VG})/h = 7$  when the smoke particles have been diffused high enough to be in the illuminated zone.

from image to image. When VGs were added to the single pair to form an array,  $VG_6^a$ , the smoke bands from the neighbouring VGs seemed to converge around  $(x - x_{VG})/h = 25$  (see figure 5b).

Figure 5(c,d) shows the result of averaging 300 images in the  $VG_6^p$  and the  $VG_6^a$  configuration, respectively. This produces images in which the light intensity indicates the averaged position of the smoke band. A least squares fit was made to the light intensity peaks of each pixel column to produce the white dashed lines. Note that the lines do not show the paths of the vortex centres. It is rather the position of the maximum positive mean velocity in V at y=3–5.5 mm. Thus the vortex centre paths are located somewhere between the white lines (which will be shown in § 5).

In figure 6 the spreading of the two dashed lines from figure 5(c,d) are compared. Furthermore, the light intensity variation across the image is also shown at a number of x positions. The reduction of the peak height, with increasing x, is a combination of smoke diffusion and an increase in vortex size. Somewhat surprisingly, the lines for the  $VG_6^p$  and the  $VG_6^a$  seem to collapse, but it should be noted that in the area in which they are expected to deviate, i.e. the most downstream part of the image, the smoke density is getting lower and the results are less reliable.

The important result from this near wake flow visualization is that there is no substantial difference in the evolution of vortices between the VG pair and array configurations at least up to  $(x - x_{VG})/h$  of about 35.

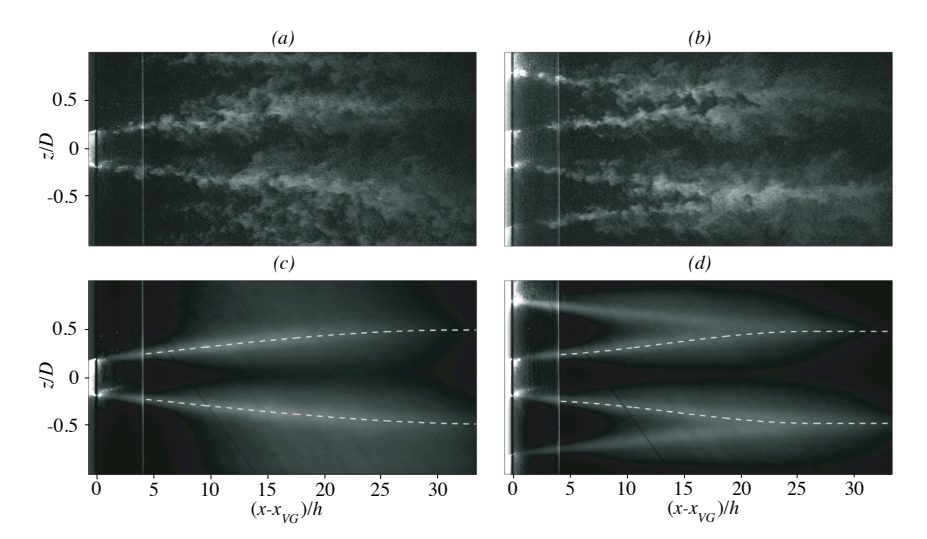


FIGURE 5. Instantaneous images at 25 m s<sup>-1</sup> with the configurations (a)  $VG_6^p$  and (b)  $VG_6^a$  (c), (d) The corresponding averaged images. Dashed lines indicate the spreading of the peak in light intensity, which corresponds to the position of the maximum positive mean wall-normal velocity component.

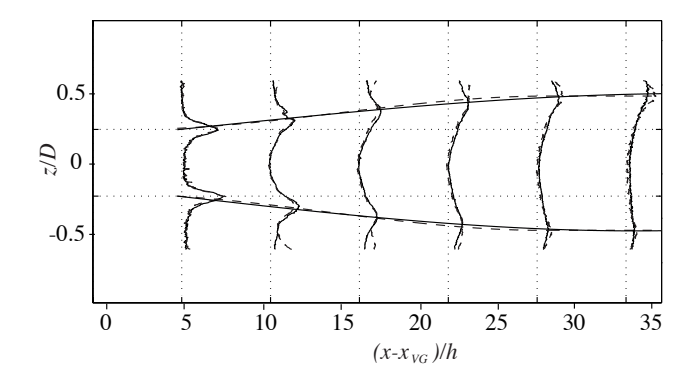


FIGURE 6. The white dashed lines from figure 5 (c, d) superimposed on each other. The solid line is the  $VG_6^p$  configuration, and the dashed line is the  $VG_6^a$ . Also shown is how the light intensity varies in the spanwise direction at six x positions.

## 3.2. Mean flow

The vortex generators set up strong vortices which modified the base flow. In figures 7 and 8 the three mean velocity components are the plotted contours of

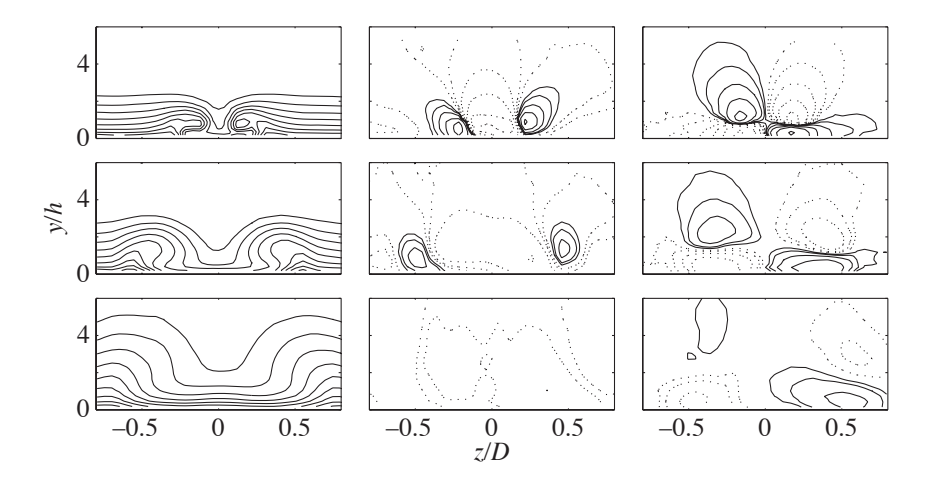


FIGURE 7. All three mean velocity components (from left to right, streamwise, wall normal and spanwise) in the boundary layer in the VG<sup>p</sup><sub>10</sub> configuration. From top to bottom the rows correspond to  $(x-x_{VG})/h=6$ , 42 and 167, respectively. The contour levels for  $U/U_{\infty}$  are (0.05:0.05:0.95). For  $V/U_{\infty}$  the levels  $[-10^{(-\frac{3}{3}:\frac{1}{3}:-\frac{7}{3})}; 10^{(-\frac{7}{3}:\frac{1}{3}:-\frac{3}{3})}]$ ,  $[-10^{(-\frac{4}{3}:\frac{1}{3}:-\frac{7}{3})}; 10^{(-\frac{7}{3}:\frac{1}{3}:-\frac{7}{3})}]$  and  $[-10^{(-\frac{5}{3}:\frac{1}{3}:-\frac{7}{3})}; -1]$  are plotted for the exceeding downstream positions, respectively. The corresponding contour levels for  $W/U_{\infty}$  are  $[-10^{(-\frac{2}{3}:\frac{1}{3}:-\frac{7}{3})}; 10^{(-\frac{7}{3}:\frac{1}{3}:-\frac{2}{3})}]$ ,  $[-10^{(-\frac{4}{3}:\frac{1}{3}:-\frac{7}{3})}; 10^{(-\frac{7}{3}:\frac{1}{3}:-\frac{5}{3})}]$ . Positive and negative contour levels are plotted with solid and dotted lines, respectively.

the VG<sub>10</sub> pair and array configurations, respectively. It can be observed that even after the corrections described in § 2.3 some error in the V component is present. This is due to the difficulty in applying the appropriate correction when there are large velocity gradients in all cross-flow directions (see § 2.3 and the discussion therein). The U and W components are symmetric; however the asymmetry in the V component is due to the large velocity gradients which affect the cooling velocities of the two wires of the X-probe differently. The maximum magnitude of the cross-flow components are approximately 15% of  $U_{\infty}$  in V and 26% in W at  $(x-x_{VG})/h=6$  for a VG pair. For the VG array they are 13% and 26%, respectively. At this x position both V and W are symmetric in the sense that the negative and the positive velocities are of the same magnitude and are expected to be even larger closer to the VGs. The cross-flow components decrease with downstream distance as the vortex grows.

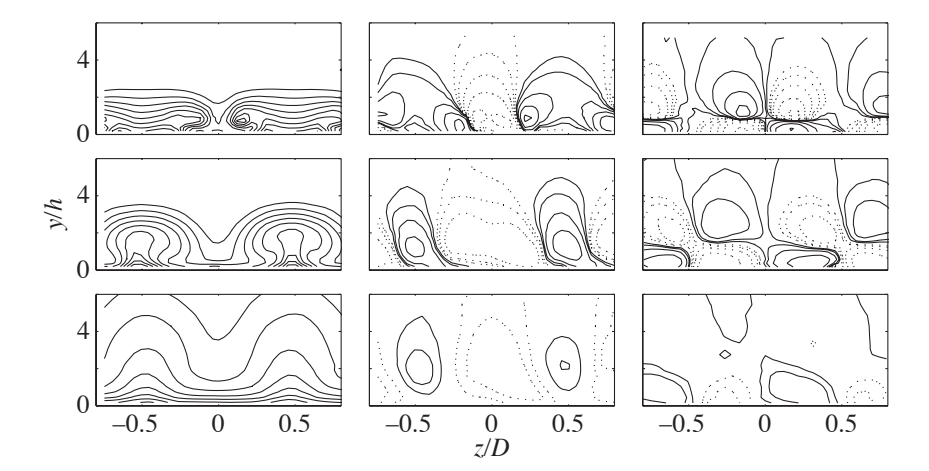


FIGURE 8. Same as in figure 7 but for the VG\$^a\_{10}\$ configuration. The contour levels for  $U/U_{\infty}$  are (0.05:0.05:0.95). For  $V/U_{\infty}$  the levels  $[-10^{(-\frac{3}{3}:\frac{1}{3}:-\frac{7}{3})}; 10^{(-\frac{7}{3}:\frac{1}{3}:-\frac{3}{3})}], [-10^{(-\frac{5}{3}:\frac{1}{3}:-\frac{7}{3})}; 10^{(-\frac{7}{3}:\frac{1}{3}:-\frac{6}{3})}]$  are plotted for the exceeding downstream positions, respectively. The corresponding contour levels for  $W/U_{\infty}$  are  $[-10^{(-\frac{2}{3}:\frac{1}{3}:-\frac{7}{3})}; 10^{(-\frac{7}{3}:\frac{1}{3}:-\frac{2}{3})}]$ ,  $[-10^{(-\frac{4}{3}:\frac{1}{3}:-\frac{7}{3})}; 10^{(-\frac{7}{3}:\frac{1}{3}:-\frac{4}{3})}]$  and  $[-10^{(-\frac{6}{3}:\frac{1}{3}:-\frac{7}{3})}; 10^{(-\frac{7}{3}:\frac{1}{3}:-\frac{6}{3})}]$ . Positive and negative contour levels are plotted with solid and dotted lines, respectively.

As far downstream as  $(x - x_{VG})/h = 267$  (not shown here), the ranges<sup>2</sup> of V and W are however still 1.8 % and 3.2 % of  $U_{\infty}$  in the VG<sup>p</sup> case and 2.3 % and 2.4 % in the VG<sup>a</sup> case.

The mean velocities of a  $VG^p$  case (figure 7) can be compared to that of an array in figure 8. Most noticeable is the larger symmetry in the  $VG_6^a$  case for all three velocity components. With an array of VGs there is a small increase in the boundary layer thickness. For counter-rotating vortices the V component of the neighbouring vortices is added, and thus it persists further downstream. For W the effect of the array is the opposite, and this velocity component decays faster compared to the VG pair case. Both effects are clearly visible in the figures.

For control purposes the induced drag due to the presence of the VGs is an important factor, which has to be taken into account as a cost in any

 $<sup>^2</sup>$ At  $(x-x_{VG})/h=267$  the V component no longer has positive and negative velocities of the same magnitude due to the boundary layer growth. Hence, the range between the maximum and the minimum values becomes a better measure than the magnitude, when comparing with the still-symmetric W component.

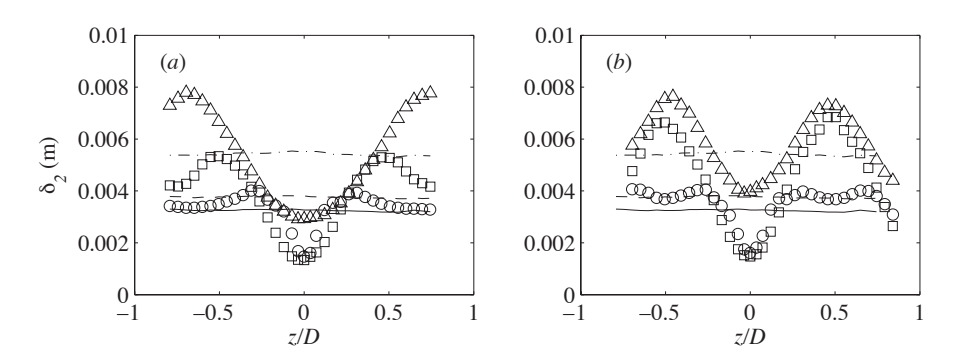


FIGURE 9. Spanwise distribution of the momentum thickness for different downstream positions with (symbols) and without (lines) VGs. (a) The VG<sup>p</sup><sub>10</sub> configuration. (b) The VG<sup>a</sup><sub>10</sub> configuration. The symbols and lines –  $\bigcirc$  solid,  $\square$  dashed and  $\triangle$  dash-dotted – correspond to  $(x - x_{VG})/h = 6$ , 42 and 167, respectively.

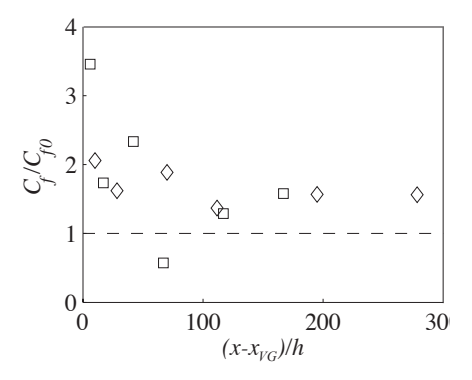


FIGURE 10. Streamwise distribution of the spanwise-averaged local skin friction coefficient  $(c_f)$ . The  $\Diamond$  and  $\square$  symbols correspond to  $VG_6^a$  and  $VG_{10}^a$ , respectively. The subindex 0 denotes the case without VGs.

performance improvement estimation. Here, we have calculated the spanwise-averaged local skin friction  $(c_f)$  by considering the momentum loss for the array case by integrating over one spanwise period  $(\lambda)$  according to

$$c_f(x) = 2\frac{\tau_w}{\rho U_\infty^2}$$
, with  $\tau_w(x) = \rho U_\infty^2 \frac{\mathrm{d}\delta_2^z(x)}{\mathrm{d}x}$  and  $\delta_2^z(x) = \frac{1}{\lambda} \int_{-\lambda/2}^{\lambda/2} \delta_2(x,z) \mathrm{d}z$ .

The streamwise derivative of the momentum thickness in the expression for  $\tau(x)$  was approximated by a forward-step finite difference. In figure 9 the spanwise distribution of the momentum thickness is shown for both (a) the pair and (b) the array cases with h=10 and at three different downstream positions. One may observe that the boundary layer modulation due to the VGs is different for the pair and the array cases as also concluded from figures 7 and 8. From figure 9 it is clear that the level of modulation peaks earlier, i.e. closer to the VGs, for the VG<sup>a</sup> case compared to the VG<sup>p</sup> case but not necessarily at a higher level. This is realized by comparing the two most downstream positions,  $(x-x_{VG})/h=42$  and 167. Finally, in figure 10 the spanwise-averaged local skin friction is plotted versus the downstream distance for the VG<sup>a</sup><sub>6</sub> and the VG<sup>a</sup><sub>10</sub> cases. The skin friction coefficient is normalized with the local ZPG turbulent boundary layer case without VGs, which gives a direct measure of the cost (i.e. increased drag) along the plate.

## 3.3. Vortex centre paths

There exist a number of different methods for vortex indentification; for a review see Jeong & Hussain (1995). In this particular case the vortex centre is defined as the position of the maximum absolute streamwise vorticity  $|\omega_x|_{max}$ . This method would give the same result as the Q method proposed by Hunt et al. (1988), i.e. by identifying the maximum positive values of the second invariant of the velocity gradient tensor denoted by Q, since the background shear in the turbulent boundary layer of the position of the vortex cores is weak compared to the vorticity magnitude within the vortex. The vortices generated by VGs are relatively strong and steady, implying that any method would work well. The second invariant Q is defined as  $1/2 \left(U_{i,i}^2 - U_{i,j}U_{j,i}\right)$ , and the streamwise component becomes

$$Q_x = -\frac{1}{2} \frac{\partial W}{\partial y} \frac{\partial V}{\partial z} , \qquad (2)$$

to which we will come back later.

In order to determine the vortex centres a simple interpolation scheme was used. To find the vortex centres of each plane the data positions of the maximum and minimum streamwise vorticities were identified, for the positively and negatively rotating vortices respectively. Then, a cubic surface fit was applied on the surrounding 24 points ( $\pm 2$  in y and z) and a new  $20 \times 20$  matrix, with higher spatial resolution, was produced in which a new maximum or minimum was found. Since the peak of maximum absolute vorticity is getting flatter as the vortices are convected downstream, and the vorticity is diffused so that the area of the vortex core is increased, the position of maximum/minimum vorticity becomes more diffused. Thus the vortex centre coordinates get less precise with increasing x.

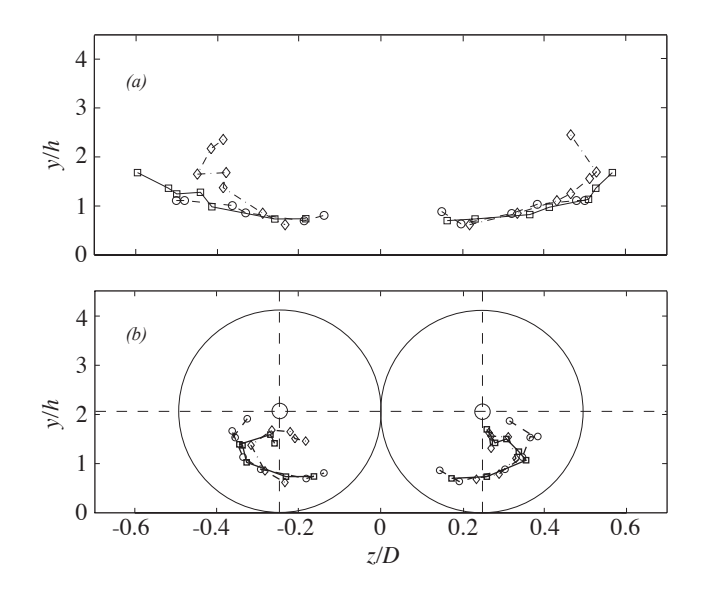


FIGURE 11. Vortex centre paths plotted in a y-z plane normal to the stream:  $-\cdot \lozenge \cdot -$ , ----, --- denote VG<sub>6</sub>, VG<sub>10</sub> and VG<sub>18</sub>, respectively. (a) The paths downstream of a VG pair. (b) The same planes for an array of VGs .

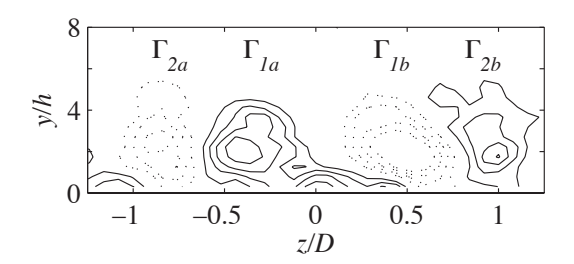


FIGURE 12. Contours of  $\omega_x/(U_\infty/h)$  in the y-z plane at  $(x-x_{VG})/h=278$ , downstream of a 6 mm VG pair;  $\Gamma_1$  and  $\Gamma_2$  denote the circulation of the primary and secondary (induced) vortices. The solid lines indicate positive vorticity with contour levels  $(2.5:2.5:10)\times 10^{-3}$  and the dashed lines negative vorticity with contour levels  $(-10:2.5:-2.5)\times 10^{-3}$ .

In figure 11(a) the vortex centre paths from VG pairs are projected on the y-z plane. The three curves do not start on the same streamwise location, since the first data point in each case are not located at the same normalized streamwise position,  $(x - x_{VG})/h$ . The paths of the vortices behind the VG<sup>p</sup><sub>10</sub>

and the  $VG_{18}^p$  seem to collapse nicely over each other. Progressing downstream these vortex paths move away from each other; at first one may observe a small approach towards the wall which is followed by a steady rise until the last measured streamwise position. This can be understood using the same reasoning as Pearcy (1961), based on potential flow theory, for VG arrays. The downward motion in the beginning is caused by the induced velocity by the neighbouring real vortex, which leads to a stronger induced force away from each other due to the mirrored vortices at the plate. However, as the two vortices move away from each other the former influence becomes weaker, and the growth of the vortex causes the vortex centre to move away from the wall. An interesting behaviour of the  $VG_6^p$  vortex path is that, after about  $(x - x_{VG})/h = 200-250$ , it makes an unexpected turn and starts to approach its neighbour. An explanation of this peculiarity will be given below.

The corresponding vortex paths of the VG arrays are shown in figure 11(b), and it is seen that they look similar to the  $VG_6^p$  case. First they move apart and towards the wall due to the same reason as in the VG pair case. But in the case of the array, when they move away from each other they are moving closer to the vortex from the neighboring vortex pair and eventually form a new counter-rotating pair – this time with common upflow. The induced velocities in the new pair will tend to lift the vortices, and according to the inviscid theory (Jones 1957) they will continue to rise from the wall with a constant slope, along an asymptotic value of z/D in the horizontal plane. However, the measurements show that the vortex centre paths of the original pair, while still rising, start to move towards each other again. This is probably due to vortex growth; when the area of the vortex grows the vortices are forced to a spanwise equidistant state. The influence from the other vortices (real or mirrored) is decreasing with increasing downstream distance. At  $(x - x_{VG})/h = 50$  the circulation is reduced to half of the initial value and thus the induced flow is equally reduced. Since the distance between the VG pairs in an array is D, and each VG pair produces two vortices, the maximum vortex radius in an equidistant system of circular vortices is D/4. If the distance from the vortex centre to the wall is D/4, the induced velocities from the real vortices and the three closest mirrored vortices all cancel. The following mirrored vortex images will produce small, alternating positive and negative forces in the spanwise direction, and the system will be close to balanced. In these experiments D/h = 8.33 (cf. table 2), and thus D/4 = 2.08h. Hence, if the assumption holds, the vortex centres should approach  $(y/h, z/D) = (2.08, \pm 0.25)$ . In figure 11(b), these coordinates are marked with small circles, whereas the large circles show the maximum size of a circular spanwise equidistant vortex. There seems to be a tendency for the vortex centres to move towards the predicted position.

Now, one can understand the peculiar vortex centre path produced by the  $VG_6^p$  in figure 11(a). Analogous to the paths of the vortices generated

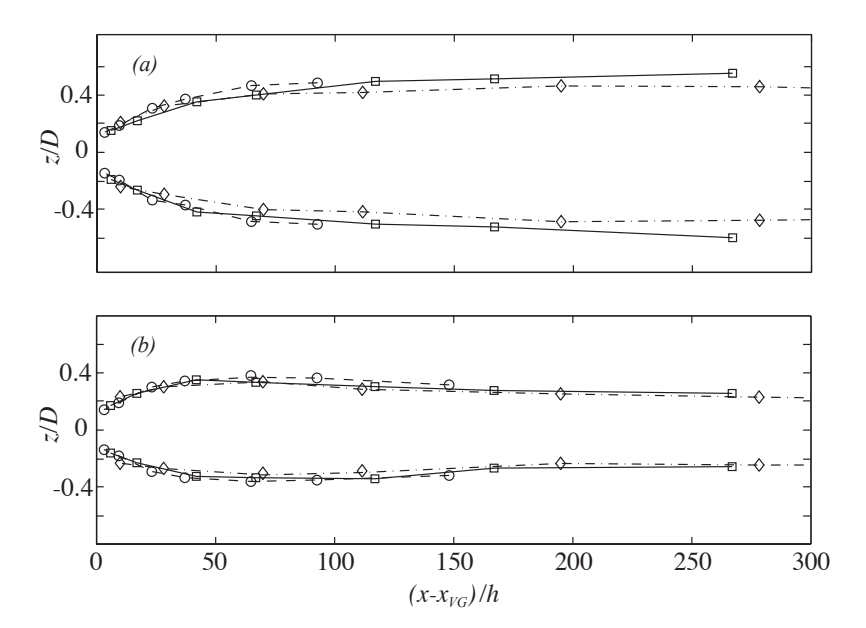


FIGURE 13. Vortex centre paths plotted in plan view (the x-z plane):  $-\cdot \lozenge \cdot -$ ,  $-\Box -$ ,  $-- \bigcirc -$  denote  $h_{VG}=6$  mm, 10 mm, 18 mm. (a) The paths downstream of a pair of vortex generators. (b) The same planes for a VG array. Note that for the array the paths of the neighbouring vortices are actually within the figure area, but for the sake of clarity they are not shown.

by the array, the curving back motion appears to indicate the existence of more vortices, outside of the primary pair. The three most downstream planes,  $(x-x_{VG})/h=\{194,\ 278,\ 445\}$ , certainly show two more vortices flanking the original ones. The new induced secondary vortices are relatively strong; at  $(x-x_{VG})/h=194$  their circulation is about 25% of the primary vortices, and at  $(x-x_{VG})/h=278$  they have reached a strength close to 50%. At  $(x-x_{VG})/h=445$  a small part of the secondary vortices is outside the measurement plane, but the major part is inside, and the circulation is about 55% of the primary vortices. Note that the circulation of the primary vortices has ceased to decay in this region and that the secondary vortices thus not only increase in strength relative to the primary vortex pair but also grow in absolute numbers. Partly this is due to their increasing distance from the wall, moving more of the secondary vortices into the measurement plane, but the major increase in circulation is due the continuous vorticity transfer from the primary vortices close to the wall to the upwash regions. In figure 12, the plotted vorticity

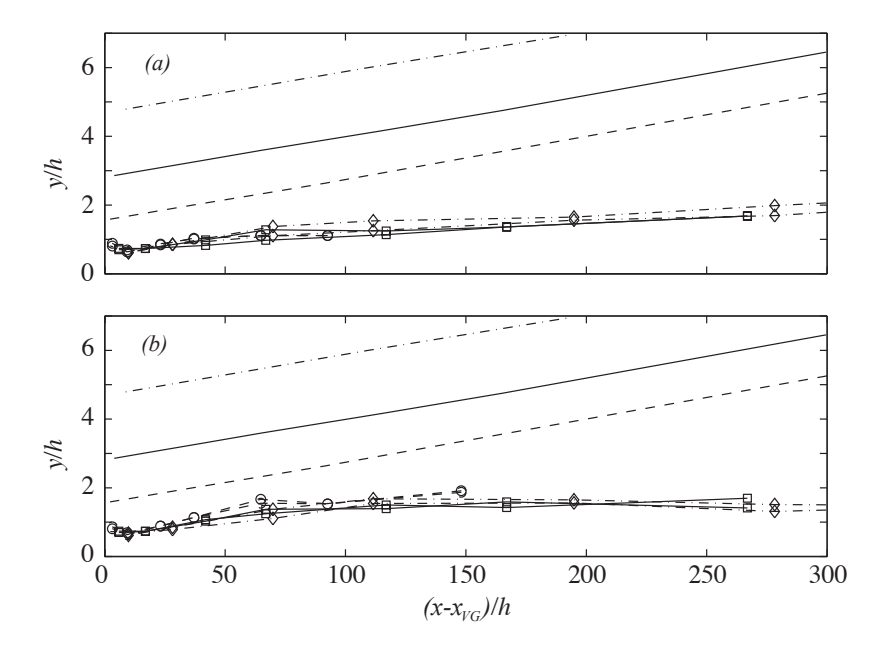


FIGURE 14. Vortex centre paths plotted in a plane parallel to the stream (the x-y plane):  $-\cdot \lozenge \cdot -$ ,  $-- \bigcirc -$ ,  $-- \bigcirc -$  denote  $h_{VG}=6$  mm, 10 mm, 18 mm. (a) The paths downstream of a pair of VGs. (b) The same planes for a VG array. The dash-dotted line shows the boundary layer thickness in the 6 mm case; the solid line is the 10 mm case; and the dashed line is the 18 mm case. Note that the scale of the y-axis is more than 10 times that of the x-axis.

contours reveal the existence of an outboard pair of induced secondary vortices at  $(x - x_{VG})/h = 278$ .

The secondary vortices originate from the very thin layer of stress-induced opposing  $\omega_x$  under the primary vortex. This layer is too thin to be detected in the experiments reported here but is described in Shabaka *et al.* (1985). According to Pauley & Eaton (1988) there is some evidence that the layer of opposing vorticity is convected out to form a small low-momentum region of opposing vorticity on the upflow side of the main vortex and close to the wall. To the authors knowledge it has never been shown before how this induced vorticity is rolled up into a vortex that rises up from the wall to influence the vortex centre path of the primary vortex.

In figure 13(a) the vortex paths from the single VG pair are shown in plan view. The paths from the VG<sub>6</sub><sup>p</sup> continue to  $(x - x_{VG})/h = 445$ , but in order not to compromise the resolution the figure is cut at  $(x - x_{VG})/h = 300$ . This

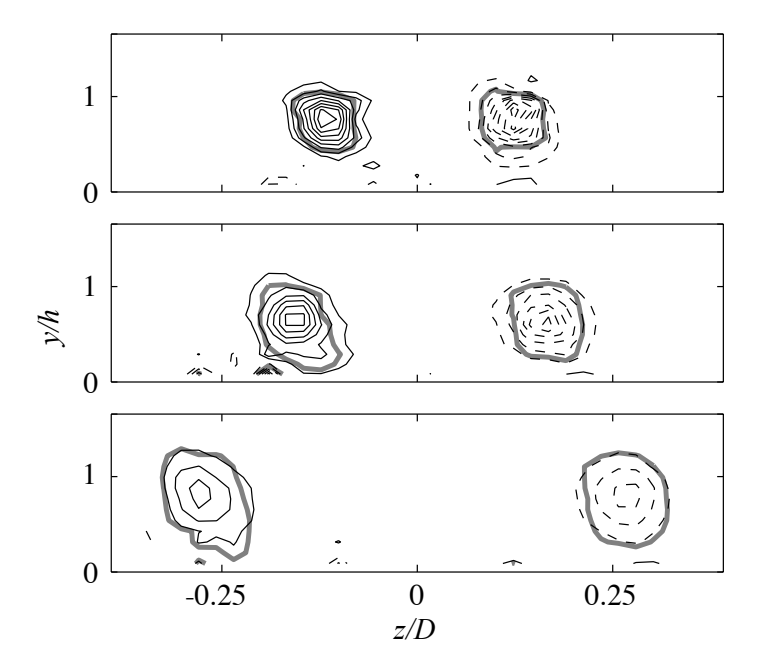


FIGURE 15. Contours of  $\omega_x/(U_\infty/h)$  in the first three planes behind the  $VG_{18}^p$  configuation. The dashed and solid contour levels correspond to (-1.8:0.2:-0.2) and (0.2:0.2:1.8), respectively. The thick contour line represents  $Q_x=0.05\,Q_x^{max}$  and encompasses the vortex core area A.

also applies to figures 13(b) and 14. A divergence of the paths, from all VG sizes, caused by the mirrored images can be observed. The angle of divergence seems to increase with vortex strength.

Vortex centre paths downstream of VG arrays are plotted in figure 13(b). These paths scale better than the VG<sup>p</sup> paths, using D in the spanwise and h in the streamwise directions. In plan view it is easy to see how the paths first move apart, roughly at the same rate as in the case of the single pairs, up to about  $(x - x_{VG})/h = 50$  and then how they converge towards the asymptotic spanwise location of  $z/D = \pm 0.25$  as discussed earlier.

Shabaka et al. (1985) suggested that since turbulence diffuses both the boundary layer and the vorticity the proportion between vortex size and boundary layer thickness should remain constant at all x stations for isolated vortices in a boundary layer. For a circular vortex, this implies a vortex centre that moves away from the wall with the increase of the boundary layer thickness. According to the inviscid analysis by Jones (1957) the interaction of the vortex pairs will make them move away from the wall linearly after an initial approach

towards the wall. Earlier in this section it was suggested that the vortex centres will move towards a constant height y=D/4. In figure 14 the vortex centre paths are plotted on a plane parallel to the stream. These paths seem to scale with h and in the figure the boundary layer thicknesses  $(\delta_{99})$  for the different VG sizes are also plotted. It is clear from the figure that the vortex centre height does not scale with the boundary layer thickness regardless of configuration. The paths seem to scale with h. The single pairs in figure 14(a) continue to rise through the test section, but the corresponding array centres in figure 14(b) seem to reach a constant height of y/h=1.5-2. This range is close to the asymptotic value of y/h=2.08 from the hypothesis of asymptotic path values stated above. When the wall-normal positions of the vortex centres are closer to the wall than D/4 the induced velocities from the mirrored images produce a force towards the neighbouring vortices with a common outflow. However the paths in figure 11(b) and 13(b) show no tendency to diverge. Thus there must be an opposing force.

## 3.4. Vortex strength decay

According to Kelvin's circulation theorem the circulation around a closed material circuit in an inviscid fluid is conserved. Thus the circulation would remain constant as the vortices are convected downstream from the VGs. In the present experiment the no slip condition at the wall generates a spanwise shear stress component that reduces the angular momentum, and hence the circulation, of the vortex.

The vortex circulation is calculated by integrating the streamwise vorticity over the area A according to

$$\Gamma = \int_{A} \omega_x \, \mathrm{d}A \,\,, \tag{3}$$

where A is defined as the area enclosed by the contour  $Q_x = 0.05 \, Q_x^{max}$  (cf. (2)). Note that  $Q_x^{max}$  refers to the local maxima in the measured plane. The choice of cutoff level was chosen after some consistency tests. Figure 15 shows the evolution of the vortex areas of three measurement planes. Since the aspect ratio and the angle of attack are the same for all three VG sizes it is appropriate to normalize the circulation by the height h and the streamwise velocity at the blade tip  $U_h$ .

In figure 16(a,b) the downstream development of circulation for the 6 mm, 10 mm and 18 mm VGs are shown for the pair and the array cases, respectively. Here, the clearly identified asymptotic value in a linear plotting has been subtracted from the data. In (a) the three curves collapse well, and down to  $(x-x_{VG})/h \approx 200$  the circulation seems to decay exponentially. The same exponential decay is achieved with VG arrays, at least up to  $(x-x_{VG})/h \approx 100$ , as can be seen in (b).

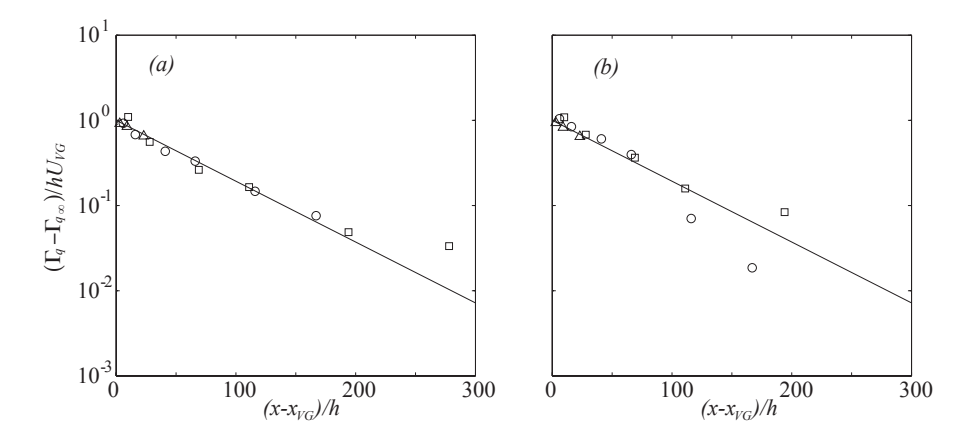


FIGURE 16. The vortex strength decay of the (a) VG<sup>p</sup> and (b) VG<sup>a</sup> cases. The symbols  $\Diamond$ ,  $\Box$  and  $\circ$  denote  $h_{VG} = 6$  mm, 10 mm and 18 mm. The solid lines correspond to the exponential decay exponent -0.0164.

#### 3.5. Turbulence quantities

In this section the velocity variances and covariances of the accessible components from the two X-probes are shown for the  $VG_10^p$  and  $VG_10^a$  cases. It may be observed from figures 17 and 18, which show all three velocity variance components for the pair and array configuration, respectively, that the maxima of  $\langle v^2 \rangle / U_{\infty}^2$  and  $\langle w^2 \rangle / U_{\infty}^2$  follow the location of the strongest velocity shear of their respective mean velocity components. The streamwise velocity variance component is the largest of the three for both the pair and the array configurations with a value just below  $15 \times 10^{-3}$  close to the VGs when normalized with  $U_{\infty}^2$ . However, the high fluctuation level decays close to the VGs and reaches a constant level of  $\langle u^2 \rangle/U_{\infty}^2$  around  $6 \times 10^{-3}$  from about  $(x-x_0)/h=150$ and beyond. In figure 19 the streamwise evolution of the turbulence quantities are plotted, and an undershoot of the decay may be observed with the minima for all three velocity variance components around  $(x-x_0)/h=40$ . This undershoot is the strongest for the spanwise component, which behaves as the streamwise component but shifts somewhat to a lower fluctuation level. The undershoot is an artefact of the second outer maximum in the y-z plane of all three velocity variance components, which is well developed around  $(x-x_{VG})/h$ = 42 (cf. figures 17 and 18). A shift from the inner peak to the outer peak being the largest gives rise to the undershoot. Similar explanation applies for the observed undershoot of the  $-\langle uv \rangle$  covariance component, which however is not revealed in figures 20 and 21. On the other hand at  $(x-x_{VG})/h=17$  (not shown here) there are two clear negative outer peaks of  $\langle uv \rangle/U_{\infty}^2$ , which merge downstream, and at  $(x - x_{VG})/h = 42$  only a single outer peak is observed (cf.

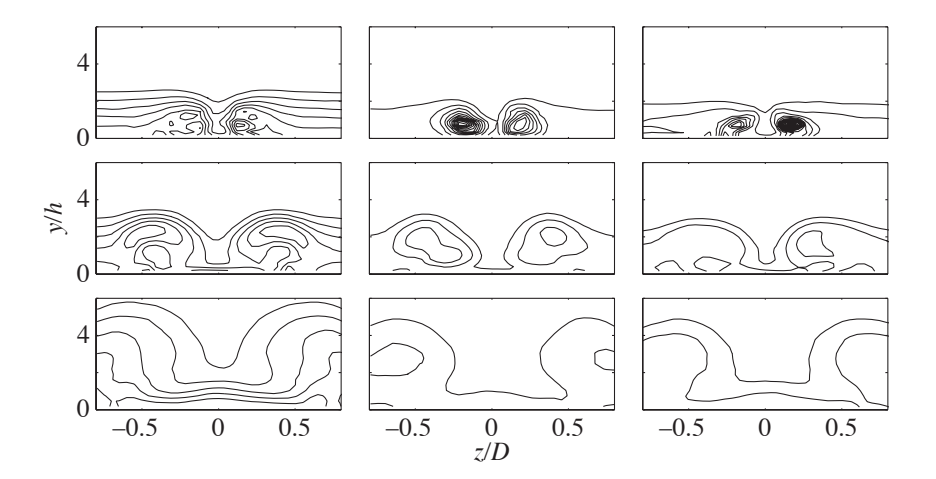


FIGURE 17. Contours of all three velocity variance components. From left to right,  $\langle u^2 \rangle/U_\infty^2$ ,  $\langle v^2 \rangle/U_\infty^2$  and  $\langle w^2 \rangle/U_\infty^2$ , in the boundary layer for the VG $_{10}^p$  configuration. From top to bottom the rows correspond to  $(x-x_{VG})/h=6$ , 42 and 167, respectively. The contour levels are  $(1:1:8)\times 10^{-3}$  for  $\langle u^2 \rangle$  and  $(1:0.5:8)\times 10^{-3}$  for  $\langle v^2 \rangle$  and  $\langle w^2 \rangle$ .

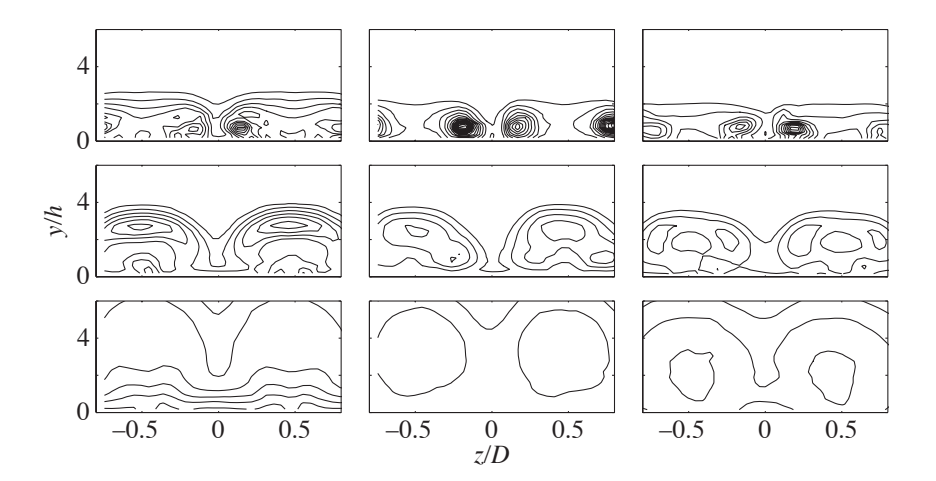


FIGURE 18. Same as in figure 17 but for the VG\$^a\_{10}\$ configuration. The contour levels are  $(1:1:10)\times 10^{-3}$  for  $\langle u^2\rangle$  and  $(1:0.5:10)\times 10^{-3}$  for  $\langle v^2\rangle$  and  $\langle w^2\rangle$ .

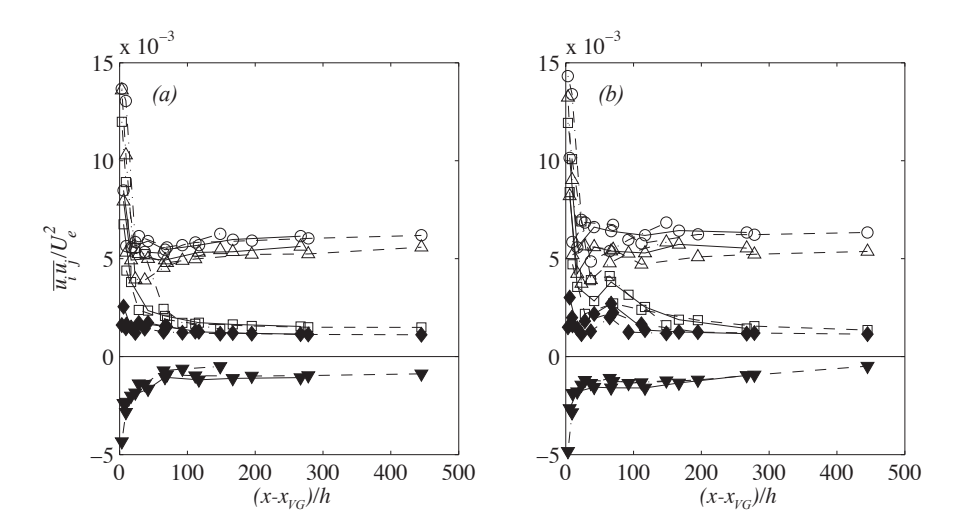


FIGURE 19. Streamwise evolution of the maximum values of the turbulence quantities shown in figures 17–21, but for all VG heights. (a) and (b) correspond to the pair and the array configurations, respectively.  $(\bigcirc, \Box, \triangle, \blacklozenge, \blacktriangledown)$  correspond to  $\max_{yz} \{\langle u^2 \rangle/U_\infty^2, \langle v^2 \rangle/U_\infty^2, \langle w^2 \rangle/U_\infty^2, -\langle uv \rangle/U_\infty^2, -\langle uw \rangle/U_\infty^2\}$ , respectively.

figures 20 and 21). Worth mentioning is that the wall-normal velocity variance component is only  $25\,\%$  of the others after the initial decay.

Furthermore, the larger term of the streamwise production of turbulence is  $-\langle uv\rangle\partial U/\partial y$  as compared to the  $-\langle uw\rangle\partial U/\partial z$  term. From figure 19 it is observed that the maxima in  $-\langle uv\rangle$  and  $-\langle uw\rangle$  are of opposite signs but "equal" magnitudes. The regions of the covariance maxima and their corresponding velocity gradient maxima (cf. figures 20 and 21) appear to coincide in the cross-flow plane. The gradient  $\partial U/\partial z$  has its maximum at the centre of the vortex and is zero at the outflow and inflow positions with a corresponding minimum and maximum in U, respectively, where it also changes signs. On the other hand the gradient  $\partial U/\partial y$  has its maximum at the position of maximum outflow due to the S-shaped wall-normal velocity profile in U (see e.g. Angele & Muhammad-Klingmann 2005). Thus, this gives the maximum production at the position of outflow and at the centre of the vortex, corresponding to  $-\langle uv\rangle\partial U/\partial y$  and  $-\langle uw\rangle\partial U/\partial z$ , respectively.

Finally, it is striking how well all the turbulence quantities in figure 19 scale with the VG height, h. Note that here all three VG heights have been plotted. The above discussed undershoot appears around  $(x - x_{VG})/h = 42$ ,

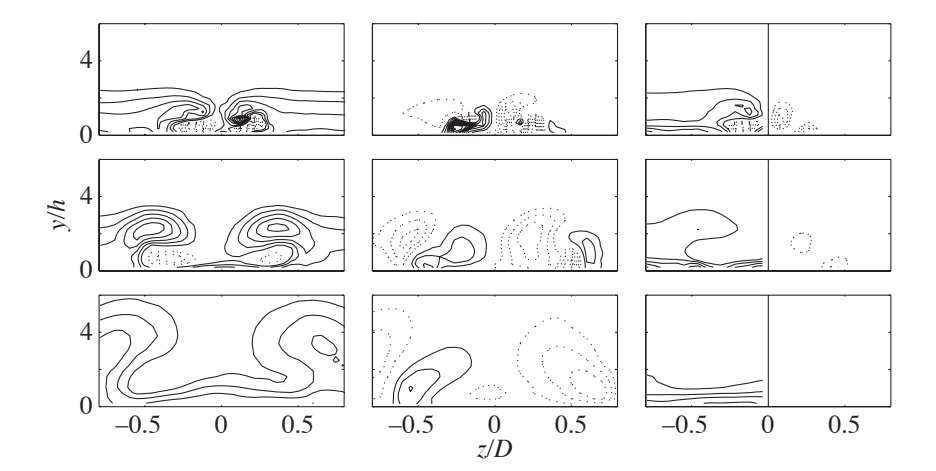


FIGURE 20. Contours of the two velocity co-variances with the streamwise component and the mean streamwise velocity gradients in the cross plane for the VG<sub>10</sub> configuration. From left to right,  $-\langle uv \rangle/U_{\infty}^2$ ,  $-\langle uw \rangle/U_{\infty}^2$  and  $(\partial U/\partial y, \partial U/\partial z) \cdot \tilde{\delta}_{99}/U_{\infty}$  = (left, right). From top to bottom the rows correspond to  $(x-x_{VG})/h=6$ , 42, and 167, respectively. The contour levels are  $(-2.4:0.3:2.7)\times 10^{-3}$  and (-1.25:0.25:-0.25;0.25:0.25:1.25) for the co-variances and the gradients, respectively. Note that for the former levels solid and dotted lines correspond to negative and positive co-variances, respectively. The opposite holds for the latter levels of the gradients.  $\tilde{\delta}_{99}$  is the spanwise averaged boundary layer thickness.

independent of the studied turbulence quantity and despite the factor of "three" in VG height difference between the lowest and the highest VGs.

# 4. The flow field downstream of yawed VGs

In many practical applications, especially ground vehicles, the VGs operate in yaw most of the time. Therefore it is of interest to study vortex generation and decay under such non-ideal conditions. Here, the  $VG_{10}$  case was chosen in both pair and array configurations (cf. table 3) for the yaw study. Yawing an array can be done in at least two different ways – either by yawing the whole array as one unit or by yawing the individual VG pairs (see the squared insert in figure 2). In this fundamental experiment the VG pairs are yawed individually in order to have the same boundary layer thickness at all blades and thus produce the same circulation for all VGs. The tested yaw angles were  $0^{\circ}$ ,  $5^{\circ}$ ,  $10^{\circ}$ ,  $15^{\circ}$  and  $20^{\circ}$ . They were chosen to be relevant for flow control on

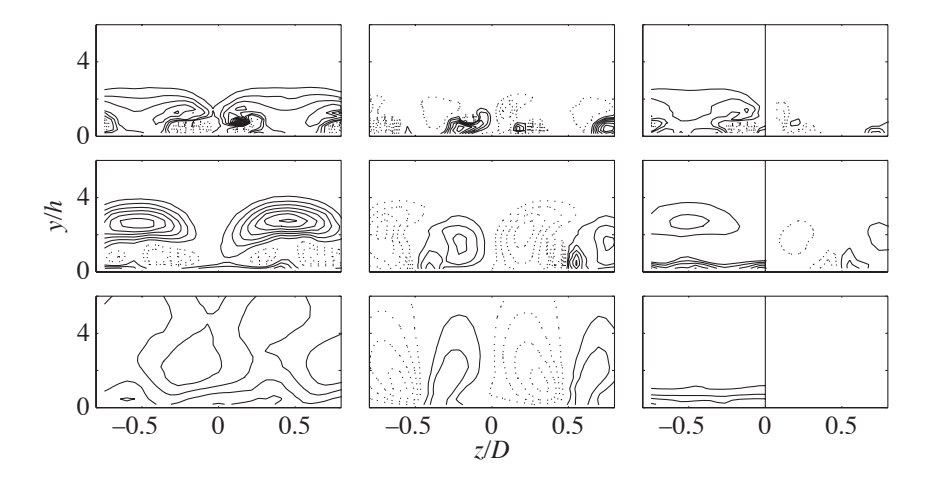


FIGURE 21. Same as in figure 20 but for the  $VG_{10}^a$  configuration. The contour levels are  $(-2.1:0.3:2.7)\times 10^{-3}$  and (-1.25:0.25:-0.25;0.25:0.25:1.25) for the co-variances and the gradients, respectively.

ground vehicles, such as trucks. Since the blade angle  $\alpha$  is  $\pm 15^{\circ}$  the "positive" blade will be yawed to 15, 20, 25, 30 and 35° and the "negative" blade to  $-15^{\circ}$ ,  $-10^{\circ}$ ,  $-5^{\circ}$ , 0° and 5°, implying that the negative blade will be parallel to the base flow in one configuration.

The purpose of introducing VGs in a flow is to increase the momentum near the wall, and in figure 22 the effect of changing the yaw angle is illustrated. Here the original ZPG boundary layer, without any vortices, is compared to the boundary layer modified by the the vortices from an array of VGs at 0°, 10° and 20° yaw. In the upper part of the boundary layer  $(y = \delta_{95})$ , unless too close the VGs, the VGs slow down the fluid and make the boundary layer thicker. This is more prominent in the downstream planes. Closer to the wall  $(y = \delta_{80})$ the vortices produce the desired velocity increase compared to the undisturbed ZPG case. The size of the area between the dotted and the solid black lines gives a visual indication of the momentum increase caused by the vortices. This area is almost constant for each x position, i.e. independent of the yaw angle, except for the first plane. This means that the momentum transfer to the lower part of the boundary layer neither decreases nor increases with yaw. Hence a flow control system based on the tested type of VGs will remain stable. A frequently used measure of the base flow modulation is the shape factor, which here has been calculated in order to demonstrate the overall effect of VGs in an array. Due to lack of X-probe data points near the wall, especially close to the array at the location of strong downwash at which the boundary layer

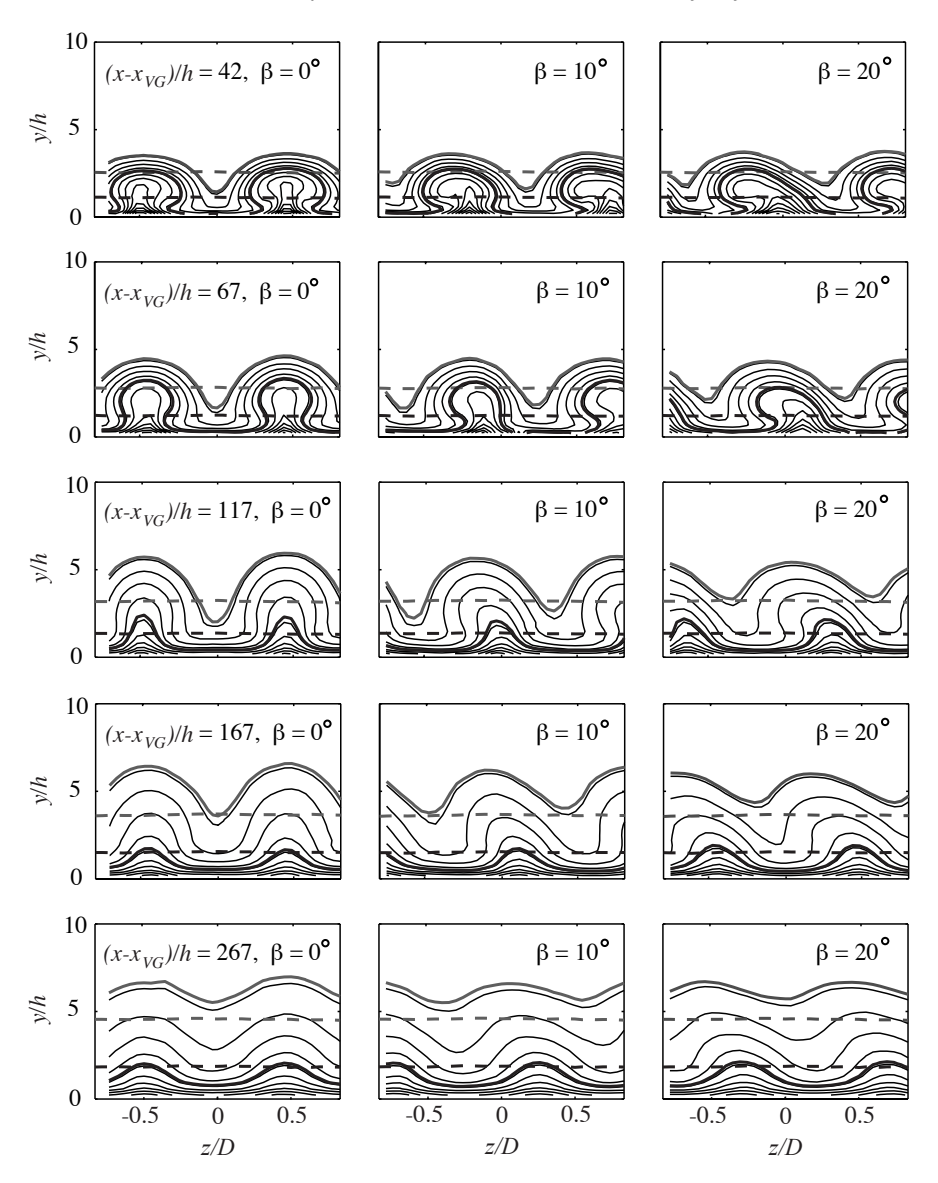


FIGURE 22. Contours of streamwise velocity at different x-positions downstream of the VG $_{10}^a$  case at 0, 10 and 20° yaw. The dotted grey and black lines corresponds to  $y = \delta_{95}$  and  $y = \delta_{80}$  respectively, in the vortex free base flow. The bold solid grey and black lines indicate the same y-positions for the shown VG cases.

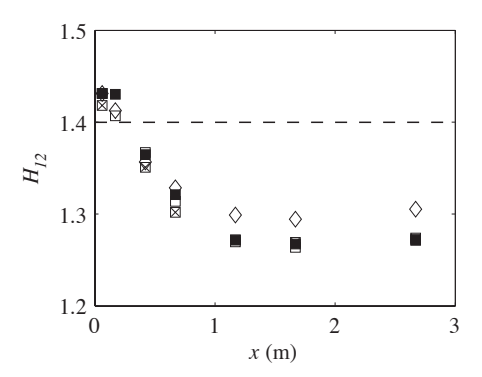


FIGURE 23. Shows the spanwise averaged shape factor for different yaw angles. ( $\square$ ,  $\boxtimes$ ,  $\blacksquare$ ) correspond to  $\beta = (0, 10, 20)$  degrees for the VG<sub>10</sub><sup>a</sup> case, respectively. ( $\Diamond$ ) correspond to VG<sub>6</sub><sup>a</sup> at zero yaw. The dashed line represent the ZPG base flow without VGs (cf. table 1).

is relatively thin, the calculation of the displacement thickness gives erroneous results. To compensate for the poorly resolved near-wall velocity profiles three additional points have consistently been added to approximate the profile in this region. Apart from the point corresponding to the no-slip condition, the additional points are  $y^+ = 5$  and 50, using the law of the wall and the log law, respectively, although the spanwise variation of  $u_{\tau}$  due to the vortices cannot be taken into account. Here it should be noted that it is not the local absolute values of  $H_{12}$  which are in focus; instead it is the spanwise-averaged values compared between the different configurations. In figure 23 the streamwise distribution of the spanwise-averaged shape factor is plotted for different yaw angles for the configuration VG<sub>10</sub><sup>a</sup>. In addition, the natural setting ( $\beta = 0$ ) for  $VG_6^a$  is also compared. It is seen that close to the VG array the shape factor is close to 1.4, i.e. hardly changed compared to the ZPG case without VGs, but decreases to a minimum value below 1.3 around 1.5 m behind the array, where it starts to recover. A similar evolution of the shape factor was reported by Fransson et al. (2005) in a laminar boundary layer. Here, the interesting result is that in an averaged perspective the yaw does not affec the shape factor or the change of VG size (only moderately) as shown in figure 23.

When a VG pair is yawed the absolute angle of attack of one blade increases, while the angle of attack of the other blade decreases. Thus one of the vortices in the counter-rotating pair becomes stronger, and the other gets weaker. Due to the shear flow and possible blade separation it is not clear whether this is a linear process at both blades, and therefore it is difficult to predict the total circulation generated by the VG pair. This investigation shows that the total circulation, up to a yaw angle of 20°, is almost constant (see figure 24a). The

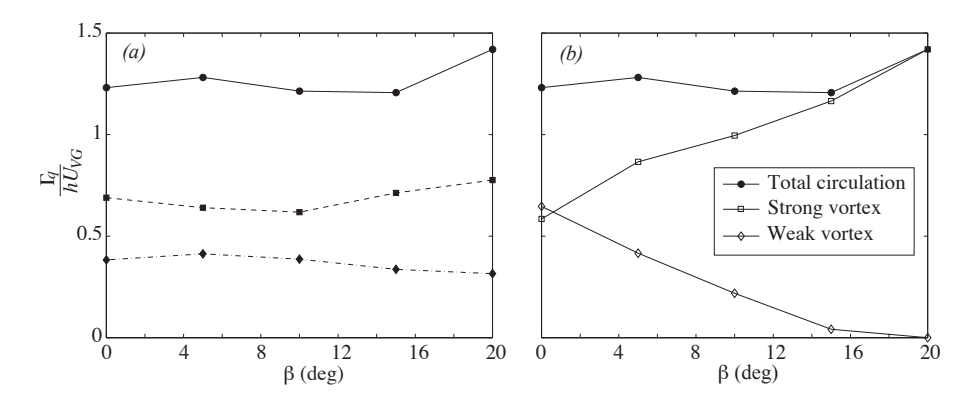


FIGURE 24. (a) shows the total circulation, i.e. the contribution from both the vortices, in the  $VG_{10}^p$  case versus the yaw angle at  $(x-x_{VG})/h = 6$ , 41, 116 with  $(\circ, \Box, \diamondsuit)$ , respectively. (b) shows the individual contribution from the two vortices for the  $VG_{10}^p$  case at  $(x-x_{VG})/h = 6$ .

circulation decay (seen vertically in the figure) also seems to be independent of yaw.

In figure 24(b) the effect of yaw on the individual vortices in a VG pair is shown at  $(x-x_{VG})/h=6$ . At 0° the two vortices should be of equal strength. The difference in the figure is due to imperfect positioning and manufacturing of the VG and to some degree also due to measurement error. When the yaw angle increases the circulation of both vortices changes linearly and according to the figure the blade that is parallel to the flow ( $\beta=15^{\circ}$ ) still produces a vortex. The reason for this behaviour could be that the strong vortex deflects the flow to reach the parallel blade at some angle or that this is caused by vorticity induced by the larger vortex. As shown by Wendt (2001) the circulation generated by a VG blade keeps increasing even after the blade stalls. This is probably what we observe here, since at 20° of yaw, i.e. an angle of attack of 35° of the strong vortex, the flow has most likely separated from the low pressure side of the blade.

Furthermore, the vortex centre paths are changed at yaw, which could be observed already in figure 22. This is due to the asymmetry caused by the fact that the two vortices of a pair are of different strength. In the 0° yaw case there is no net side force, but as soon as there is a difference in circulation the mirror images will induce a velocity that modifies the vortex paths. The paths are deflected in the direction of the strong vortex, and in figure 25 the vortex centre paths for different yaw angles are shown. When one of the vortices from the VG pair disappears, there is no longer a pair or an array of counter-rotating vortices. In the case of a VG pair the result is a single longitudinal vortex.

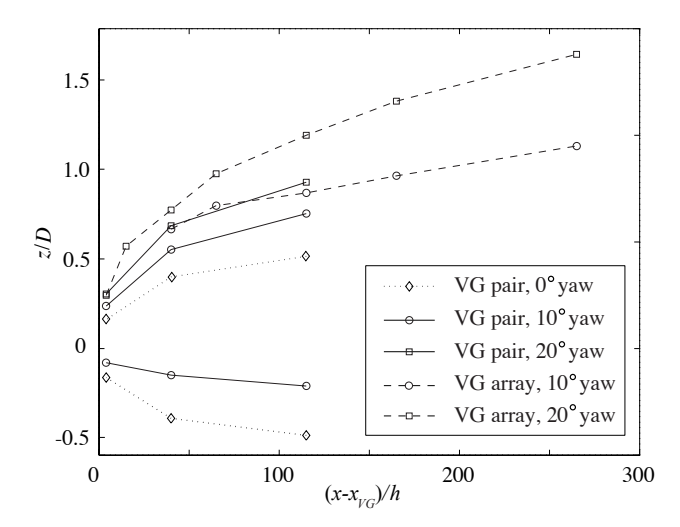


FIGURE 25. Vortex centre paths of  $VG_{10}$  pairs and arrays at  $0^{\circ}$ ,  $10^{\circ}$  and  $20^{\circ}$  yaw.

An array of VG pairs at yaw will produce a system of co-rotating vortices. Since the induced velocities of all the mirror images of the array work in the same direction the deflection angle is larger for an array compared to a pair at the same yaw angle. The vortex centre path of a VG pair at  $20^{\circ}$  yaw is approximately the same as that of a vortex generated in an array at  $10^{\circ}$  yaw. For the VG pair it was only possible to track the paths of the vortices up to  $(x - x_{VG})/h = 116$ ; beyond this position they were deflected out of the measurement plane due to the limited spanwise range of the traversing system. In case of the array it was possible to combine the vortex paths that were going out of the plane with the ones coming in from the other side.

## 5. A pseudo-viscous vortex model

In the course of this paper potential flow theory has been used to explain the streamwise evolution of longitudinal vortices. Jones (1957) calculated the paths of counter-rotating vortices from a system of VGs using potential flow theory and Pearcy (1961) proposed design criteria of VGs based on these calculations. Even though the assumption that the effect of viscosity can be neglected, implying that there is no wall-normal shear due to the slip condition at the wall and consequently that the vortices do not decay in strength as they move downstream, the agreement with experiments is remarkably good in the near region of the VG array. In this experiment measurements have been performed as far downstream as 450h of the VG array, and it is clear that the assumptions become questionable. However, here we have extended the analysis by Jones

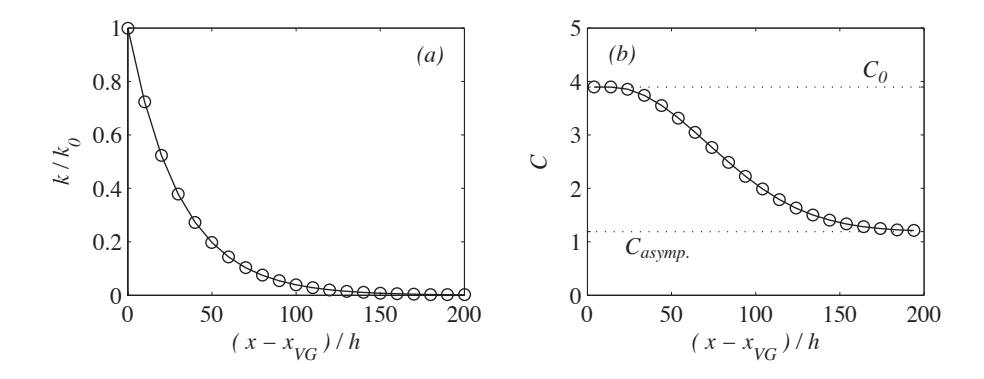


FIGURE 26. Model functions for (a) the vortex strength decay, and (b) the variable C in expression 4.

to also include vortex strength decay and a streamwise asymptotic z/D limit of the vortex centre based on experimental observations. This improved model seems to capture the effects of the flow physics in order to describe the vortex path also in the far region and, thus, gives a satisfactory agreement with the experimental results throughout the measurement region.

Jones (1957) showed that the projected vortex path in the plane normal to the stream is given by

$$\operatorname{cosech}^2 \eta + \operatorname{cosec}^2 \xi = C , \qquad (4)$$

where  $\xi = 2\pi z/D$ ,  $\eta = 2\pi y/D$ , and C is a constant determined from the coordinates of the VG pair tips  $(\xi_1, \eta_1)$ . From simple geometry analysis of the present VGs these coordinates are  $(\xi_1, \eta_1) = (\pi[d/D + l/D \tan \alpha], 2\pi h/D)$  giving  $C = C_0 = 3.89$  (cf. table 2). Moreover, the slopes of the paths projected in the x-z and x-y planes were also deduced by Jones and are given by

$$\frac{\mathrm{d}\xi}{\mathrm{d}\theta} = \frac{k \tan^2 \xi}{\sinh 2\eta \, \left(\tan^2 \xi + \tanh^2 \eta\right)} \tag{5}$$

and

$$\frac{\mathrm{d}\eta}{\mathrm{d}\theta} = \frac{k \tanh^2 \eta}{\sin 2\xi \left(\tan^2 \xi + \tanh^2 \eta\right)} , \qquad (6)$$

respectively, where  $\theta = 2\pi x/D$  and  $k = \{k_0 = \Gamma_0/(D \cdot U_h)\}$  = constant is the dimensionless vortex strength at the VG tips. These equations can be integrated stepwise after substituting for  $\eta$  or  $\xi$  from (4). For continuously increasing  $\xi$  and  $\eta$ , once one of the two integrals (from (5) or 6) has been calculated, the path projected in the missing plane is known, indirectly, through

(4). Worth mentioning here is since the applied VGs are "self-similar" there is no difference between the array configurations and thus their vortex centers follow the same paths.

Jones (1957) estimated the magnitude of k by a form of "lifting-line-theory" and hence k becomes solely a function of the incidence angle and configuration of the VGs (i.e. chord length, tip locations ( $\xi_1$ ,  $\eta_1$ ) and the lift slope in two-dimensional flow). However, the experiments (figure 16) show that the vortex strength decays exponentially with x, i.e.  $k = k(\theta)$ , and is not a constant. Thus, in the extended model we let k vary as  $\exp\{-\sigma \times 10^{-2}(x-x_{VG})/h\}$  with  $\sigma = 3.24$ , as shown in figure 26(a), where  $k_0$  is estimated from the experimental data to be 0.19 in the limit when x goes to zero. Here, the exponent has been tuned to fit the data, and a comparison with the measured vortex strength decay (figure 16) reveals that a stronger decay is needed for the model to work well in the far region. However, the choice of the exponential constant  $\sigma$  can be seen as a calibration parameter.

According to (4) the cross-flow vortex path is independent of k and for increasing  $\eta$  the vortex core asymptotes to a constant  $\xi$  value, which is already set by the initial VG configuration since  $C=C_0=$  constant. However, the experimental data show that the position of vortex core levels off to a constant wall-normal distance at the same time as the cores from a VG pair (in the array) move towards each other. In order to capture this behaviour with the model one needs to allow C to vary with  $\theta$ . Now, we can make use of the previously discussed asymptotic core limits (see § 3.3), namely  $(\xi_{asymp}, \eta_{asymp}) = (1.57, 1.57)$ , which gives  $C_{asymp} = 1.19$ , and assume C to vary as  $\exp{\{\varphi(\theta - \theta_s)^2\}}$  between  $C_0$  and  $C_{asymp}$  (see figure 26(b)). Here,  $\theta_s$  and  $\varphi$  were set to 14 and  $1.5 \times 10^{-4}$ , respectively, and can be seen as another set of calibration parameters of the model.

Figure 27 compares Jones (1957) original model and the pseudo-viscous model with experimental data for the three projected planes. In (a) the near region, up to  $(x - x_{VG})/h = 45$ , for the x-z plane is shown. The dashed lines correspond to the smoke visualization results, which rather represent the position of maximum positive mean velocity of the wall-normal component and then the location of the vortex cores. It is seen that the dashed lines diverge from the measured data points in the downstream direction, which is an artefact of the vortex growth. However, already at  $(x - x_{VG})/h$  of about 30 the neighbouring vortices limit the growth in the spanwise direction. In figure 27(a) it is seen that both models work well in the near region of the VGs. However, since Jones's (1957) model does not allow for a variation in C the vortex path reaches its asymptotic spanwise equidistance around  $(x-x_{VG})/h =$ 30 and consequently fails to describe the core evolution beyond this location (see figure 27(c)). In figure 27(d) the x-y plane is shown. The dotted line corresponds to the slope  $d\eta/d\theta$  (6) in the limit when  $\eta$  goes to infinity. It is seen that Jones's (1957) model is unable to predict the correct behaviour beyond

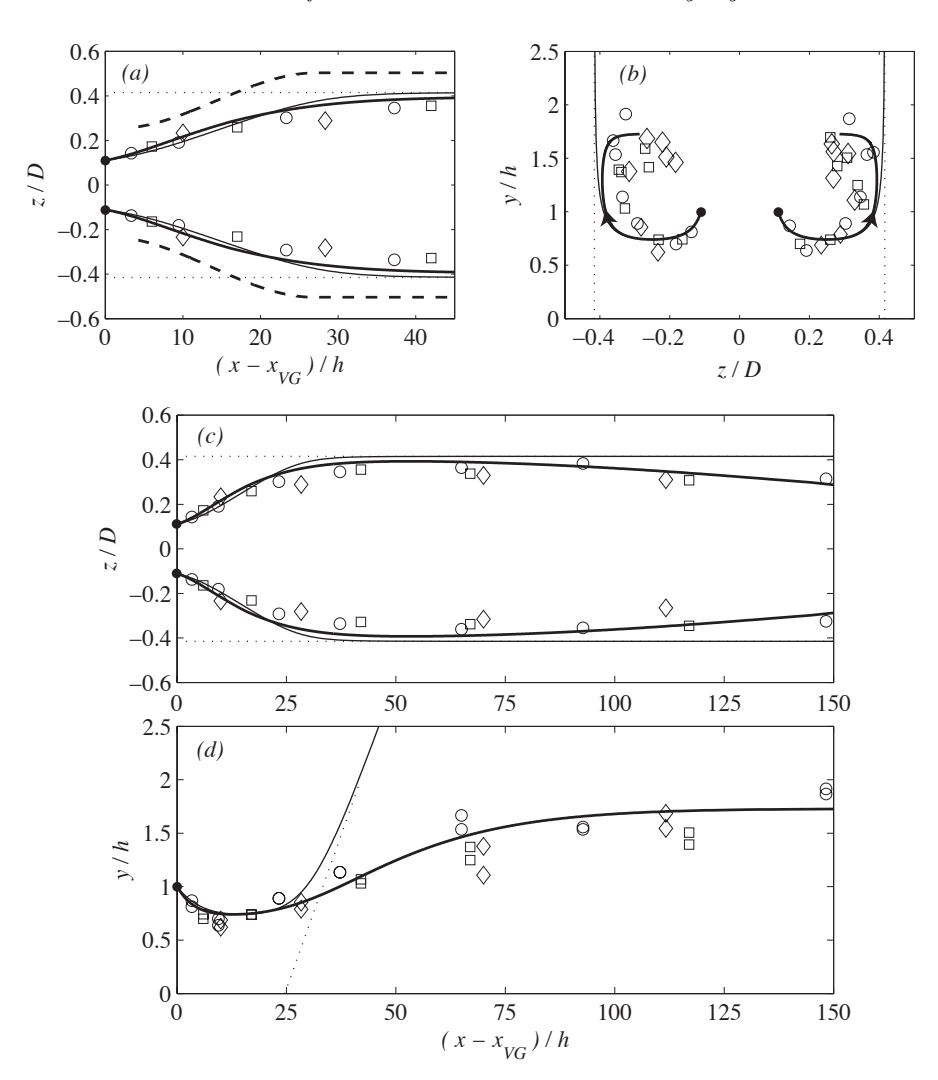


FIGURE 27. (a-d) show the vortex paths in the three projected planes. Bullets correspond to the positions of the VG tips, dotted lines indicate asymptotic limits for Jones original model , solid lines are theoretical curves where the bold lines correspond to the pseudo-viscous model and the thin lines to Jones model. The bold dashed lines in (a) correspond to the flow visualization results. The symbols  $\lozenge$ ,  $\square$  and  $\bigcirc$  denote  $h_{VG}=6$  mm, 10 mm and 18 mm.

 $(x-x_{VG})/h$  around 25, suggesting that the vortices, in quite an unphysical way, take off from the wall with a constant slope. However, the pseudo-viscous model works fine due to the vortex strength decay implementation. Finally, the peculiar curving-back motion of the vortex cores in the cross-flow plane is captured by the pseudo-viscous model as can be seen in figure 27(b).

## 6. Conclusions

In this study, in which both smoke visualization and hot-wire anemometry have been used, several new results of the evolution of longitudinal vortices are reported. Both vortex pairs and vortex arrays in the natural setting as well as yawed have been studied. A comparison between the smoke visualisation and hot-wire data affirm that, as intuitively expected, the trace of cumulative smoke particles in the laser sheet rather corresponds to the position of maximum positive vertical mean velocity than the location of the vortex core. Moreover, it is shown that for the present similarity parameter D/h = 8.33 there is no substantial difference between the pair and the array vortex core evolution up to  $(x - x_{VG})/h$  of about 35.

The vortex core paths in plan view as well as in the plane parallel to the stream scale with the VG height in the downstream direction and with D and hin the spanwise and wall-normal directions, respectively. In the array case the vortex paths are locked in the spanwise direction due to the neighbouring vortex pair, and consequently the proposed scaling works better in the far region for this configuration compared to the VG pair case. In this paper an asymptotic limit hypothesis of the vortex array path is stated and is shown to hold reasonable well. The limiting values are  $(y/h, z/D) = (2.08, \pm 0.25)$ , which the experimental data seem to approach. This result is contradictory to the inviscid flow analysis put forward by Jones (1957). Furthermore a peculiar hooklike motion, not previously reported, of the vortex core in the cross-sectional plane has been found in the array case as well as in the VG pair case. This motion is explained by the vortex growth and the limiting space inside the boundary layer due to neighbouring vortices. It is here shown, in the VG pair case, that strong vortices are able to induce vorticity which is rolled up into a secondary vortex and hence affect the primary vortex path. These flanking secondary vortices, naturally present in the VG array configuration, are responsible for the hooklike motion in the VG pair case, which otherwise would be absent. Furthermore, it has been shown that in both the pair and the array configuration the circulation decays exponentially with about the same rate, and the circulation scales with the VG height and corresponding local velocity at the position of the VG tip.

A striking result regarding the turbulence quantities is how well they scale with the VG height in the streamwise direction (cf.  $\S$  3.5).

The results of the yawed configurations are that in an averaged perspective there is hardly any effect compared with the natural setting. We have

shown that the spanwise-averaged shape factor is unaffected by yaw as well as the spanwise-averaged circulation. The stronger vortex in a yaw configuration compensates for the weaker contribution of the coupled vortex, thus rendering out the averaged effect. A notable difference between the natural setting and the yawed lies in the vortex core paths, which becomes important if a successive array or pair is thought of being implemented for a more persistent streamwise modulation of the base flow. It has been shown that the asymmetry affects the array configuration more than the pair case by comparing the  $10^{\circ}$  array yaw with the  $20^{\circ}$  single pair yaw, which show a similar streamwise evolution. Furthermore, as soon as the symmetry is broken due to yaw the asymptotic limit hypothesis ceases to be valid, since the paths are continuously deflected in the spanwise direction in favour for the stronger vortex. The weaker vortex with less circulation is not lifted up as strongly as its coupled vortex, and consequently the weaker vortex core stays closer to the wall compared to the stronger vortex.

In order to capture the evolution of vortex core paths in the far region behind an array of counter-rotating vortices it has been shown through a pseudoviscous vortex model that circulation decay and streamwise asymptotic limits have to be taken into account. These two viscous effects seem to contain the necessary physics for a model to perform well also in the far field. Based on a rather simple inviscid analysis by Jones (1957) an extended version is here proposed in which the two viscous effects just mentioned have been incorporated. Comparing the pseudo-viscous vortex model with the experimental data gives a satisfactory agreement throughout the measured region down to 400h. Involved in the model are three calibration/tuning parameters. One is the exponential constant  $\sigma$  giving the circulation decay, and the other two are connected to the model function  $C(\theta)$  appearing as a constant in the inviscid analysis (cf. (4)). Experimental data analysis of VG arrays has shown that the vortex core evolution scales with the VG height (h) and the individual VG pair spacing (D) in the streamwise and spanwise directions, respectively. Furthermore, the wall-normal position also scales with the VG height. Since the starting point for the pseudo-viscous vortex model is a purely inviscid model, i.e. boundary layer independent, the newly developed pseudo-viscous model also does not depend on the boundary layer parameters. In addition, since the analysis shows that the circulation of the VGs scale with the VG height and the corresponding velocity at that height, we believe that the initial vortex strength generated at the VG tip would scale equally good with the VG blade angle ( $\alpha$ ). The vortex path in both the x-z and x-y plane would in turn be well predicted by the pseudo-viscous vortex model due to the locking effect in the spanwise direction, which is created by the neighbouring VGs. No other parameter is likely to have any significant effect on the streamwise vortex core evolution meaning that the model is robust to geometry changes.

# Acknowledgments

Ola Lögdberg acknowledges Scania CV for the opportunity to carry out his doctoral work at KTH Mechanics within the Linné Flow Centre.

## References

- Angele, K. P. & Muhammad-Klingmann, B. 2005 The effect of streamwise vortices on the turbulence structure of a separating boundary layer. *Eur. J. Mech.*B **24**, 539–554.
- Blackwelder, R. F. & Eckelmann, H. 1979 Streamwise vortices associated with the bursting phenomenon. J. Fluid Mech. 94, 577–594.
- Cutler, A. D. & Bradshaw, P. 1991 A crossed hot-wire technique for complex turbulent flows. *Exp. Fluids* **12**, 17–22.
- Fransson, J. H. M., Brandt, L., Talamelli, A. & Cossu, C. 2005 Experimental study of the stabilization of Tollmien–Schlichting waves by finite amplitude streaks. *Phys. Fluids* 17, 054110.
- Fransson, J. H. M., Talamelli, A., Brandt, L. & Cossu, C. 2006 Delaying transition to turbulence by a passive mechanism. *Phys. Rev. Lett.* **96**, 064501.
- Godard, G. & Stanislas, M. 2006 Control of a decelerating boundary layer. Part 1: Optimization of passive vortex generators. *Aero. Sci. Technol.* **10**, 181–191.
- HUNT, J. C. R., WRAY, A. & MOIN, P. 1988 Eddies, stream, and convergence zones in turbulent flows. In *Center for Turbulence Research Report CTR-S88*, p. 193.
- JEONG, J. & HUSSAIN, F. 1995 On the identification of a vortex. J. Fluid Mech. 285, 69–94.
- Johansson, A. V. & Alfredsson, P. H. 1982 On the structure of turbulent channel flow. J. Fluid Mech. 122, 295–314.
- Jones, J. P. 1957 The calculation of the paths of vortices from a system of vortex generators, and a comparison with experiment. *Tech Rep.* C. P. No. 361. Aeronautical Research Council.
- Lin, J. C. 2002 Review of research on low-profile vortex generators to control boundary-layer separation. *Prog. Aero. Sci.* **38**, 389–420.
- LINDGREN, B. & JOHANSSON, A. V. 2002 Evaluation of the flow quality in the MTL wind-tunnel. *Tech. Rep.* 2002:13. Department of Mechanics, KTH, Stockholm.
- LÖGDBERG, O. 2006 Vortex generators and turbulent boundary layer separation control. Licentiate thesis, Department of Mechanics, KTH, Stockholm.
- Mehta, R. D. & Bradshaw, P. 1988 Longitudinal vortices imbedded in turbulent

- boundary layers. Part 2. Vortex pair with 'common flow' upwards. J. Fluid Mech. 188, 529–546.
- ÖSTERLUND, J. M. 1999 Experimental studies of a zero pressure-gradient turbulent boundary layer flow. PhD thesis, Department of Mechanics, KTH, Stockholm.
- ÖSTERLUND, J. M., JOHANSSON, A. V., NAGIB, H. M. & HITES, MICHAEL H. 2000 A note on the overlap region in turbulent boundary layers. *Phys. Fluids* **12**, 1–4.
- Pauley, Wayne R. & Eaton, John K. 1988 Experimental study of the development of longitudinal vortex pairs embedded in a turbulent boundary layer. *AIAA J.* **26**, 816–823.
- Pearcy, H. H. 1961 Boundary Layer and Flow Control: Its Principle and Applications vol. 2 Pergamon
- Schubauer, G. B. & Spangenberg, W. G. 1960 Forced mixing in boundary layers. J. Fluid Mech. 8, 10–32.
- Shabaka, I. M. M. A., Mehta, R. D. & Bradshaw, P. 1985 Longitudinal vortices imbedded in turbulent boundary layers. Part 1. Single vortex. *J. Fluid Mech.* **155**, 37–57.
- SWEARINGEN, J. D. & BLACKWELDER, R. F. 1987 The growth and breakdown of streamwise vortices in the presence of a wall. *J. Fluid Mech.* **182**, 255–290.
- Taylor, H.D. 1947 The elimination of diffuser separation by vortex generators. Tech Rep. R-4012-3. United Aircraft Corporation.
- Tsuji, Y., Fransson, J. H. M., Alfredsson, P. H. & Johansson, A. V. 2007 Pressure statistics and their scaling in high-Reynolds-number turbulent boundary layers. *J. Fluid Mech.* **585**, 1–40.
- Watmuff, J. H., Witt, H. T. & Joubert, P. N. 1985 Developing turbulent boundary layers with system rotation. *J. Fluid Mech.* **157**, 405–448.
- WENDT, B. J. 2001 Initial circulation and peak vorticity behavior of vortices shed from airfoil vortex generators. Tech Rep. NASA/CR 2001-211144. NASA.
- Wendt, B. J., Reichert, B. A. & Jeffry, D. F. 1995 The decay of longitudinal vortices shed from airfoil vortex generators. Tech Rep. 198356 AIAA-95-1797. NASA.
- Westphal, R. V., Eaton, J. K. & Pauley, W.R. 1985 Interaction between a vortex and a turbulent boundary layer in a streamwise pressure gradient. In 5th Symp. of Turbulent Shear Flows.
- Westphal, R. V. & Mehta, R. D. 1989 Interaction of an oscillating vortex with a turbulent boundary layer. *Exp. Fluids* 7, 405–411.
- Westphal, R.V., Pauley, W.R. & Eaton, J.K. 1987 Interaction between a vortex and a turbulent boundary layer. Part 1: Mean flow evolution and turbulence properties. Tech Rep. TM 88361. NASA.
- Yao, C-S, Lin, J. C. & Allan, B. G. 2002 Flow-field measurement of device-induced embedded streamwise vortex on a flat plate, AIAA 2002-3162. In 1st AIAA Flow Control Conf..

## Paper 3

# On the robustness of separation control by streamwise vortices

By O. Lögdberg<sup>1,2</sup>, K. Angele<sup>3</sup> and P. H. Alfredsson<sup>1</sup>

<sup>1</sup>Linné Flow Centre, KTH Mechanics, S-100 44 Stockholm, Sweden
<sup>2</sup>Scania CV AB, S-151 87 Södertalje, Sweden
<sup>3</sup>Vattenfall Research and Development AB, S-162 87 Stockholm, Sweden

The robustness of vane-type vortex generators (VGs) for flow control was studied in a separating turbulent boundary layer on a flat plate. VG arrays of different sizes and streamwise positions were positioned upstream of the separation bubble and their effect was studied with the help of particle image velocimetry (PIV). The size of the separated region was varied by changing the pressure gradient. It was found that the sensitivity of the control effect to changes in the size of the separation bubble is small within the applied range of pressure gradients. Furthermore, the importance of the relative position of the VGs with respect to the separated region is small.

#### 1. Introduction

Turbulent boundary layer separation is a flow phenomenon which often has a great negative effect on the performance in many technical applications. Therefore, it is of great practical importance and there is much to be gained if separation can be controlled.

Schubauer & Spangenberg (1960) investigated the relative performance of different mixing devices for separation control in a flat plate turbulent boundary layer subjected to a strong adverse pressure gradient (APG). Spanwise averaged mean velocity profiles were compared for different mixing devices and pressure gradients, and it was concluded that forced mixing has a similar effect as a lowering of the pressure gradient. Hence, forced mixing makes it possible to withstand a stronger pressure gradient, thereby delaying or even avoiding separation.

The most common technique to control separation in practice, on e.g. wings of commercial aircrafts, are vane-type VGs. Many different VG configurations were investigated by Pearcy (1961) and design criteria were given for both cases with co-rotating and counter-rotating vortices. The latter configuration is used in the present investigation. In figure 1 the main VG parameters are defined.

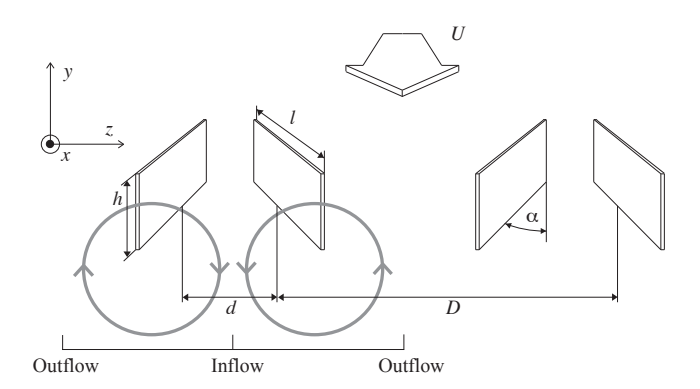


FIGURE 1. (a) VG geometry. All of the VG configurations produce counter-rotating vortices with a common inflow.

Pearcy (1961) predicted the vortex paths, based on inviscid theory for the interaction between different vortices and the surface (the image vortices). With a counter-rotating set-up, there is a transport of high momentum fluid from the free-stream towards the wall between two vortices from one VG, and there is a transport of low momentum fluid from the wall region up towards the free-stream between the two vortices from two different VGs. For this case the following was found: initially equidistant vortices approach each other in pairs with common outflow which results in a movement away from the surface. If the vortices are arranged to be initially non-equidistant the two vortices from one VG move away from each other and towards the wall. The movement towards the wall was found to give a high maximum efficiency for separation control. However, eventually the vortices will reach an equidistant state which will lead to a movement away from the wall. This scenario can be delayed by increasing the relative spanwise spacing (D/h) of the VGs, thus increasing the length over which the vortices are effective, at the expense of a slightly decreased maximum efficiency.

Pauley & Eaton (1988) carried out measurements in a zero pressure gradient (ZPG) turbulent boundary layer using a VG height h of approximately 15% of the local boundary layer thickness  $\delta$ . Focus was on the downstream development of the vortices in terms of streamwise vorticity  $\omega_x$  and circulation  $\Gamma$ . For a vortex pair with common outflow it was found that at the streamwise position where the decay in  $\Gamma$  was approximately 50%, the maximum  $\omega_x$  was reduced to 15-20%. The strength of the vortices increased linearly up to a VG vane angle of attack  $\alpha$  of 18°.

Model predictions for the flow field induced by triangular wedge like VGs were made by Smith (1994) to be used as a tool for VG design. The model predicted experimental data well and it was concluded that an increased efficiency

could be realized by more dense VG arrays and by longer VGs. The most beneficial spanwise spacing was found to be D/d=2.4, which is significantly lower than the D/d=4, suggested by Pearcy (1961).

More recent studies have focused on minimizing the drag induced by VGs, see e.g. the review by Lin (2002). A smaller VG results in lower form drag, making VGs with  $h < \delta$  attractive, where  $\delta$  is the boundary layer thickness. Lin *et al.* (1989) found that VGs with a relative height with respect to the boundary layer thickness  $h/\delta = 0.1$  were effective but the circulation decayed rapidly.

Angele & Grewe (2007) studied the behaviour of the streamwise vortices from a VG for the control of a separating APG boundary layer. It was found that the counter-rotating vortices from one VG moved away from each other in the spanwise direction and slightly outward in the wall-normal direction. The latter is contradictory to the conclusion by Pearcy (1961) and is an effect of the viscous diffusion of the growing boundary layer and the growing vortices. The results from wall shear-stress measurements showed that an approximately two-dimensional state was reached at  $(x - x_{VG})/h$ =30.

It was concluded by Angele & Muhammad-Klingmann (2005a) that the counter-rotating and initially non-equidistant streamwise vortices become and remain equidistant and confined within the boundary layer, contradictory to the prediction by inviscid theory. The boundary layer developed towards a two-dimensional state in the downstream direction. A critical value was found for the ability to eliminate the backflow, above which an increase in the circulation only had a minor effect.

Godard & Stanislas (2006) recently published a comprehensive optimisation study on co- and counter rotating VGs, with  $h < \delta$ , in an APG boundary layer. They conclude that triangular blades are better than rectangular blades, both in terms of increased vortex strength and in reduced drag. They also found that the counter-rotating set-up was twice as effective as the co-rotating in increasing the wall shear stress and that the optimum blade angle was  $\alpha = 18^{\circ}$ .

Lögdberg et al. (2008) studied VG pairs and VG arrays in a ZPG wind tunnel experiment, and showed that the vortex core paths scale with h in the streamwise direction and with D in the spanwise directions. Furthermore the experimental data indicates that the vortex paths asymptote to a prescribed location in the cross-plane. This observation contradicts previously reported numerical results based on inviscid theory. An account for the important viscous effects is taken in a pseudo-viscous vortex model which is able to capture the streamwise core evolution throughout the measurement region down to  $(x - x_{VG})/h = 450$ .

### 1.1. Summary and present work

The present study is a continuation of Angele & Muhammad-Klingmann (2005a) and Lögdberg et al. (2008) and aims at investigating the robustness of VGs for separation control. The question is how sensitive the control effect is to changes in the size and the location of the separation bubble relative to the VGs, something which is motivated by the changing nature of flows in real applications. More specifically we are investigating three different cases with different strength of the pressure gradient, generating three different sizes of separated regions. We also investigate the importance of the relative position of the VGs with respect to the separated region.

## 2. Experimental set-up

#### 2.1. Wind tunnel

The experiments were conducted in the BL<sup>1</sup> wind tunnel at KTH Mechanics. The test section is 4.0 m long and has a cross-sectional area of 0.75 m $\times$ 0.50 m (height×width). A temperature control system makes it possible to keep the temperature constant within  $\pm 0.03$  °C. For a detailed description of the wind tunnel the reader is referred to Lindgren & Johansson (2004). A schematic of the experimental set-up is shown in figure 2. A vertical flat test plate made of Plexiglas spans the whole height and length of the test section and is mounted with its surface 0.30 m from the back side wall of the test section. The coordinate system origin is located at the centreline at the plate leading edge, with x in the streamwise direction, y in the wall-normal direction and z in the spanwise direction. At the leading edge the boundary layer is tripped in order to ensure a spanwise homogenous transition to turbulence. At the inlet the test section width is 0.5 m, but at x = 1.25 m the test section is diverged, by the back side curved wall, in order to decelerate the flow and thus induce an APG. Suction is applied on the curved wall to prevent the boundary layer from separating there. Instead the separation bubble develops on the flat test plate. By changing the suction rate the strength of the APG can be varied. Three different suction rates were used to create APG cases I, II and III. For APG case I the suction rate was set to 6–7% of the flow over the flat plate at the inlet of the test section. In case II the suction rate was 12.5–13% and in case III it was approximately 17%. APG case I was thoroughly investigated by Angele & Muhammad-Klingmann (2005a, 2006) and case II and III are experiments performed in the present study. For definitions of case I, II and III see section 3.1a.

 $<sup>^1\</sup>mathrm{For}$  "Boundary Layer" or "Björn Lindgren", after the designer of the tunnel.

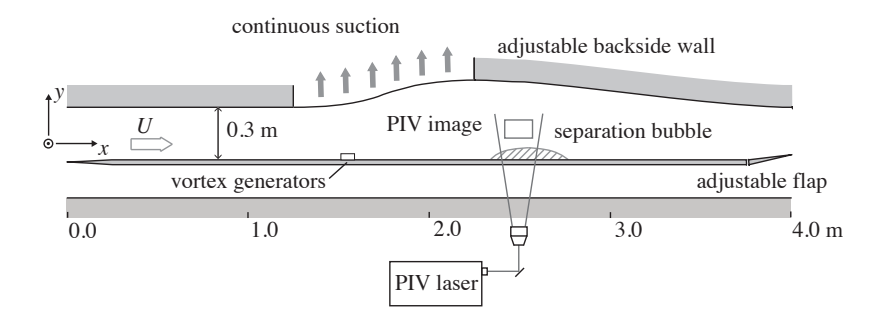


FIGURE 2. Schematic of the test section seen from above. The x direction is aligned with the test plate and the y direction is perpendicular to it.

#### 2.2. Measurement technique

The static pressure was measured on the test plate centreline in order to quantify the APG cases. All flow field measurements were performed with PIV in either x-y planes or x-z planes.

The PIV-system uses a 400 mJ double cavity Nd:Yag laser operating at 15 Hz and a  $1018 \times 1008$  pixels CCD camera with 8 bit resolution. The air was seeded with smoke droplets generated by heating glycol injected in the pressure equalizer slit downstream of the test section. The droplets are large enough to render a particle image size larger than 2 pixels in all measurements. According to Raffel et al. (1997) this is enough to avoid peak-locking due to problems with the peak-fit algorithm. Furthermore, the ratio between the discretization velocity  $u_d$  and the  $u_{rms}$  is close to 2 in all measurements. According to Angele & Muhammad-Klingmann (2005b) this reduces errors due to peak-locking effects in mean- and rms-values to approximately 1%. The number of particles inside the interrogation areas is higher than five, as recommended by Keane & Adrian (1992), in all measured x-y planes.

Conventional post-processing validation procedures were used. No particles moving more than  $25\,\%$  of the interrogation area length were allowed in order to reduce loss-of-pairs and the resulting low-velocity bias. The ratio between the highest and the second highest peak in the correlation plane must be more than 1.2 if the vector should be accepted. Often the light in the PIV images are streaky due to fittings and bubbles in the Plexiglas, but the streaks are always in the wall-normal direction at x-y plane measurements. Thus it was always possible to measure velocity profiles with validation ratios of more than  $95\,\%$ .

The wall static pressure P was measured using a Furness pressure transducer. The pressure transducer has an accuracy of 0.025% of full scale (2000 Pa),

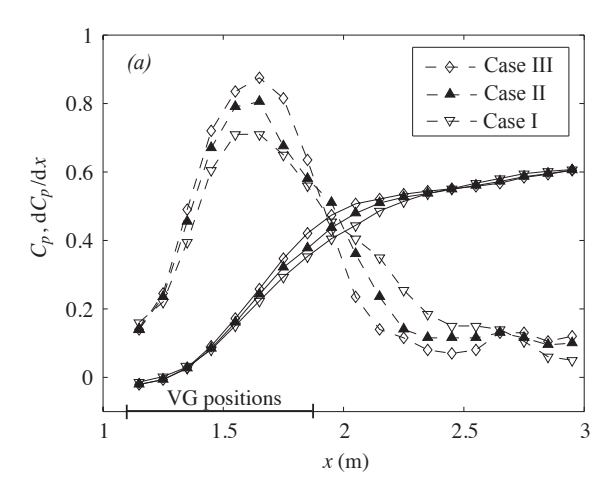


FIGURE 3. Pressure distribution  $C_p$  and its gradient in the streamwise direction  $dC_p/dx$ . The region where the VGs are mounted is indicated on the x-axis.

which in the present experiment produces a measurement accuracy of 1–3 %. In figure 3 the pressure coefficient

$$C_p = \frac{P - P_{ref}}{P_0 - P_{ref}} \tag{1}$$

for the wall static pressure and its gradient in the flow direction are plotted against the distance from the leading edge of the test plate.  $P_{ref}$  is taken on the wall at x=0.45 m and  $P_0$  is the total pressure at the same x-position.

## 2.3. The circulation generated by the VGs

In this experiment the separation control is performed by arrays of counterrotating vortices, where each VG pair produces a vortex pair with common flow downwards (c.f. figure 1). All arrays span the whole width of the test section, like in figure 4. The VG arrays applied here have the same dimensions as the ones previously used by Angele & Muhammad-Klingmann (2006), but are supplemented by one smaller set. Their geometries are described in table 1. The blade angle  $\alpha$  is 15° and the general design follows the criteria suggested by Pearcy (1961). There are four different sizes, which are geometrically self-similar, i.e. D/h, D/d and l/h are constant (see figure 1).

For a VG pair, Angele & Muhammad-Klingmann (2005a) found that the total generated circulation can be estimated as

$$\Gamma_e = 2khU_{VG},\tag{2}$$

Table 1. Physical dimensions of the VG sets. The first parameters are defined in figures 1 and 4, Z is the width of the test section and Z/D is the number of VG pairs in the array.

h  (mm)	d  (mm)	l  (mm)	D  (mm)	l/h	D/h	D/d	Z/D	
6	12.5	18	50	3	8.33	4	15	
10	21	30	83	3	8.33	4	9	
18	37.5	54	150	3	8.33	4	5	
30	62.5	90	250	3	8.33	4	3	

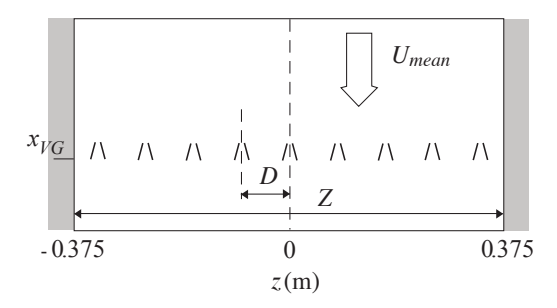


FIGURE 4. A top-view of the 10 mm VG array in the BL wind tunnel. All tested arrays are set up like this: the mid pair at z=0 and the centreline of the outermost pair at a distance D/2 from the wall. The streamwise position of the array is defined as the position of the blade trailing edge.

where  $U_{VG}$  is the mean velocity at the VG blade tip and k is a coefficient which is a function of the geometry of the VG. The estimation of  $\Gamma$  makes it possible to rank the circulation of different VG configurations without measuring the velocities in the y-z plane. For an array of VGs, it is better to estimate the circulation generated per unit width

$$\gamma_e = 2k \frac{hU_{VG}}{D}. (3)$$

For the VG array the number of VGs increases with decreasing blade height, but h/D is constant. However,  $\gamma_e$  increases with h since the blade reaches higher up in the boundary layer, where the velocity is higher. For the VG geometry described in table 1, eq. 2 becomes  $\gamma_e = 0.24kU_{VG}$ .

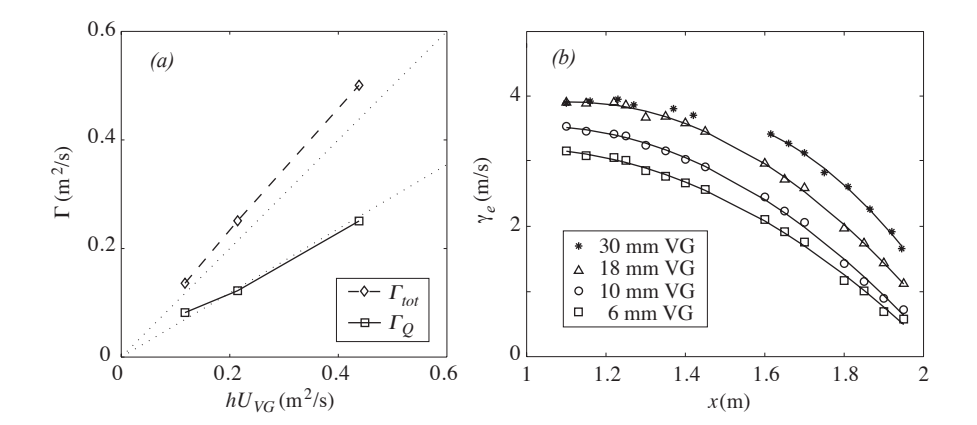


FIGURE 5. (a) Circulation generated by 6, 10 and 18 mm VGs calculated in two different ways from the ZPG data of Lögdberg et al. (2008). The two dotted lines show k=0.6 and k=1.0 in eq. 2. (b) Estimated generation of circulation per unit width depending on the position and size of the VG in APG case III for the arrays described in table 1.

In Lögdberg et al. (2008) the cross-plane velocities produced by VG arrays, identical to the ones applied here, were measured in a plane 6h downstream of the array. The circulation was calculated by integrating the streamwise vorticity  $\omega_x$  over an area. The total circulation  $\Gamma_{tot}$  is obtained by integrating  $\omega_x$  over  $\Delta z = D/2$  and to obtain  $\Gamma_Q$  an integration of  $\omega_x$  is made over the area inside a contour defined by a constant value of  $Q_x$ . Q is the second invariant of the velocity gradient tensor, and its streamwise component is calculated as

$$Q_x = -\frac{1}{2} \frac{\partial W}{\partial y} \frac{\partial V}{\partial z}.$$
 (4)

in the y-z plane.  $Q_x$  is useful since it is a measure of the local rotation, without contribution from pure shear. The contour of constant  $Q_x$  is chosen as  $Q_x = 0.05\,Q_{x,max}$ . This level is somewhat arbitrary, but empirical tests have shown that this value produces stable and consistent levels of circulation for a wide range of data. In figure 5(a) the circulation measured for h=6, 10 and 18 mm are compared to the corresponding circulation estimates from eq. 2. The dotted lines in figure 5(a) show k=0.6 and k=1.0. The value of k is less important and it is sufficient that the estimate works in a consistent way when comparing the relative strength of the vortices produced by different VG configurations. In the results presented hereafter k=0.6 is used, thus  $\gamma_e=0.144U_{VG}$ .

In the present study, the circulation generated by the VG array is varied by varying h and  $x_{VG}$ . Changing h directly affects eq. 2, but  $x_{VG}$  acts by changing  $U_{VG}$ . When the position of the VG array is moved downstream, the rapidly increasing boundary layer thickness  $\delta$  causes  $h/\delta$  to decrease and thereby reduces  $U_{VG}$ . The VG array was positioned at different locations at  $1.10 \text{m} < x_{VG} < 1.95 \text{m}$  in order to generate different levels of circulation. To be able to estimate  $\gamma_e$ , 15 wall-normal velocity profiles were measured in this region. Then  $\gamma_e$  was calculated for four different values of h at each measurement position, using eq. 2. The resulting  $\gamma_e$  for case III are presented in figure 5(b). The lines are least squares fits to the points<sup>2</sup>. Note that for the largest VGs,  $h > \delta$  for x < 1.5 m and thus  $\gamma_e$  no longer increases as  $x_{VG}$  is moved upstream.

#### 3. Results

In the following the experimental results are presented. First the uncontrolled flow cases are characterized. Then the effects of different VG array configurations are reported. The shape factor  $H_{12} = \delta_1/\delta_2$ , where  $\delta_1$  is the diplacement thickness and  $\delta_2$  is the momentum loss thickness, is consistently used to describe the boundary layer.

#### 3.1. The uncontrolled case

The uncontrolled APG cases are also discussed in Lögdberg et al. (2008). The free stream velocity in the wind tunnel  $U_{\infty}$  is 26.5±0.1 m/s at the inlet of the test section. The temperature was kept constant at 20 °C throughout all the measurements.

3.1a. The pressure distribution and the shape factor. The pressure gradient was set through a contoured wall and by changing the suction rate as described in section 2.1. Three pressure gradients are compared here. Data for case I are taken from Angele & Muhammad-Klingmann (2005a, 2006) and are reproduced here. Case II and III are new experiments. Case I is a weak separation bubble, case III is the largest possible separation bubble with the present suction fan and geometry and case II is in between the other two pressure gradients. Case II is the most thoroughly investigated configuration.

As shown in figure 3 the APG reaches its maximum between x=1.6 and 1.7 m. In this area the maximum  $\mathrm{d}C_p/\mathrm{d}x$  for the three APG cases are 0.70, 0.78 and 0.87 m<sup>-1</sup> respectively. The shape factor is approximately constant until x=1.7 m for all APG cases, as shown in figure 6. Then it increases rapidly and reaches a maximum at  $x\approx2.55$  m.

<sup>&</sup>lt;sup>2</sup>By extrapolating the curves to  $\gamma_e = 0$ , it is possible to obtain a fairly accurate estimate of the separation point.

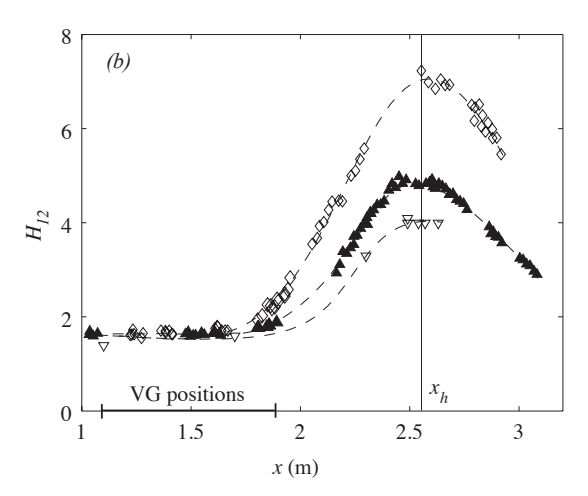


FIGURE 6. Streamwise evolution of  $H_{12}$ . Note that the lines are for visual aid only.

3.1b. The backflow coefficient. Here the separation bubble is defined as the region where backflow occurs more than 50 % of the time ( $\chi > 0.5$ ). The point of separation is defined as the position where the backflow coefficient on the wall<sup>3</sup> ( $\chi_w$ ) reaches 0.5. This parameter is difficult to measure directly with PIV, since the interrogation areas must be large enough to contain approximately 5 particles. In this experiment the data points closest to the wall are located at y = 1.5-3 mm, and since  $\chi$  is a strong function of y, the value of  $\chi$  measured at the point closest to the wall under-predicts  $\chi_w$ . Dengel & Fernholz (1990) used wall pulsed wires with the sensor wires only 0.03 mm above the wall to obtain an accurate value of  $\chi_w$ . According to their data,  $\chi$  is almost a linear function of y when  $\chi_w$  is larger than 0.4–0.5. Therefore,  $\chi_w$  was estimated from a linear fit to the seven data points closest to the wall, as shown in figure 7(a). The described procedure will still under-predict  $\chi_w$  for lower values of  $\chi_w$ . This will cause the estimated separation point to be slightly more downstream and the point of reattachment to be more upstream than their actual positions. In the separation bubble  $\chi_w$  is more accurate. In figure 7(b) the development of  $\chi_w$  through the separated region is shown for APG case II.

3.1c. Overview of the separated region. The set-up aims at a two-dimensional flow around the test section centreline (z=0) and the spanwise velocity profiles in figure 8 show an acceptable two-dimensionality even for the worst case (III).

An overview of the three investigated separation bubbles is given in table 2, where  $x_s$  and  $x_r$  are the separation and reattachment points, respectively,  $l_s$ 

<sup>&</sup>lt;sup>3</sup>On the wall it is the direction of  $\tau_w$  that defines  $\chi$ .

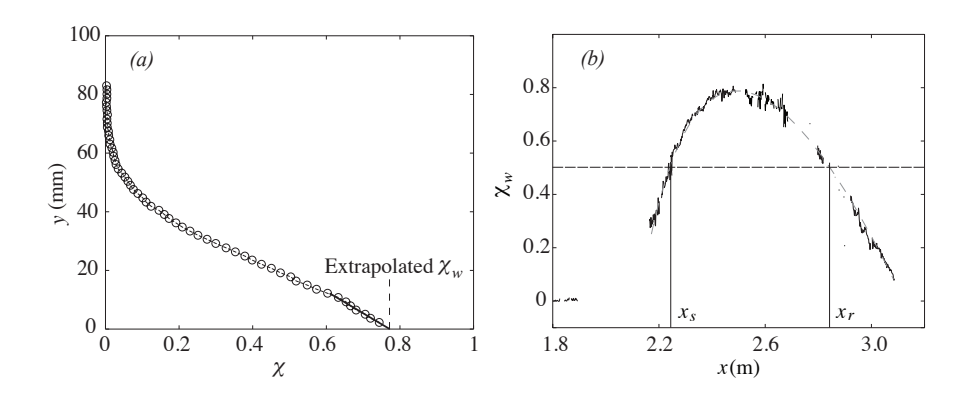


FIGURE 7. (a) The backflow coefficient at the wall for case II.  $\chi$  is extrapolated to the wall from the data points in the region  $y \approx 1.5$ –10 mm, to estimate  $\chi_w$ . (b) The downstream development of  $\chi_w$  for case II.

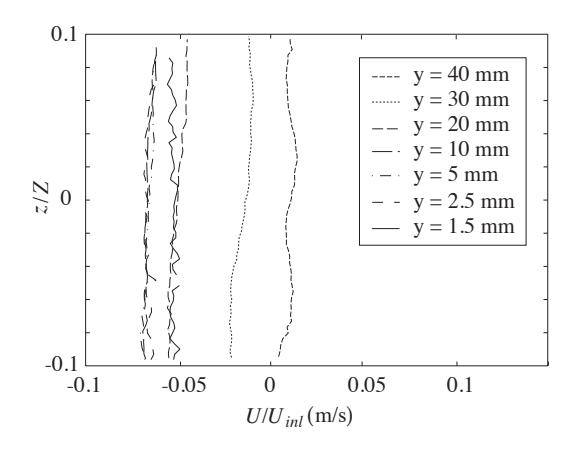


FIGURE 8. Mean velocity profiles at x = 2.55 m for case III.

is the length of the separated region and  $h_s$  its maximum height. Here  $x_r$  is defined in the same way as  $x_s$ , i.e.  $\chi_w = 0.5$ . When the pressure gradient increases,  $x_r$  is moving downstream approximately the same distance as  $x_s$  is moving upstream. Thus, the position of the separation bubble centre is nearly constant for all cases. Furthermore, the bubble aspect ratio AR, i.e. ratio of height to length, increases with increasing pressure gradient. Thus the separation bubble thickness increases both in absolute and relative terms with

Table 2. Separation bubble size. In case III the point of reattachment is approximated from visual inspection of tufts attached with tape on the test plate. Thus  $x_r$  and  $l_s$  are more uncertain for case III.

Case	$\mathrm{d}C_p/\mathrm{d}x\ (\mathrm{m}^{-1})$	$x_s$ (m)	$x_r$ (m)	$l_s$ (m)	$h_s \text{ (mm)}$	$H_{12,sep}$	AR
I	0.70	2.4	2.7	0.3	7	3.45	0.23
II	0.78	2.24	2.85	0.6	17	3.50	0.28
III	0.87	2.09	3.1	1.0	35	3.75	0.35

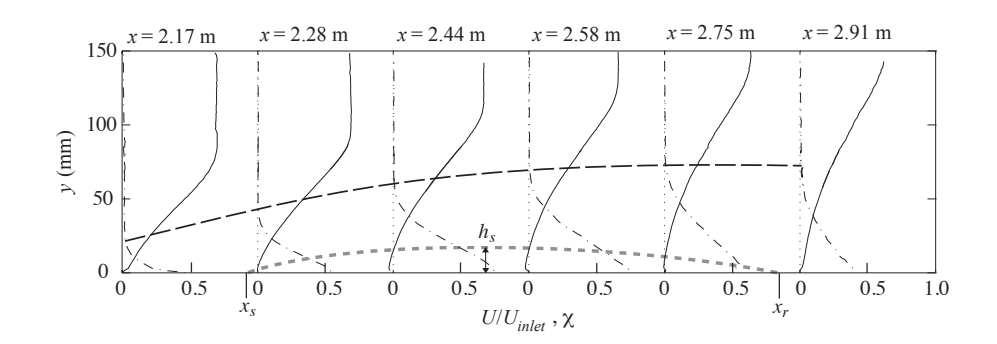


FIGURE 9. The separation bubble for the APG case II . The figure is not to scale and therefore the bubble appear to be thicker. The full lines show  $U/U_{inlet}$ , the dash-dotted lines show the backflow coefficient  $\chi$ . The extent of the separation bubble, defined as the region where  $\chi>0.5$ , is shown by the lower dashed line. The higher dashed line shows the region of  $\chi>0$ .

increasing APG. Also  $H_{12,sep}$ , which is  $H_{12}$  at  $x_s$  increases with increasing APG.

Case II is most thoroughly investigated and an overview of the flow around the separation bubble is shown in figure 9. In the figure the streamwise evolution of the mean velocity profile and the backflow coefficient are presented. A complete profile at each position was obtained from two measured x-y planes, which overlap slightly in the y-direction. As reported in table 2,  $x_s = 2.24$  m and  $x_r = 2.85$  m. Note that, due to the growth of the boundary layer, the y position where  $\chi > 0$  is moving further out from the wall even after the bubble has passed its maximum height. The first backflow events occur a short

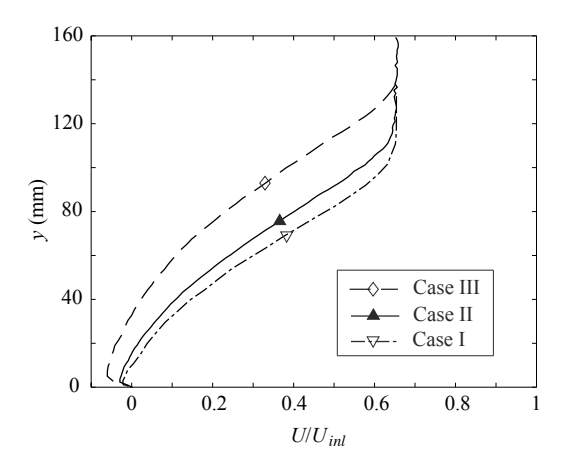


FIGURE 10. The mean velocity profiles at x=2.55 m in the uncontrolled APG cases.

distance upstream of the separation point, and from figure 7(b) the position can be estimated to be at  $x \approx 2.1$  m.

The mean velocity profiles for all three cases at x=2.55 m are compared in figure 10. In Lögdberg *et al.* (2008) it was shown that the mean velocity defect profiles of the three APG cases are self-similar in the region between  $x_s$  and the position of maximum backflow.

#### 3.2. The controlled case

As shown in 5(b), the rapidly growing boundary layer makes it possible to produce any vortex strength up to  $\gamma_e = 4.0$  m/s with only four different VG arrays. However, in relation to the measurement position, the vortices produced further upstream will evolve and decay over a larger distance compared to vortices produced at a position further downstream. This is discussed in section 3.2c.

3.2a. Measurement positions. In figure 6 it is shown that the maximum in  $H_{12}$  occurs at  $x_h \approx 2.55$  m for all APG cases. Furthermore, in Lögdberg et al. (2008) it was reported that  $H_{12}$  increases linearly with  $\chi_w$  and that their maxima coincides. Thus  $x_h$  is suitable as reference position when the control effect of different VG sets are compared. The spanwise position where the vortices produce an inflow is always at z/D=0 and the outflow position is at z/D=0.5. Since these are the extreme positions, velocity profiles are always measured at both z/D=0 and z/D=0.5. Detailed results from APG case I are thoroughly presented in Angele & Muhammad-Klingmann (2005a) and the focus of the present paper is on case II and case III.

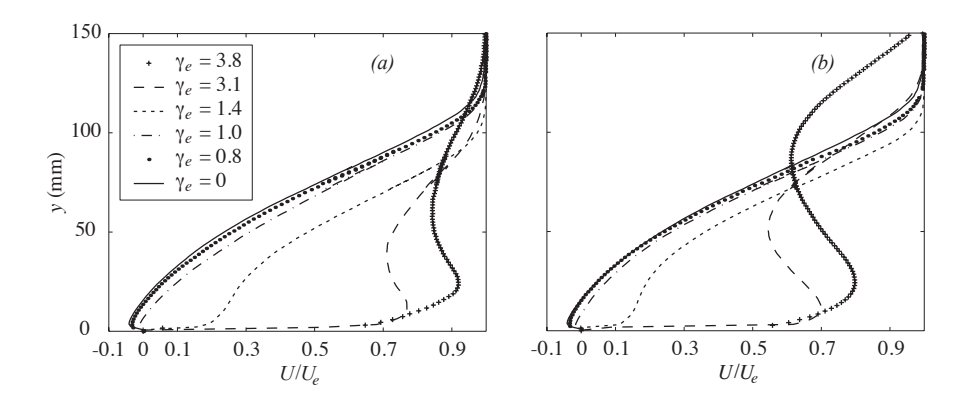


FIGURE 11. Mean velocity profiles at (a) the spanwise position of inflow and (b) the position of outflow.

Table 3.  $H_{12}$  and  $\chi_w$  of the profiles seen in figures 11 and 12.

$\gamma_e \ (\mathrm{m/s})$	$(x_h - x_{VG})/h$	I	$H_{12}$	2	$\chi_w$
		Inflow	Outflow	Inflow	Outflow
0	-	4.9	4.9	0.75	0.75
0.8	92	4.6	4.9	0.74	0.75
1.0	55	4.0	4.4	0.63	0.65
1.4	31	2.6	3.2	0.11	0.13
3.1	53	1.4	1.6	0.0	0.0
3.8	81	1.3	1.5	0.0	0.0

3.2b. Circulation and reverse flow elimination. When evaluating the control effect of the vortices it is useful to define a simple measure of merit. The measure used in this article is  $H_{12}$ . In separated flows  $H_{12}$  is a good indicator of the backflow. It has been shown by Dengel & Fernholz (1990) and Lögdberg et al. (2008) that  $H_{12}$  is proportional to  $\chi_w$  in the separated region. In this experiment  $H_{12}$  and  $\chi_w$  are nearly proportional also in the flow cases with VGs. It could be argued that  $\chi_w$  is more suitable for separation control purposes. The reason why  $H_{12}$  is preferred is that it is easier to calculate it accurately for  $\chi_w < 0.4 - 0.5$ .

The purpose of the VG arrays is to eliminate the mean reverse flow in the separated region. In figure 11 the streamwise mean velocity profiles U(y) at the position of inflow (z/D=0) and the position of outflow (z/D=0.5), are

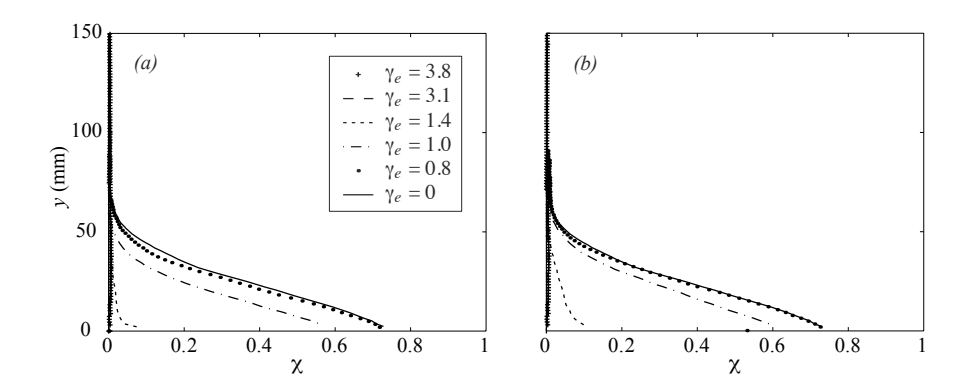


FIGURE 12. Backflow coefficient profiles at (a) the spanwise position of inflow and (b) the position of outflow.

shown for different VG configurations in case II. The uncontrolled case,  $\gamma_e=0$ , is shown for comparison. In table 3 the results are listed. At the position of inflow, more streamwise momentum is transported down through the boundary layer, and a larger effect of the VGs can be seen compared to the position of outflow. However, due to the spanwise movement of the vortices and the viscous diffusion, the difference has become quite small. The two VGs which produces the least circulation,  $\gamma_e=0.8$  and  $\gamma_e=1.0$ , have negligible influence on U, but when the circulation is increased to  $\gamma_e=1.4$  mean separation is prevented. The change in U is not large, but as shown in figure 12 the reverse flow is almost eliminated. At the positions of inflow and outflow  $\chi_w$  is only about 0.08 and 0.15 respectively. Thus, the backflow coefficient is correlated to the circulation in a nonlinear way. Since the drag of the VG array is expected to increase with  $\gamma_e$ , this is the most efficient VG configuration for preventing separation in this particular flow case.

Figure 13 summarises the separation control effectiveness of all examined VG configurations. Here the  $H_{12}$  values at  $x_h$  for case I, II and III are compared for different  $\gamma_e$ . In the separation bubbles of the uncontrolled cases,  $H_{12}$  is approximately 4, 5 and 7 in the respective cases. This can also be seen in figure 6. The dashed lines display the results at the spanwise position of outflow and the dotted line refers to the position of inflow. A fuller profile and hence a lower  $H_{12}$  is expected at the position of inflow, as can be seen when comparing figures 11 (a, b). This is shown in figure 13, where the two curves are separated by an average  $\Delta H_{12} \approx 0.3$ .

For the flow to stay attached  $H_{12}$  should be lower than  $H_{12,sep}$  in table 2 i.e.  $H_{12} \approx 3.5$ . The light grey area in figure 13 indicates the present range of  $H_{12,sep}$ . The value of  $\gamma_e$  at which the flow stays attached seems to be

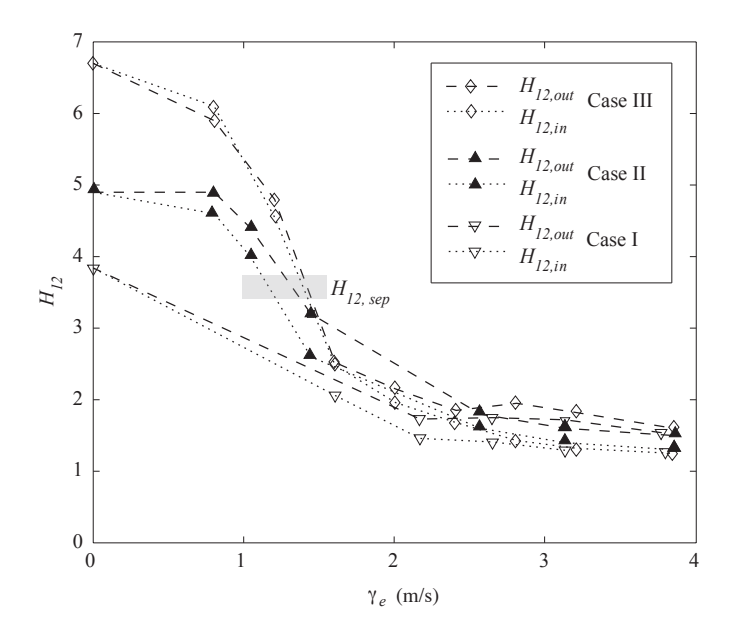


FIGURE 13. The shape factor  $H_{12}$  at the position of inflow and the position of outflow plotted against  $\gamma_e$  in case I, II and III. The measurements were made at the respective separation bubble's streamwise position of maximum bubble height.

fairly insensitive to the pressure gradient, even though the difference in size of the separated region is quite large in the uncontrolled cases. A  $\gamma_e$  of 1.3-1.5 m/s is sufficient for cases II and III. Case I has too few data points to allow any conclusions. The drop in  $H_{12}$  is sudden in both case II and III, and confirms the nonlinearity suggested above. When the circulation is further increased, the shape factor levels off to about  $H_{12}=1.3$  at the position of inflow and to  $H_{12}=1.5$  at the position of outflow. Thus the average  $H_{12}$  seems to asymptotically approach 1.4, similarly to a ZPG turbulent boundary layer. At  $\gamma_e > 1.5$  m/s the variation of  $H_{12}$  with  $\gamma_e$  is similar for all APG cases, and for  $\gamma_e > 2.5$  m/s the pressure gradient has no effect on  $H_{12}$ . This suggests that there exists a  $\gamma_e$ , within the present APG range, above which the pressure gradient no longer affects the flow.

3.2c. Streamwise position of the VGs. To design an efficient flow control system with VGs it is not only necessary to decide the circulation required to prevent separation, but also the position of the VGs with respect to the point of separation. So far, in the present study, it has not been taken into account

Table 4. Four VG configuration that produce  $\gamma_e = 3.1$ .

h  (mm)	$x_{VG}$ (m)	$(x_h - x_{VG})/h$	$\gamma_e \ (\mathrm{m/s})$
6	1.10	242	3.1
10	1.37	118	3.1
18	1.54	56	3.1
30	1.68	29	3.1

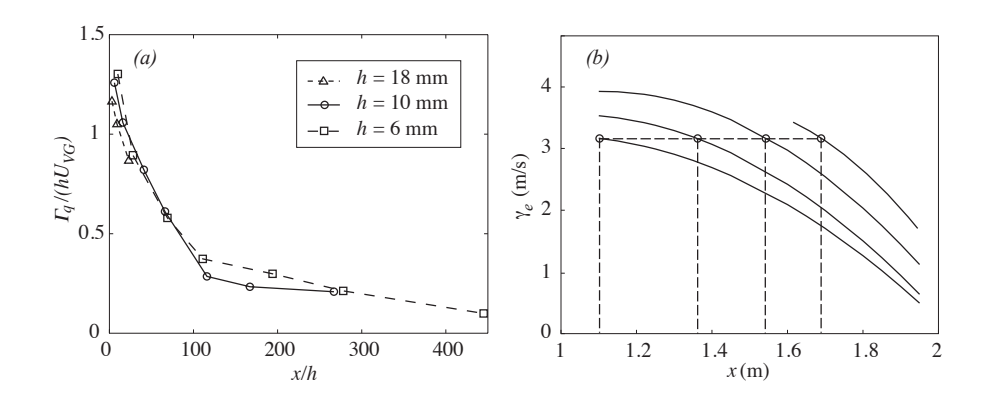


FIGURE 14. (a) Circulation decay downstream of arrays of VGs in ZPG (b)  $\gamma_e$  generated by the four different VG sizes in case III. The horizontal line indicates  $\gamma_e=3.1$  and the x-positions where it intersects with the four lines of estimated circulation shows where the VGs should be placed to generate  $\gamma_e=3.1$ .

at which position  $\gamma_e$  is generated. The position is important since the circulation decays in the downstream direction and also since the location of  $x_s$  might change.

In Lögdberg et al. (2008) the streamwise circulation decay of vortices produced by VG arrays identical to the present ones was measured in a ZPG turbulent boundary layer. As shown in figure 14(a) the circulation decay scales with h. Since the APG changes the boundary layer in which the vortices are embedded it is reasonable to assume that the rate of decay might change. However, Westphal et al. (1987) reported that even though the vortex core grows quicker in an APG and the peak vorticity becomes lower, the decay of circulation from a vortex with the same initial circulation does not change when a pressure gradient is imposed.

In figure 11 the vortices of  $\gamma_e = 3.8$  are produced by a VG array at  $x_h$  –  $x_{VG} = 81 h$ , whereas the vortices of  $\gamma_e = 1.4$  are generated at  $x_h - x_{VG} = 31 h$ . Assuming that the decay of circulation displayed in figure 14(a) is applicable, the stronger vortices would have lost 60 % of their estimated circulation at  $x_h$ , while the weaker vortices would have lost only about 20% of their circulation. The question is if it is  $\gamma_e$  at  $x_h$  which is of importance for separation control purposes or if it is the initial  $\gamma_e$ . Figure 14(a) should not be interpreted as showing the decay of the control effect. The boundary layer's capacity to withstand an APG depends on the fullness of the velocity profile and high momentum fluid is transported towards the wall despite the fact that the circulation decays, when the vortices are convected downstream. The downward momentum transport thus takes place over a longer streamwise distance for VG configurations positioned further upstream. Therefore there are two seemingly opposing consequences when the streamwise position of the VG array is moved upstream: a decreased circulation at  $x_h$  and an increased total momentum transport towards the wall.

In order to investigate the influence of the streamwise position of the VG array, the same magnitude of circulation was produced at four different x-positions. This was accomplished by applying the 6, 10, 18 and 30 mm VGs at different streamwise positions so that  $hU_{VG}$  is constant (see table 4). The procedure is illustrated in figure 14(b), which is based on the data from figure 5. Two arrays are placed before the pressure gradient peak in figure 3, one is placed at the position of the peak and one is positioned right after the maximum in the pressure gradient. The normalised distance from  $x_{VG}$  to  $x_h$  span x/h = 29 to 242.

In figure 15(a) the resulting mean streamwise velocity profiles at the spanwise positions of inflow and outflow at  $x_h$  are presented. For the case with 6 mm VGs the boundary layer has become two-dimensional. With the 10 mm VG array, the velocity profiles at the positions of inflow and outflow are slightly shifted with respect to each other, with a fuller profile at the position of inflow. For the next two cases of larger VGs and decreasing x/h, the shift of the profiles at the inflow and outflow positions increases further, showing that they have not developed as far. However, if an average of the profiles at the inflow and outflow positions are taken for each VG size, the resulting velocity profiles of the three largest VGs become quite similar. Hence,  $H_{12}$  of the average mean velocity profiles is similar. This is shown in figure 15(b), where  $H_{12}$ at the inflow and outflow positions are plotted against  $x_{VG}$ . The grey line in the figure shows the average  $H_{12}$  and one can conclude that the control effect in terms of  $H_{12}$  at  $x_h$ , is insensitive to the streamwise position and dP/dx for  $x_h - x_{VG} = 29h - 118h$ . For the most upstream VG array at  $x_h - x_{VG} = 242h$ the control effect is reduced (see table 4 for the conversion between  $x_{VG}$  and  $(x_h - x_{VG})/h$ ). Note that the resulting data points in figure 13 are all within the  $x_{VG}$ -insensitive range.

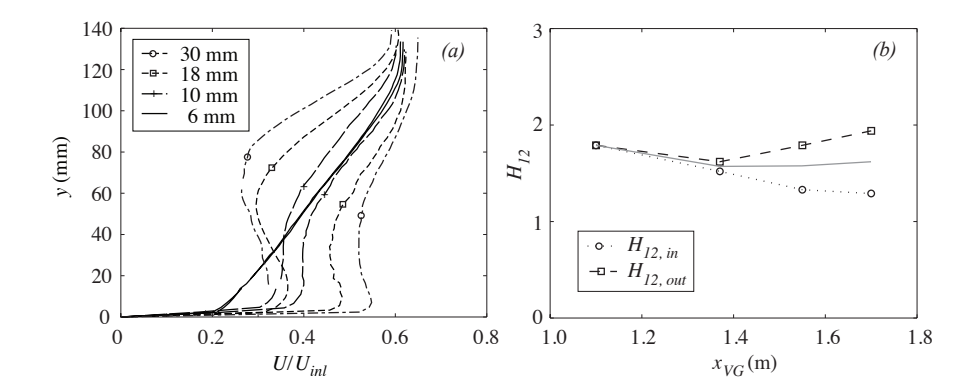


FIGURE 15. (a) Mean velocity profiles at the spanwise positions of inflow and outflow for four different VG configurations described in table 4. The four rightmost profiles are measured at the position of inflow and the others at the position of outflow. (b)  $H_{12}$  measured at  $x_h$  for an estimated generated  $\gamma_e$  of 3.1 m/s. The circulation is produced at four different x-positions. The upper curve is  $H_{12}$  at the position of outflow and the lower curve is  $H_{12}$  at the position of inflow. The grey line shows the mean  $H_{12}$ .

## 4. Conclusions

In this study the control effectiveness of conventional vane-type VGs has been investigated, for different pressure gradients and different levels of generated circulation, using PIV.

As the circulation is increased the effect on the separated region is first small, but when a critical  $\gamma_e$  is reached the flow does not separate. Since the parasitic drag of the VGs increases with  $\gamma_e$ , the lowest possible  $\gamma_e$  that still keeps the boundary layer attached is the most efficient. This, together with the sudden change to attached flow produces a pronounced efficiency maximum. However, in an application where the flow conditions vary, a system designed for maximum efficiency might be sensitive to such variations.

Figure 13 illustrates the sensitivity of the VG system. A system is designed for maximum efficiency probably produces  $\gamma_e \approx 1.5$ . If a change of the flow at  $x_{VG}$  causes  $U_{VG}$  and  $\gamma_e$  to decrease, the flow at  $x_h$  can quickly become separated. Thus, an optimised system is sensitive to variations in  $\gamma_e$ . However, if instead the pressure gradient changes, figure 13 shows that the effect is small. Thus, the VG system is not sensitive to variations in the pressure gradient.

In figure 15(a,b) it is shown that, within a range of  $x_h - x_{VG}$ , the streamwise position of the VG array is of minor importance. Thus, the VG system is not sensitive to changes of the separation point.

To conclude, flow control by means of vane-type VG arrays is robust with respect to changes in the pressure gradient and changes of separation point. However, if the system is designed for optimum efficiency it could be sensitive to changes of the flow conditions at the position of the VG array.

## Acknowledgements

Ola Lögdberg acknowledges Scania CV for the opportunity to carry out his doctoral work at KTH Mechanics within the Linné Flow Centre.

## References

- Angele, K. & Grewe, F. 2007 Instantaneous behavior of streamwise vortices for turbulent boundary layer separation control. *J. Fluids Eng.* **129**, 226–235.
- Angele, K. P. & Muhammad-Klingmann, B. 2005a The effect of streamwise vortices on the turbulence structure of a separating boundary layer. *Eur. J. Mech.* B **24**, 539–554.
- Angele, K. P. & Muhammad-Klingmann, B. 2005b A simple model for the effect of peak-locking on the accuracy of boundary layer statistics in digital PIV. *Exp. Fluids* **38**, 341–347.
- Angele, K. P. & Muhammad-Klingmann, B. 2006 PIV measurements in a weakly separating and reattaching turbulent boundary layer. *Eur. J. Mech.* B **25**, 204–222.
- DENGEL, P. & FERNHOLZ, H. H. 1990 An experimental investigation of an incompressible turbulent boundary layer in the vicinity of separation. *J. Fluid Mech.* 212, 615–636.
- Godard, G. & Stanislas, M. 2006 Control of a decelerating boundary layer. Part 1: Optimization of passive vortex generators. *Aerosp. Sci. Tech* 10, 181–191.
- KEANE, R. & ADRIAN, R. 1992 Theory of cross-correlation in PIV. App. Sci. Res. 49, 191–215.
- LIN, J. C. 2002 Review of research on low-profile vortex generators to control boundary-layer separation. *Progr. Aerosp. Sci.* **38**, 389–420.
- LIN, J. C., HOWARD, F. G. & SELBY, G. V. 1989 Turbulent flow separation control through passive techniques, AIAA-89-0976. In AIAA 2nd shear flow conf.
- LINDGREN, B. & JOHANSSON, A. V. 2004 Evaluation of a new wind-tunnel with expanding corners. *Exp. Fluids* **36**, 197–203.
- LÖGDBERG, O., ANGELE, K. & ALFREDSSON, P. H. 2008 On the scaling of turbulent separating boundary layers. *Phys. Fluids* **20** 075104.
- LÖGDBERG, O., FRANSSON, J. H. M. & ALFREDSSON, P. H. 2008 On the streamwise evolution of longitudinal vortices in a turbulent boundary layer. *J. Fluid Mech.* (in press).
- Pauley, W. R. & Eaton, J. K. 1988 Experimental study of the development of longitudinal vortex pairs embeddedd in a turbulent boundary layer. *AIAA J.* **26**, 816–823.

- Pearcy, H. H. 1961 Boundary layer and flow control, its principle and applications, Vol 2, chap. Shock-induced separation and its prevention, pp. 1170–1344. Pergamon.
- Raffel, M., Willert, J. & Kompenhans, J. 1997 Particle Image Velocimetry. A practical guide. Springer-Verlag.
- Schubauer, G. & Spangenberg, W. 1960 Forced mixing in boundary layers. J. Fluid Mech. 8, 10–32.
- SMITH, F. 1994 Theoretical prediction and design for vortex generators in turbulent boundary layers. *J. Fluid Mech.* **270**, 91–131.
- Westphal, R. V., K., E. J. & Pauley, W. R. 1987 Interaction between a vortex and a turbulent boundary layer in a streamwise pressure gradient. In *Turbulent shear flows 5* (ed. F. Durst, B. E. Launder, J. L. Lumley, F. W. Schmidt & J. H. Whitelaw), pp. 266–277. Springer.

4

# Separation control by an array of vortex generator jets. Part 1. Steady jets.

## By O. Lögdberg<sup>1,2</sup>

<sup>1</sup>Linné Flow Centre, KTH Mechanics, S-100 44 Stockholm, Sweden <sup>2</sup>Scania CV AB, S-151 87 Södertalje, Sweden

The effect of longitudinal vortices produced by an array of steady jets on a separation bubble was examined experimentally. A adverse pressure gradient on a flat plate causes the turbulent boundary layer to separate. The jets are originating from orifices in the wall and are directed  $45^{\circ}$  from the wall and  $90^{\circ}$  from the mean flow direction. In the centre of the separated region, particle image velocimetry (PIV) is used to measure the momentum increase near the wall that the vortices produces. An effect maximum is found for a jet velocity that is 5 times the test section inlet velocity. Maxima based on volume flow efficiency and energy efficiency are also found at lower jet velocities. Furthermore, it is shown that the highest possible effect of the jet array is comparable to that of a vane-type vortex generator array. In sidewind, the jet array is shown to be effective at yaw angles up to  $40^{\circ}$ .

### 1. Introduction

Control of separation of boundary layer flows can be achieved through different approaches. One common method, that has proved to be effective, is to introduce longitudinal vortices in the boundary layer. The vortices enhance mixing and transport high momentum fluid towards the wall. In the past, the vortices have been produced by vane-type vortex generators, *i.e.* short wings attached to the surface with the wingspan in the wall-normal direction and set at an angle towards the mean flow direction. Such devices are commonly seen on the wings of commercial aircraft. An alternative way of producing the vortices is by jets originating from the wall and lately there have been several studies on vortex generator jets (VGJs). This study complements and extends earlier work on VGJs and is divided in two parts, dealing with steady (present paper) and pulsed jets (Lögdberg (2008)), respectively.

#### 1.1. Background

Circular jets in cross-flow are known to produce a multitude of vortical structures. The complex interaction between the oncoming flow and the jet surface

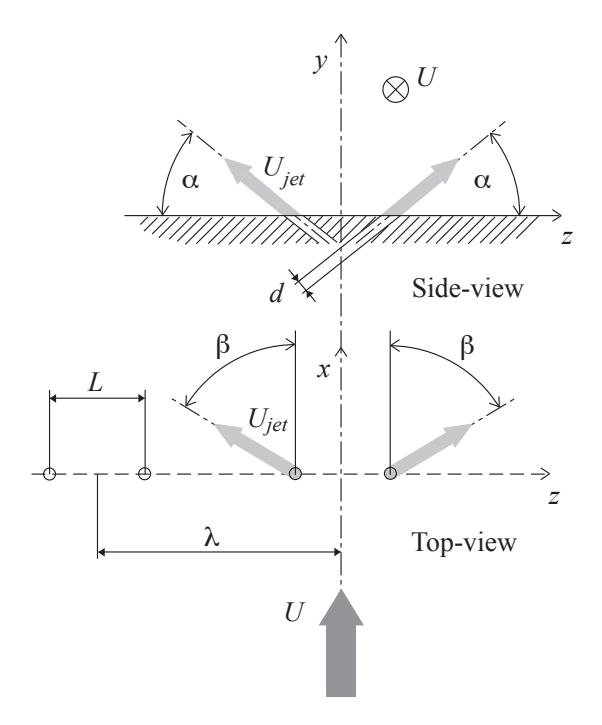


FIGURE 1. Schematic of a VGJ device producing counterrotating vortices. Note that the figure is in first-angle projection. U is the free stream mean direction and  $U_{jet}$  is the jet velocity. The direction of the jet is defined by the pitch angle  $\alpha$  and the skew angle  $\beta$ . The jet exit diameter is named d, the distance between the jets of a VGJ pair L and the distance between the pairs in an array  $\lambda$ . For a co-rotating array there is no L and thus  $\lambda$  is the distance between the jets.

vortex sheet generates a counter-rotating vortex pair as the jet is deflected in the cross-flow direction. The mechanism is still not completely understood, but plausible models are presented by Kelso *et al.* (1996) and Lim *et al.* (2001). If the jet is inclined relative to the cross-flow, one of the vortices will grow stronger, as explained by Zhang (2003). The vortex pair from an inclined jet will thus form a primary and a secondary vortex.

Flow control by VGJs was first described by Wallis (1952). He claimed that an array of VGJs is as effective as passive vortex generators in suppressing separation on an airfoil. One advantage of an active system is that it can be turned off when it is not needed and thus the parasitic drag of conventional vortex generators can be avoided. In the following the jet direction is given

by the skew and pitch angle, see figure 1 for a definition of the geometry. The pitch angle  $\alpha$  is the angle between the wall and the jet centreline. Skew is the angle  $\beta$  between the wall projection of the jet centreline and the free stream direction. Note that in some studies the skew angle is referred to as yaw angle.

After some more experiments by Wallis very little was published until the 1990s. The study by Johnston & Nishi (1990) demonstrated how streamwise vortices are produced by an array of pitched jets at 90° skew. A pitch angle of less than 90° was needed in order to generate a strong primary vortex. Some success in reducing the size of a separated region in an adverse pressure gradient (APG) was also demonstrated when the velocity ratio VR, which is the ratio of the jet velocity to the free stream velocity, was 0.86 or higher.

Compton & Johnston (1992) studied VGJs pitched at 45° and skewed from 0-180° from the mean flow (a skew angle larger than 90° means that the jet is directed in the upstream direction). A skew angle between 45 and 90° was found to give the strongest vortices. The circulation of the vortices was also found to increase monotonically as the VR was increased up to 1.3. A comparison to vane-type VGs showed that the vortices from the jets decayed more rapidly.

In a study on a zero pressure gradient (ZPG) flow followed by a backward facing ramp with a slope of  $25^{\circ}$ , where the flow separates, Selby, Lin & Howard (1992) (SLH1992) measured the increase in pressure recovery of different VGJ array configurations. The pressure recovery increased monotonically up to the highest tested VR ratio of 6.8. It was shown that a small pitch angle ( $15^{\circ}$  or  $25^{\circ}$ ) is beneficial, since momentum transfer occurs closer to the wall. The optimum skew angle appears to be between  $60^{\circ}$  and  $90^{\circ}$ . A comparison with tangential slot blowing at an equal flow rate per unit width showed substantially better pressure recovery for the VGJ case. Since this is one of the most comprehensive studies made on VGJ arrays, the main characteristics are listed in table 1.

According to the review by Johnston (1999) the VR is the dominant parameter in generating circulation. He also concludes that a pitch angle below  $30^{\circ}$  and a skew angle in the range  $60^{\circ}$  to  $90^{\circ}$  from the free stream are the most effective. The exact streamwise location of the VGJ row seems less important since the boundary layer reacts likewise independent of where it is energised. The VGJ spacing, the hole diameter and the hole shape are yet to be optimised.

Khan & Johnston (2000) showed detailed measurements of the flow field downstream of one VGJ. Their data support earlier experiments when they claim that a skew angle of  $60^{\circ}$  produces the highest peak vorticity. For pitch they write that  $30^{\circ}$  is the optimum angle, but the only other angle that is tested is  $45^{\circ}$ . The flow field seems similar to that of solid VGs.

Zhang (2000) showed that a rectangular jet can produce higher levels of vorticity and circulation compared to a circular jet of equal hydraulic diameter and VR. The circulation decay with distance is linear for both nozzle configurations. The complicated near field structures around a rectangular skewed jet

was earlier investigated by Zhang, Zhang & Hurst (1996). Another experiment on the jet orifice shape by Johnston, Moiser & Khan (2002) showed that the inlet geometry affects the near-field but not the far-field.

For a single VGJ with a fixed direction, the VR was varied in an experiment by Rixon & Johari (2003). The jet creates a pair of vortices of which one is significantly stronger. The weak vortex was found to decay rapidly and only the strong one persisted downstream. Both circulation and the vortex centre distance to the wall increased linearly with VR for ratios between one and three. The vortex core was observed to meander up to  $0.3\,\delta$  in both the wall normal and spanwise directions.

Zhang (2003) studied co-rotaing vortices produced by a spanwise array of VGJs where both skew and pitch are set to  $45^{\circ}$ , and described the complicated near field. The ratio of vortex strength of the primary and secondary vortices (cf. Rixon & Johari (2003)) are shown to depend on VR. Compared to a single vortex the array of co-rotating vortices experience a larger spanwise movement as they evolve downstream, but after a certain distance opposing secondary flow structures seem to halt the spanwise motion.

In all previous reports the vortex strength has been reported to increase monotonically with VR, but Milanovic & Zaman (2004) finds a maximum in the region of VR = 2.0–2.8. The optimum skew angle and pitch angle are in accordance with earlier experiments.

The most extensive investigation in recent years is the one by Godard & Stanislas (2006) (GS2006). It is the third part in a larger study of flow control by longitudinal vortices in an APG without separation. They measure the skin friction increase for different VGJ configurations producing co-rotating and counter-rotating vortices. Their data show that optimised VGJs produce results comparable to passive vane-type VGs in terms of skin friction. For a counter-rotating pair their optimal set of parameters are:  $\beta=45-90^{\circ}$ ,  $\alpha=45^{\circ}$  and L/d=15. They show a strong increase in skin friction with jet velocity up to VR=3.1. Above that there is almost no increase. They also reported that the counter-rotating VGJ pair is effective at free stream skew angles up to  $20^{\circ}$ . The main characteristics of this study are also listed in table 1.

## 1.2. Present study

This study focuses on the VGJ array as a system, but not on the detailed flow physics. Of the above mentioned works the ones by SLH1992 and GS2006 have been the most influential on the present investigation. Here an array of VGJs, that spans the full width of a flat plate, is used to control a separation bubble. The measurement technique used here makes it easier to quantify the control effect as compared to SLH1992. The difference compared to GS2006 is that the uncontrolled flow separates and that the VGJs form an array.



Figure 2. Rotatable VGJ device mounted flush in Plexiglass plate.

## 2. Vortex generator jets

The intention of this study was not to optimise the VGJ geometry. This has already been done by SLH1992, GS2006 and others.

#### 2.1. VGJ devices

Here a counter-rotating configuration was chosen for the VGJ array, because of our earlier experiences of counter-rotating vane-type VGs (see Angele & Muhammad-Klingmann (2005a), Lögdberg et al. (2008c) and Lögdberg et al. (2008b)) in the BL wind tunnel at KTH. The geometry was chosen in agreement with the results of the above mentioned studies, although modified to suit the wind tunnel. The skew and pitch angles are chosen as 90° and 45°, respectively. The distance between the jets of the VG device is 40 mm and the diameter of the circular jet is 2.5 mm. This results in L = 16 d, which is close to the optimum according to GS2006. However, in their set-up  $L/\delta_{99} = 0.6$  and in our set-up it is 1.6. Since others have shown good results with L > 1 this geometry was judged to be a good compromise. To ease future configuration changes the distance between the devices was set to 80 mm ( $\lambda = 2L$ ). An array that spans the full wind tunnel width of 0.75 m will then consist of 9 VGJ devices (18 jets). A compressor with a capacity of 25 g/s at 4 bar and 18 jets with d = 2.5 mm, the maximum sustainable jet velocity is 220–230 m/s, which corresponds to VR = 8-9 at a test section inlet velocity  $U_{inl}$  of 26.5 m/s. This produces a reasonable VR range for the experiment. The most important geometry quantities of the VGJ devices used in this experiment are listed in table 1.

To be able to yaw each VGJ pair individually, the VGJ devices consist of 50 mm diameter cylindrical aluminum plugs. In figure 2 two plugs of the array can be seen. Through the Plexiglas, in which the plug is mounted, two of the

adjustment screws are visible. With these, fine adjustment of the plugs are possible, to avoid steps between the plug and the plate. There is an air supply inlet for each jet and they are placed on the lower side of the plug. The inlets are normal to the surface of the plug and thus there is a 45° bend of the air channel inside the plug.

 $\alpha$ ,  $\beta$ , d, L and  $\lambda$  are defined in figure 1.  $\delta$  is the boundary layer thickness at the streamwise position of the VGJ array,  $n_{jet}$  is the number of jets in the array, VR is the range of jet velocity ratios and  $\Delta x_{sep}$  is the distance from the VGJs to the separation point. Table 1. The main features of the VGJ systems of the present experiment, of SLH1992 and of GS2006.

Configuration	$\alpha$ ( $_{\circ}$ )	$\beta$ (°)	d  (mm)	L  (mm)	$\lambda \; (\mathrm{mm})$	$\delta$ (mm)	$n_{jet}$	VR	$\alpha$ (°) $\beta$ (°) $d$ (mm) $L$ (mm) $\lambda$ (mm) $\delta$ (mm) $n_{jet}$ $VR$ $\Delta x_{sep}$ (m)
Present experiment									
Ctrrotating	45	06	2.5	40	80	26 - 27	18	0.5-7	$\approx 0.6$
Ctrrotating	45	06	2.5	40	160	26 - 27	6	3, 5	$\approx 0.6$
Co-rotating	45	06	2.5	1	80	26 - 27	6	3, 5	$\approx 0.6$
SLH1992									
Ctrrotating	15-90	06-0	0.8-4.8	30	30	33	10	0.6 - 6.8	$\approx 0.1$
Co-rotating	15-90	06-0	0.8-4.8	1	30	33	10	0.6 - 6.8	$\approx 0.1 - 1.3$
GS2006									
Ctrrotating	45	45-135	9	48-138	ı	167	2	1.6 - 4.7	No sep.
Co-rotating	45	45,90	4, 6		24 - 100	167	3-6	1.6 - 4.7	

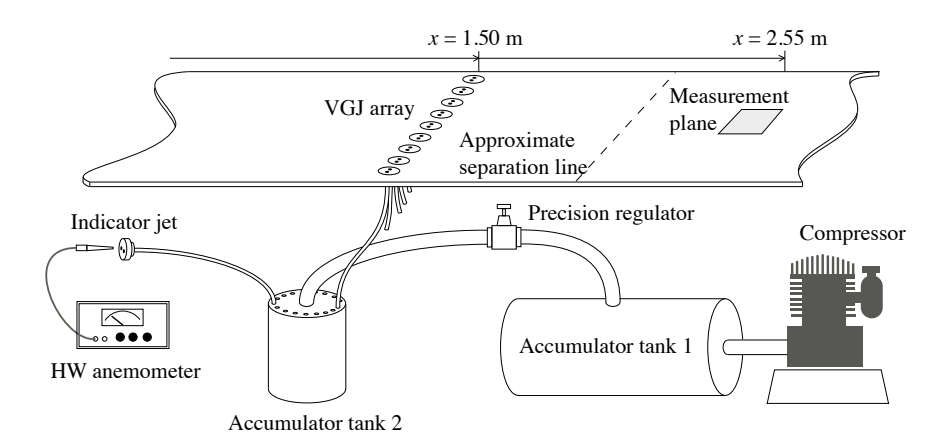


FIGURE 3. Schematic of VG set-up. The tubes between the compressor, accumulator tank 1 and accumulator tank 2 is approximately 20 m each. The measurement plane is parallel to the wall and located at the flat plate centreline, 5 mm from the wall.

#### 2.2. VGJ installation

As already mentioned, the array of VGJ devices are mounted on a Plexiglas plate. This can be seen in figures 3 and 4. The high pressure air for the jets, produced by a compressor is then fed to the 0.3 m³ accumulator tank 1 via a 20 m hose. The compressor keeps the pressure in accumulator tank 1 at 7–8 bar and the large volume of the tank enables the jets to run at higher jet velocities for short periods. On the hose between accumulator tanks 1 and 2 there is a SMC IR3020 precision regulator to control the jet velocity. The 0.012 m³ accumulator tank 2 is located outside the wind tunnel and connects the large supply hose to the 18 4 mm (inner diameter) tubes that feed the VGJ devices in the wind tunnel. In figure 4 one can observe valves on the 4 mm tubes. They are used for the pulsed jets discussed in Lögdberg (2008).

One of the VGJ devices is placed outside the wind tunnel. It is identical to the ones in the array and connected to accumulator tank 2 with a tube of the same length and diameter as the others. A straight hot wire probe, connected to a Dantec DISA 55M10 anemometer, is used to measure the jet centreline velocity  $U_{CL}$ . The jet velocity is continuously monitored during the experiments, and kept within  $\pm$  3 m/s.

## 2.3. Jet results

Before the separation control experiments the main characteristics of the VG jets were studied.

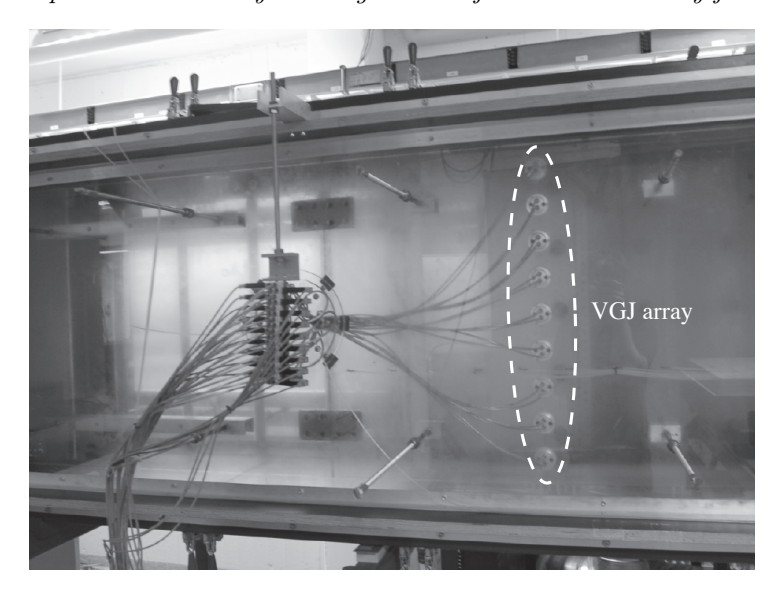


FIGURE 4. The VGJ array seen from below the plate. The valves seen outside the test section are not used in this experiment.

To measure the jet exit velocity profile a single-wire probe was traversed over the jet exit hole at y/d=0.4. The measurements are thus not taken perpendicular to the jet axis. The jet centreline velocity was varied from 26.5 to 159 m/s, or VR=1-6, by adjusting the pressure in accumulator tank 2. As expected there was a linear relationship between the square of  $U_{CL}$  and the pressure.

In figure 5(a) the velocity profiles for VR=1-6 are shown normalised by  $U_{CL}$ . In the figure the positive x direction is from the centre of the VGJ plug and outwards. Except for a small deviation for VR=1, all U profiles are self-similar. At y/d=4 the profile for VR=3 is shown and the spreading of the jet is clearly seen. For clarity the data for y/d=4 in the figure is centered around  $x/d_x=0$  despite the jet angle.

The asymmetry of the velocity profile is due to the 45° angle in the plug channel. A CFD computation of the channel geometry produced the same skewed profile. In the computation it was shown that flow separation at the inner corner of the bend in the channel produced the asymmetry.

The rms-profiles in figure 5(b) are also quite similar, although less so than the velocity. The two peaks in rms are, as expected, found where the mean velocity gradient is the largest. Between the peaks  $u_{rms}$  increases with the jet velocity.

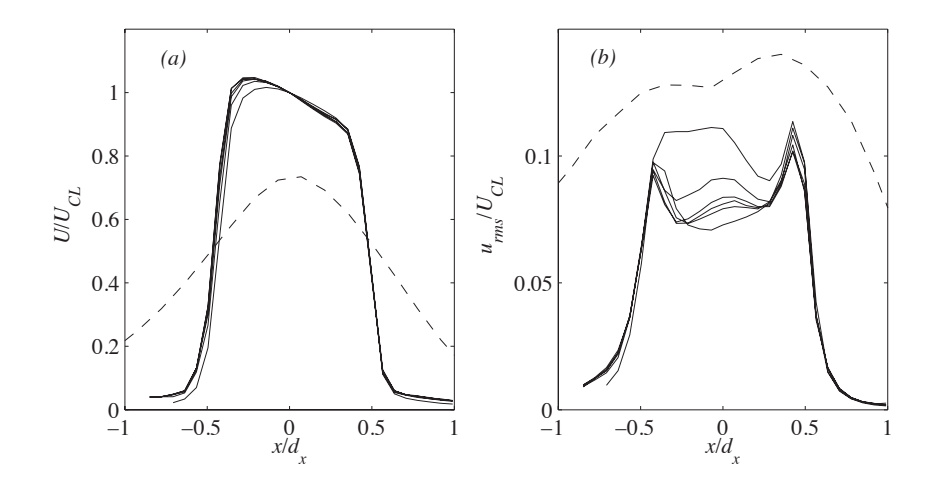


FIGURE 5. (a) The full lines show  $U/U_{CL}$  at y/d=0.4 for VR=1–6 and the dotted line shows  $U/U_{CL,y/d=0.4}$  at y/d=4 for VR=3. (b)  $u_{rms}/U_{CL,y/d=0.4}$  at y/d=0.4 and y/d=4 mm. Note that  $d_x$  is  $d/\sin 45^\circ$ .

#### 3. Experimental set-up

The VGJs were evaluated in a wind tunnel, where pressure measurements and PIV measurements were performed.

#### 3.1. Wind tunnel

All experiments were performed in the KTH BL wind tunnel, with a free stream velocity of 26.5 m/s at the inlet of the test section. The test section, which is shown in figure 6, is 4.0 m long and has a cross-sectional area of 0.75 m×0.50 m (height×width). For a detailed description of the wind tunnel, the reader is referred to Lindgren & Johansson (2004). A vertical flat plate made of Plexiglas, which spans the whole height and length of the test section, is mounted unsymmetrically with its back surface 300 mm from the back side wall of the test section. The plate is equipped with pressure taps, separated by  $\Delta x = 0.1$  m, along the centreline. At x = 1.25 m, the back side wall diverges in order to decelerate the flow. Suction is applied on the curved wall to prevent separation there. The induced APG on the flat plate can be varied by adjusting the suction rate through the curved wall. The measurements are made with PIV and for a detailed description of the experimental set-up the reader is referred to Angele & Muhammad-Klingmann (2005a,b).

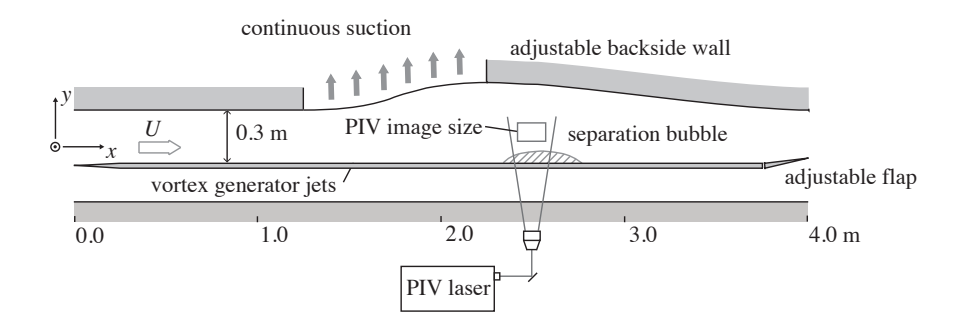


FIGURE 6. Test section with plate model. Here the PIV system is arranged to measure a x-y plane.

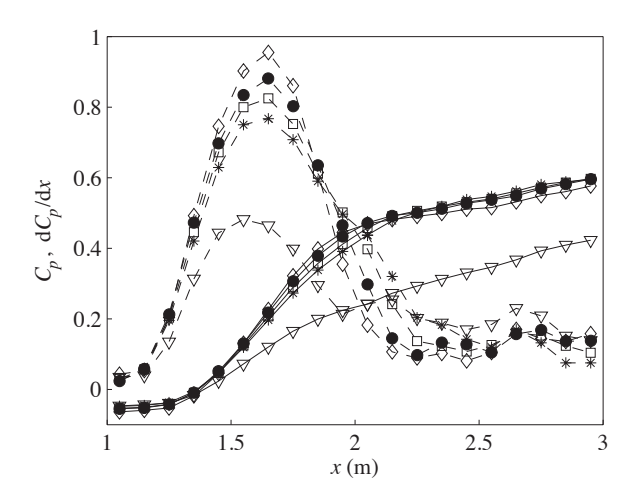


FIGURE 7. The pressure and its gradient at APG-1 ( $\nabla$ ), APG-2 (\*), APG-3 ( $\square$ ), APG-4 (•) and APG-5 ( $\diamond$ ).

# 3.2. Pressure measurements

The wall static pressure P was measured along the spanwise centreline using a 16 channel Scanivalve pressure scanner. The pressure transducer has an accuracy of  $\pm$  0.2% of full scale (2500 Pa), which in the present experiment produces a measurement accuracy of  $\pm$  3%. The pressure coefficient

$$C_p = \frac{P - P_{ref}}{P_0 - P_{ref}} \tag{1}$$

for the wall static pressure and its gradient in the flow direction are plotted in figure 7 against the distance from the leading edge of the test plate.  $P_{ref}$  is taken on the wall at x=0.45 m and  $P_0$  is the total pressure at the same xposition.

#### 3.3. PIV set-up

The PIV-system used consists of a 400 mJ double cavity Nd:Yag laser operating at 15 Hz and a  $1018 \times 1008$  pixels CCD camera with 8 bit resolution. The air was seeded with smoke droplets generated by heating glycol injected in the pressure equalizer slit downstream of the test section. The droplets are large enough to render a particle image size larger than 2 pixels in all measurements. According to Raffel et al. (1997) this is enough to avoid peak-locking due to problems with the peak-fit algorithm. Also the ratio between the discretization velocity  $u_d$  and the rms-value of the streamwise velocity is close to 2 in all measurements. According to Angele & Muhammad-Klingmann (2005b) this reduces errors due to peak-locking effects in mean- and rms-values to approximately 1%.

Conventional post-processing validation procedures of the PIV image pairs were used. No particles moving more than  $25\,\%$  of the interrogation area length between two images were allowed in order to reduce loss-of-pairs and the resulting low-velocity bias. The peak height ratio between the highest and the second highest peak in the correlation plane must be more than 1.2 if the vector should be accepted.

#### 3.4. Hot-wire

Hot-wire measurements were performed to characterize and monitor the jet. A single-wire probe with a welded 5  $\mu$ m tungsten wire was used. The wire length is 1.2 mm and the probe was connected to a Dantec DISA 55M10 anemometer. The probe was calibrated before each measurement series (*i.e.* once per day).

#### 4. Separation control

There are two ways of studying the effect of VGs. The generated circulation or vorticity can be measured at different positions in the flow field. Alternatively the region of the flow that the VGs are designed to influence is studied. Here the second approach is chosen.

#### 4.1. The uncontrolled case

The curvature of the wall causes a pressure gradient that can be further increased by applying suction. Flow control will be applied at four different APG cases. They are chosen so that the first is on the verge of separation, the fourth the largest possible separation bubble and the other two evenly distributed in between. They will henceforward be called APG case 2–5. APG case 1 is without suction. What restricts the size of the case 5 separation bubble is the

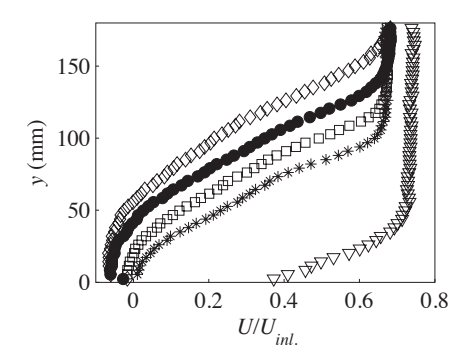


FIGURE 8. Mean velocity profiles at  $x=2.55~\mathrm{m}$  and  $z=0~\mathrm{mm}$ . Symbols as in figure 7

capacity of the suction system. The baseline case in the flow control study will be case 4.

Figure 7 shows the pressures and the pressure gradients of the five APG cases. The four largest pressure gradients have their maxima at approximately x=1.65 m. Without suction the pressure gradient is weak. The streamwise position of separation  $x_{sep}$  was not measured, but considering the results in the same wind tunnel at an almost identical APG presented in Lögdberg  $et\ al.$  (2008a) a reasonable estimate is  $x_{sep}\approx 2.1$  m for case 4.

In Lögdberg et al. (2008a) the position of maximum bubble height and the position of maximum backflow coefficient  $\chi_{wall}$  was shown to coincide at  $x_h=2.55$  m for all pressure gradients. Because of the similarity mentioned above it was assumed that the bubble maximum was located near that position also in this set-up. For this experiment the exact position is not so important, but it is vital that it is fairly constant. For approximately the same set-up it was shown in Lögdberg et al. (2008b) that even for large separation bubbles the flow is two-dimensional around the centreline at  $x_h$ .

The velocity profiles of the different APG cases, at  $x_h$ , are shown in figure 8. The free stream velocity  $U_e$  is reduced by approximately 2 m/s when suction is applied. However, when the suction flow is further increased to enlarge the separated region,  $U_e$  remains constant. Thus, at increased suction ratios the increased blockage from the separation bubble seems to balance the reduced flow after the suction region. For the other APG cases the height of the separation bubble, defined as  $\chi > 0.5$ , ranges from 0 to 60 mm.

#### 4.2. Effect measure

In order to compare many different flow control configurations a simple scalar measure of the control effect is helpful. Since the purpose of introducing the vortices in the flow is to transport momentum towards the wall, measuring



#### O. Lögdberg

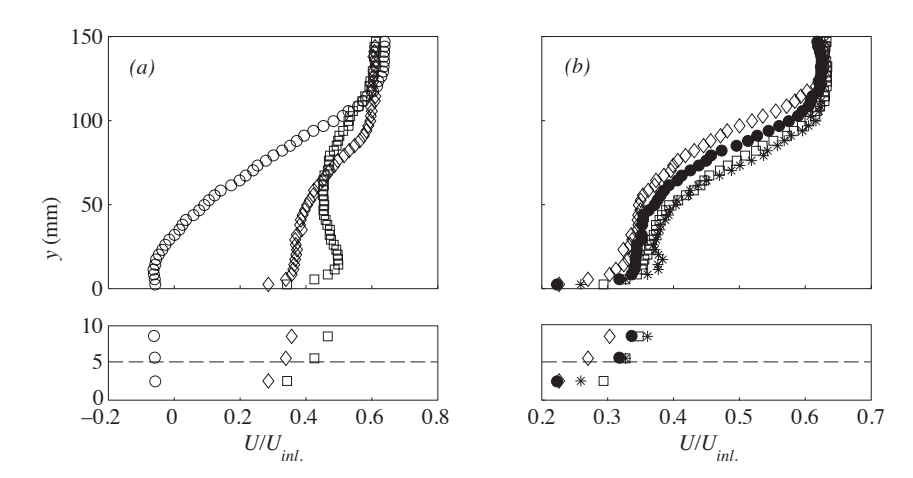


FIGURE 9. (a) Velocity profiles at baseline APG for VR = 0, VR = 3 and VR = 6. (b) Velocity profiles for APG cases 2 (\*), 3 ( $\square$ ), 4 ( $\circ$ ) and 5 ( $\diamond$ ) at VR = 3.

the momentum increase near the wall at the streamwise position of maximum backflow  $(x_h)$ , seems to be a straightforward method. To be able to detect small differences a large range or a high accuracy is needed; preferably both. At y=5 mm the backflow of the uncontrolled case 4 has reached  $U/U_{inl}=-0.075$ , which is close to its maximum value. Consequently, velocity measurements at that position could potentially provide a good range and it is still close enough to the wall for the velocity to be approximately zero when the flow is on the verge of separation, i.e. when  $\partial U/\partial y=0$  at y=0 mm. Furthermore it is far enough from the wall to avoid most of the disturbances from dust particles on the wall when measuring an x-z plane with PIV. By measuring a plane parallel to the wall the accuracy is increased, since the small gradient makes it possible to average the data in the streamwise direction. The resulting velocity, normalised by  $U_{inl}$ , will be called  $U_5$  in the following. From  $U_5$  a scalar effect measure can be calculated by averaging the velocity over one wavelength  $\lambda$  in the spanwise direction. This scalar will be termed  $\overline{U}_5$ .

The approximate position of the measurement plane is shown in figure 3. The wall-normal position of the laser sheet is at  $y=5\pm0.5$  mm and its thickness is approximately 1.5 mm. Furthermore, the sheet is not completely parallel to the wall. The spanwise angle error is, however, less than 0.1°. The error in the streamwise angle is estimated to be less than 0.3°. Due to the difficulty in reproducing the same laser sheet, all x-z planes at y=5 mm were measured in a sequence, without touching the laser and the camera of the PIV system. Thus the different configurations of this experiment can be accurately compared, but if  $\overline{U}_5$  is calculated from other data the accuracy is reduced.

In figures 9(a,b) the suitability and limitation of  $\overline{U}_5$  as effect measure is demonstrated. Figure 9(a) show velocity profiles at VR=0, 3 and 6 in APG case 4. As shown in the magnification, below the main figure, the range of  $U_5$  is approximately 0.5 and increasing with increasing VR. If instead VR is kept constant and the pressure gradient varied  $U_5$  increases with decreasing pressure gradient for the three cases with separated flow without control. For case 2, which does not separate, the momentum transfer produces a peak at y=15–20 mm, but leaves  $U_5$  unchanged compared to case 3. Thus  $\overline{U}_5$  seems to work in APG cases 3–5 and for the range of VRs applied in this experiment.

For a ZPG turbulent boundary layer with the same free stream velocity (Lögdberg et al. (2008c))  $\overline{U}_5$  is 0.68 at x=2.55 m.

#### 4.3. VGJ position

Both the passive and the active vortex generators are positioned at  $x_{VG} = 1.5$  m. There the momentum thickness Reynolds number is approximately 6000 and  $\delta = 26 - 27$  mm, depending on the pressure gradient. For case 4 this is approximately 0.6 m upstream of the separation line.

#### 4.4. Vane-type VG

In the the earlier experiments described in Angele & Muhammad-Klingmann (2005a) and Lögdberg et~al.~(2008b) square-bladed vane-type vortex generators were used to successfully control separation in a set-up similar to the present. Here the same passive VGs were applied in APG case 4. The VGs produce counter-rotating vortices with common downflow and exist in three different sizes, which are geometrically self-similar. The VGs are mounted in an array at  $x_{VG}$ . In figure  $10(a)~U_5$  profiles at  $x_h$  are shown for VG heights h=6, 10 and 18 mm. As expected the larger VGs, that produce more circulation, increases  $U_5$ . Furthermore, the wavelength amplitude is relatively larger for the stronger vortices, i.e. the velocity difference between the positions of inflow and outflow increases.

The circulation per unit width generated by an array of VGs can be estimated as

$$\gamma_e = 2k \frac{hU_{VG}}{D}. (2)$$

where  $U_{VG}$  is the mean velocity at the VG blade tip and k is a coefficient that is a function of the geometry of the VG. Lögdberg et~al.~(2008c) measured the circulation produced by the above mentioned VGs in a ZPG and found k to be  $0.6 \pm 0.05$ . Since the boundary layer profile is known at the position of the VG arrays,  $\gamma_e$  can be determined in the present set-up. Obviously, k might change due to the APG, but in Lögdberg et~al.~(2008b) it is shown that the velocity profiles at  $x_{VG}$  are quite constant. In figure  $10(b)~\overline{U}_5$  is shown for varying  $\gamma_e$ .

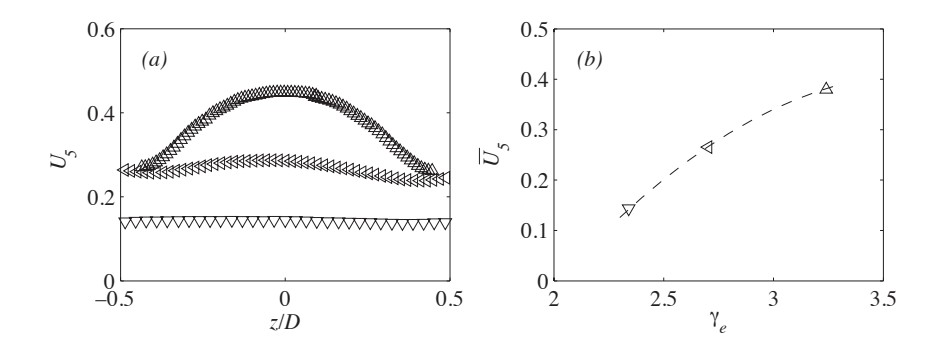


FIGURE 10. (a) Velocity profiles at y=5 mm for h=6 mm ( $\triangledown$ ), h=10 mm ( $\triangleleft$ ) and h=18 mm ( $\triangle$ ). (b) The corresponding averaged velocities  $\overline{U}_5$  at different  $\gamma_e$ .

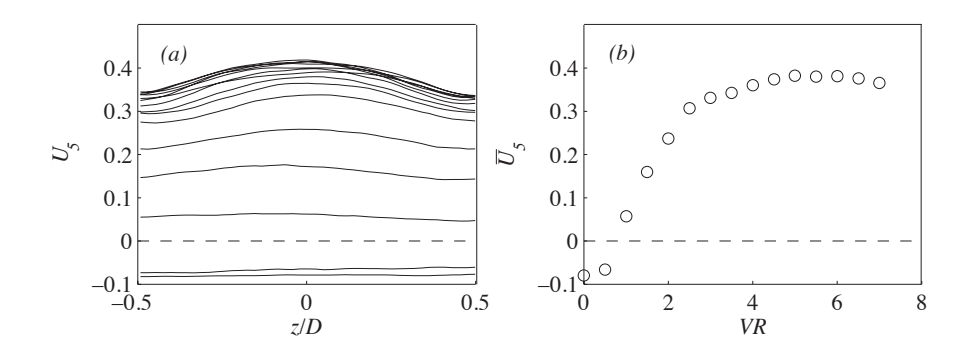


FIGURE 11. (a) Velocity profiles at y=5 mm for different VR and (b) the corresponding mean velocities  $\overline{U}_5$ .

# 4.5. Jet vortex generators

4.5a. Velocity ratio. With a fixed geometry the only variable parameter of the VGJs is VR. Here VR is varied between 0 and 7, i.e.  $U_{jet}=0-185$  m/s. Figures 11(a,b) show that  $\overline{U}_5=-0.075$  without the jets, at VR=0. There is almost no change when the jet are activated at VR=0.5. Possibly, this is because the jets are still too weak to produce any vortices. A further velocity increase to VR=1.0 turns the backflow into the mean flow direction. Thus, there are now longitudinal vortices present in the boundary layer. From VR=0.5 to VR=2.5 the increase in  $\overline{U}_5$  with VR is approximately linear. After that and up to VR=5.0 the control effectiveness is still increasing, but at a lower rate. Above VR=5.0 there is a decrease in  $\overline{U}_5$ .

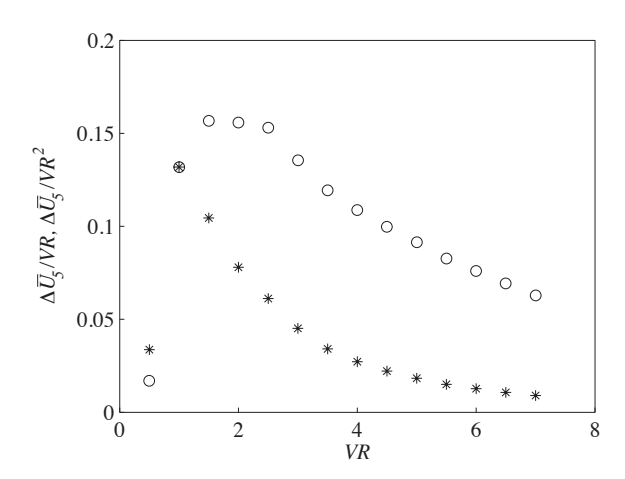


FIGURE 12. The volume flow efficiency  $\Delta \overline{U}_5/VR$  ( $\circ$ ) and the energy efficiency  $\Delta \overline{U}_5/VR^2$  (\*) at different VR.

For a vane-type VG array with h>18 mm, the increase in  $\gamma_e$  with h is small since the h is close to the boundary layer thickness and thus  $U_{VG}$  is already close to the free stream velocity. Therefore the maximum  $\overline{U}_5$  for the VG array is only slightly larger than 0.38. Likewise, for the jet array, the maximum  $\overline{U}_5$  is slightly larger than 0.38. It is a coincidence that  $\overline{U}_{5,max}$  is exactly the same for both cases, but there appears to be a maximum level of control effect possible with longitudinal vortices. Note that the accuracy of the y position of the laser sheet is such that quantitive comparisons to previously obtained data in the same set-up are uncertain.

If the available flow rate for the VGJs is limited, it is interesting to study flow control efficiency instead of effectiveness. Since VR is proportional to the volume flow rate, it can be used to normalise  $\overline{U}_5$  to produce a measure of volume flow efficiency. In order to avoid negative data points  $\Delta \overline{U}_5 = \overline{U}_5 - \overline{U}_{5,VR=0}$  is now used as the effect measure. In figure 12  $\Delta \overline{U}_5/VR$  is shown to have a maximum in the region VR=1.5-2.5. This coincides with the end of the linear region in figure 11(b), after which the rate of increase in  $\overline{U}_5$  decreases. If instead the kinetic energy of the jet is considered, the effect measure is scaled with  $VR^2$ , and the maximum efficiency is achieved at VR=1.0.

An expression for  $\gamma_e$  that approximates the data in figure 10(b) with a least squares fit was used to produce figure 13. Here the estimated levels of  $\gamma_e$  produced at different VRs are shown. As in the report by Rixon & Johari (2003) the circulation increases in a fairly linear way between VR=1.0 and VR=3.0. At VR>3.0 the gradient is decreasing until VR=5.0, where  $\gamma_e$  start to decrease. The circulation calculated from  $\overline{U}_5$  is only the effective

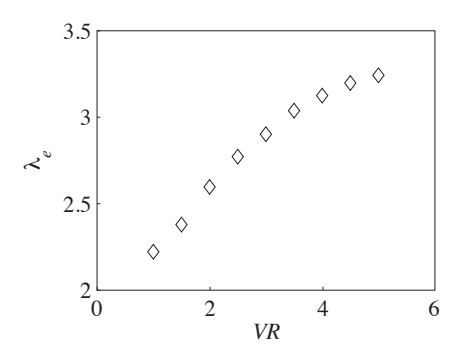


FIGURE 13. Estimated circulation produced at different VR. Above VR = 5 the estimate is no longer credible.

TABLE 2. The velocity ratio that produces a boundary layer on the verge of separation for different APGs.

Case	$h_s \text{ (mm)}$	$(dC_p/dx)_{max}$	$VR_{\chi_w=0}$	$\gamma_e$
APG-3	24	0.82	0.70	2.10
APG-4	40	0.88	0.85	2.15
APG-5	49	0.95	1.00	2.21

circulation, *i.e.* the part of the produced circulation that affects the boundary layer at  $x_h$ . For VR > 5.0 the vortices are probably formed partly outside the boundary layer and consequently the estimate is no longer valid.

Since both the pressure gradient and the generated circulation can be varied it is possible to test at what level of VR or  $\gamma_e$  separation is inhibited. This was done by measuring x-y planes at z/D=0 and adjusting the jet velocity until  $\partial U/\partial y=0$ . The circulation required differs only marginally between the APG cases. The necessary VR varies between 0.70 and 1.00 as shown in table 2. For APG-4 the flow remain attached when  $VR\geq0.85$ .

4.5b. Cross-planes. In order to get a better view of the flow field at  $x_h$  an y-z plane is plotted. The y-z plane contours shown in figure 14 are produced by interpolating data from several x-z planes at  $y=5,\,10,\,20,\,30,\,40,\,50,\,60$  and 75 mm.

Between the two counter-rotating vortices, at z/D = 0, the vortices produce a downflow that transport streamwise momentum towards the wall. The effect of this can be seen for VR = 3 in figure 14(a), where the velocity contours

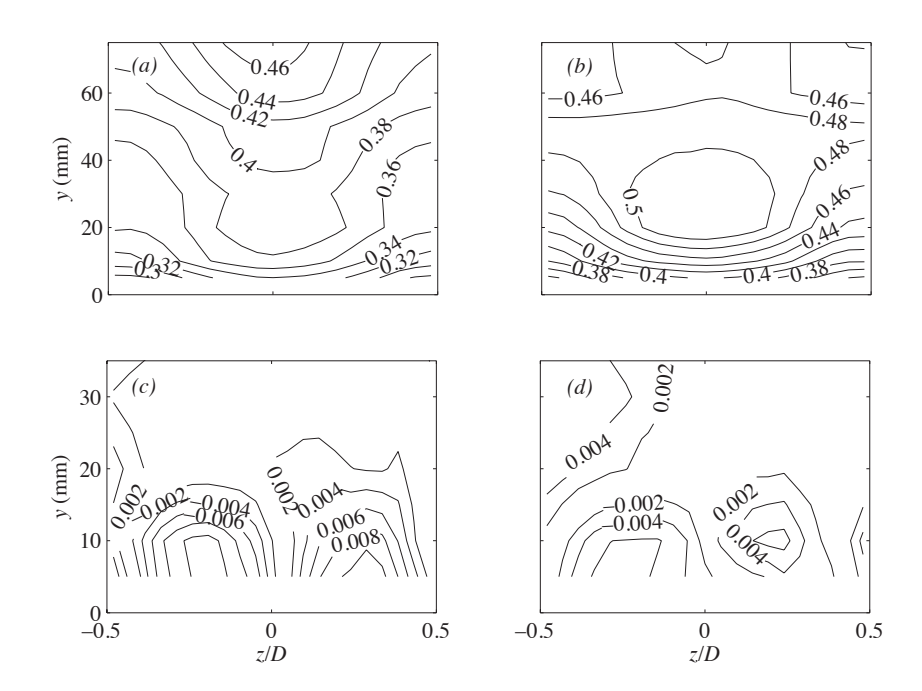


FIGURE 14. Contours of (a)  $U/U_{inl}$  at VR = 3, (b)  $U/U_{inl}$  at VR = 6, (c)  $W/U_{inl}$  at VR = 3 and (d)  $W/U_{inl}$  at VR = 6. All measurements are taken at  $x_h$ .

have a U-shape around z/D=0. The figure width is one period of the array and thus contains two vortices. At z/D=0.5 the vortices instead produce upflow and transport of low streamwise momentum from the wall. At  $x_h$  the cross-plane velocities of the vortices is quite low. Figure 14 (c) shows that the maximum spanwise velocity is  $W/U_{inl}\approx 0.008$ . In the figure only the spanwise components of the lower parts of the vortices are seen. This is because the spanwise velocity of the upper vortex half diffuses more rapidly as the vortices are convected downstream. In Lögdberg  $et\ al.\ (2008c)$  this is shown for vane-type VGs in a ZPG. There the spanwise velocity magnitude of the upper half of a vortex, in an array, is shown to be less than 25 % of the lower half velocity magnitude. This is in a measurement plane 1.17 m downstream of a VG array with  $\lambda=83$  mm.

If VR is increased to 6 the U distribution in the cross-plane changes as can be seen when comparing figures 14(a,b). The velocity increases near the wall, but a high speed streak, unconnected to the free stream, is also formed at z/D=0. A possible explanation is that initially strong vortices have created the U-shaped contours mentioned above but lost strength as they are convected

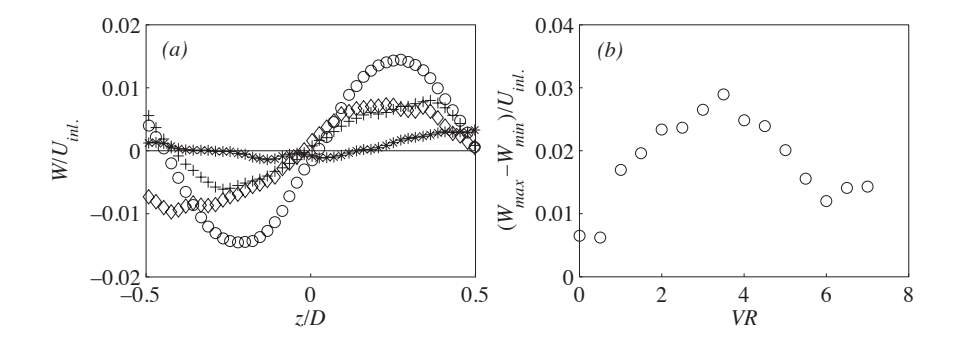


FIGURE 15. (a) W profiles at VR = 0.0 (\*), VR = 1.0 (\$\infty\$), VR = 3.5 (\$\infty\$) and VR = 6.5 (+). (b) The range of W for different VR.

downstream and thus causing the wall-normal transport of streamwise momentum to end. The circulation of the initially stronger vortices seems to decay faster. In figures 14 (c,d) the spanwise velocity magnitudes for the VR=6 configuration is lower than for VR=3.

In figure 15(a) profiles of W at y=5 mm are shown for some levels of VR. The amplitude at VR=3.5 is substantially larger than at VR=6.5. This agrees with the conclusions from figures 14 (c,d). Furthermore the contour plots show that the decrease in W is not due to lifting of the vortices at higher VRs. Figure 15(b) seems to confirm that no vortices are created at VR=0.5. When the jet velocity is increased to VR=1.0 there is a jump in the range of W, indicating that vortices now are present in the boundary layer. For VRs higher that 3.5 the W range decreases rapidly, implying that the circulation also decreases. Despite this  $\overline{U}_5$  in figure 11(b) continues to increase up to VR=5.0 and then falls off very slowly. Thus, even though the circulation is lower for higher VR at  $x_h$  the momentum transport is greater. This further augments the hypothesis above, that the vortices that the initially strongest vortices also experience the highest rate of decay.

Figures 16(a,b) show  $u_{rms}/U_{inl}$  for VR=3 and VR=6. For both cases the turbulence distribution is symmetrical and the average level is similar. Still the contours are very differently organised. In order to estimate quantitatively how VR affects  $u_{rms}$ , its mean value is calculated from the x-z planes at y=5 mm and plotted against VR in figure 17. Without control the turbulence intensity is approximately 6% in the separation bubble. At VR=0.5 no vortices are formed and the separated region is unaffected. When weak vortices are produced at VR=1.0 they tend to increase the turbulence level, in spite of the now attached flow. At higher jet velocities the turbulence intensity decreases as the flow become more organised.

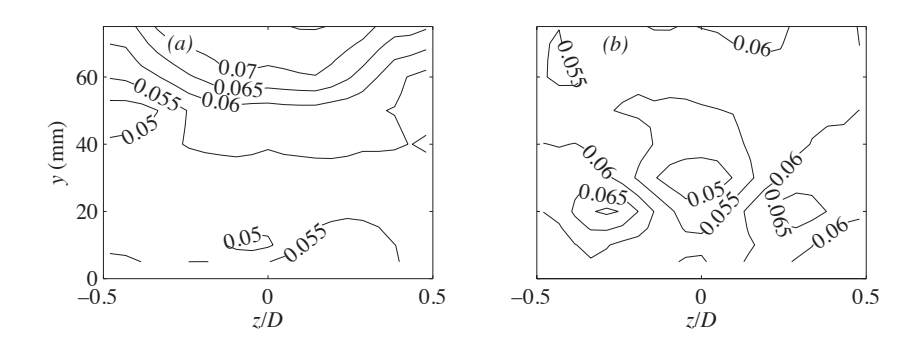


Figure 16. Contours of  $u_{rms}/U_{inl}$  at (a) VR = 3 and (b) VR = 6.

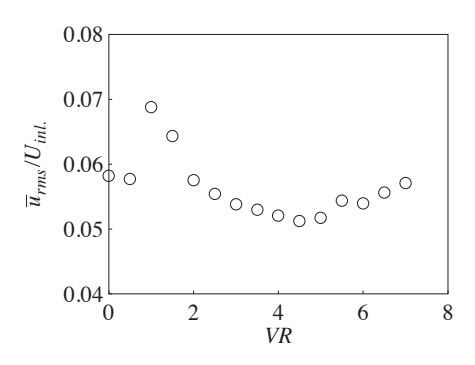
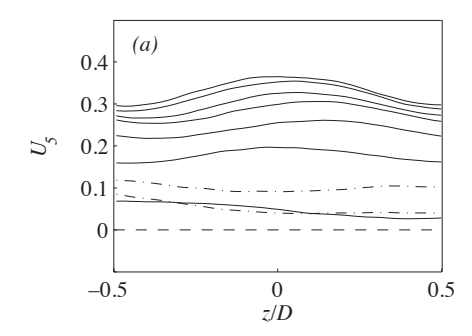


FIGURE 17. Mean  $u_{rms}$  at y = 5 mm for different levels of VR.

4.5c. Yaw. In many real life applications the mean flow direction is not constant. Thus, to be robust a flow control system must be able to function even at yawed flow conditions. Earlier experiments, by Lögdberg et al. (2008c), have shown that vane-type VG pairs, with the vanes set at  $\pm 15^{\circ}$ , produce the same level of circulation, independent of yaw angle, up to a yaw angle  $\theta = 20^{\circ}$ .

Since it is not feasible to yaw the flow in the wind tunnel, a study of the influence of yaw was made by yawing the VG-devices. This was done by turning the VGJ plugs. It would be more like in a real application if the whole array was yawed, but that was not practical. Furthermore, an advantage of the chosen configuration is that every VGJ will remain at the same streamwise position and thus act on the same boundary layer. Yaw measurements were performed for  $\theta = 0 - 90^{\circ}$  at VR = 3 and VR = 5, and the resulting  $U_5$  profiles are shown in figures 18(a, b). For VR = 3 the control effect is slowly decreasing



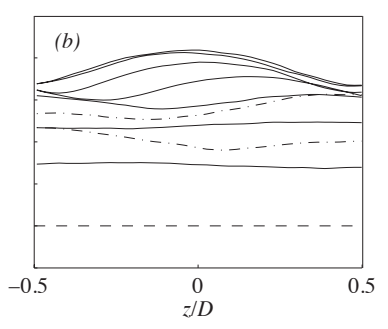


FIGURE 18. Velocity profiles at different yaw angles at (a) VR = 3 and (b) VR = 5. Full lines show yaw angles up to  $60^{\circ}$  and the dash-dotted lines show the yaw angles  $70^{\circ}$  and  $90^{\circ}$ . Thus for the full lines  $U_5$  decreases monotonically with increasing  $\theta$  but for the dash-dotted lines  $U_5$  is increasing with  $\theta$ .

as  $\theta$  is increasing. From  $0^{\circ}$  to  $40^{\circ}$  the velocity maximum is gradually moving in the yaw direction and the flow field seems to be qualitatively similar. At  $\theta=50^{\circ}$  the velocity maximum is back at z/D=0, possibly indicating the loss of one of the vortices in the counter-rotating pair. At  $\theta\geq 60^{\circ}$   $U_5$  is low, but increasing slightly after a minimum at  $\theta=60^{\circ}$ . This is more clearly seen on  $\overline{U}_5$  in figure 19. When the jet velocity is increased to VR=5 both  $U_5$  and  $\overline{U}_5$  increase, but their development with  $\theta$  seems similar to VR=3 up to  $\theta=60^{\circ}$ . Again there is a minimum, but when the angle is further increased the control effect increases rapidly. At  $\theta=90^{\circ}$   $\overline{U}_5$  is back on same level as at approximately  $\theta=45^{\circ}$  (interpolated).

4.5d. Geometry and velocity ratio. If it is necessary to increase the control effect either VR or the the number of jets can be increased. A comparison between the alternatives were made by turning off half the jets, while keeping the jet flow rate constant. First every second VGJ device were turned off to produce counter-rotating vortices with L=40 mm and  $\gamma=160$  mm. Then every second jet were turned off to produce co-rotating vortices with  $\gamma=80$  mm. Measurements were made at two flow rates:  $Q=Q_1$ , corresponding to VR=3 in the original configuration, and  $Q=Q_2$ , corresponding to VR=5 in the original configuration.

Figure 20(a) compare  $U_5$  profiles of the sparse counter-rotaing array and the original array. Obviously the amplitude increases when  $\lambda$  is doubled and the total flow rate is kept constant. Furthermore the distance between the  $U_5$  profiles is smaller for the sparse array. This is because the increase of  $\overline{U}_5$  with

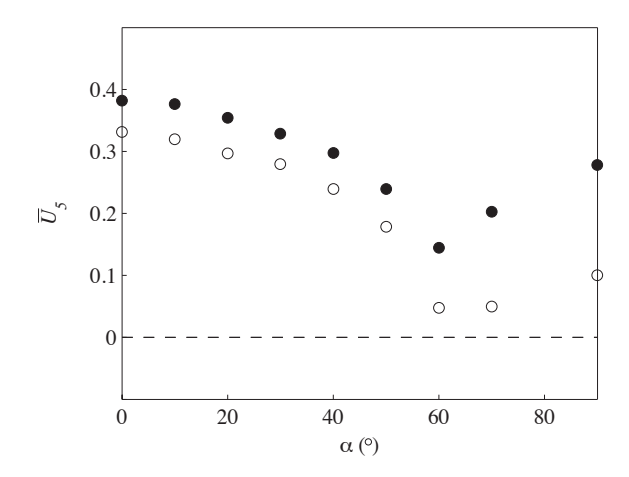


FIGURE 19. Effectiveness at different yaw angles. The open circles show VR=3 and the filled circles show VR=5.

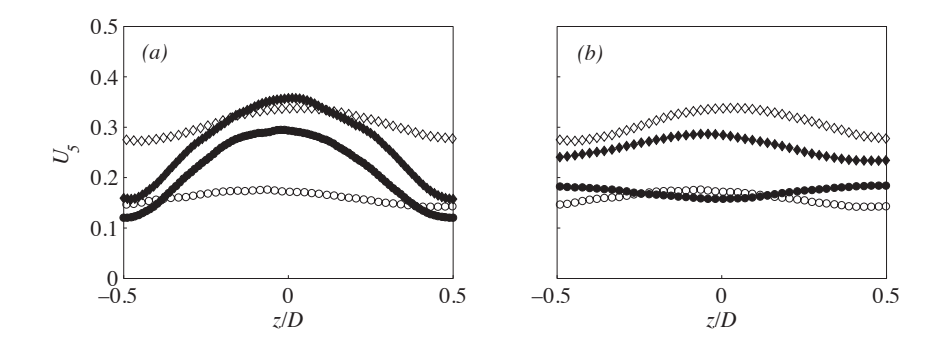


FIGURE 20. U profiles at y=5 mm. (a) The filled circle and diamond show velocities at VR=3 and 5, respectively, with every second VGJ device turned off. Open circles and diamonds show velocities for the standard configuration at VR=1.5 and 2.5, respectively. (b) Every second jet is turned off to produce co-rotating vortices. Symbols as in (a).

VR is smaller at this VR level. At the flow rate  $Q=Q_1$  the sparse array produces a highest control effect and at flow rate  $Q=Q_2$  the dense array is best. For both flow rates it is the configuration with a VR closest to the maximum  $\overline{U}_5/Q$  in figure 12 that produces the best result.

For the co-rotating configuration the result, shown in figure 20(b), is less clear. The co-rotating array is slightly better than the original at  $Q_1$  and the

original is better at  $Q_2$ , but the differences are smaller than in figure 20(a). Apparently the rate of change of  $\overline{U}_5$  with VR is different with co-rotating vortices. The spanwise variation of  $\overline{U}_5$  is smaller for the co-rotating vortices.

#### 5. Discussion

Jet vortex generators have been shown to be as effective as conventional vane-type VGs. Furthermore, there seems to be a maximum possible value of  $\overline{U}_5 \approx 0.4$ , that is common for both systems. This agrees with the results in Lögdberg et al. (2008c), where  $\overline{U}_{5,max}$  seems to approach an asymptotic value of 0.40–0.45, independent of APG, for  $\gamma_e > 3$ . For a ZPG turbulent boundary layer at the same x position and  $U_{inl}$ ,  $\overline{U}_5$  is 0.68. Since  $U_e = U_{inl}$  in ZPG,  $\overline{U}_5$  is recalculated for  $U_e$  at  $x_h$ . The new value of the symptotic value of  $\overline{U}_5$  is 0.6-0.65, which is close to that of the ZPG case.

A maximum in  $\overline{U}_5$  is reached at VR=5. Since the rate of increase of  $\overline{U}_5$  with VR is decreasing from VR>2.5, the maximum volume flow efficiency and the maximum kinetic energy efficiency is obtained at lower VRs. Their maxima is at  $VR\approx 2.0$  and VR=1.0, respectively.

The necessary VR to keep the flow attached varies little with APG. This is in line with the results by Lögdberg et~al.~(2008b), where a circulation of approximately  $\gamma_e=1.0-1.5$  was enough to eliminate separation in all three APG cases. In APG-4 VR=0.85 is enough to avoid separation. It is VR=1.0, when VR is based on  $U_e$ . This is similar to Johnston & Nishi (1990) in a comparable APG, where the separation bubble was eliminated at VR>0.86.

At yaw the control effect is decreasing slowly up to  $\theta=40^\circ$ , where it is still 70–80% of the non yawed level. Thus, the system robustness for yaw is good. If the jet velocity is adjusted for maximum volume flow efficiency, in this case VR=2.0, it is possible to keep  $\overline{U}_5$  constant up to  $\theta=45^\circ-50^\circ$  by increasing VR. At  $\theta>60^\circ$   $\overline{U}_5$  is increasing again. The performance difference between high and low VR increases at  $\theta>60^\circ$ . In this  $\theta$  region the flow field changes qualitatively. At a yaw angle of the plug  $\theta=90^\circ$ , the two jets are directed such that  $\beta$  is  $0^\circ$  and  $180^\circ$ . According to Compton & Johnston (1992) and many others each jet then produces a pair of weak counter-rotating vortices. Here, however, the control effect at  $\beta=[0^\circ, 180^\circ]$  is quite strong for VR=5.

When VR is in the maximum efficiency range and more control is needed, the VGJ array should, if possible, be made denser instead of increasing VR. Similarly, to reduce control the VGJ array is made more sparse. Obviously,  $\lambda$  has to be within a certain range for the VGJs to continue to be effective.

In the second part of this study (Lögdberg (2008)) pulsed VGJs are studied and the influence of VR, frequency and duty cycle on their effectiveness is thoroughly investigated.

# Acknowledgements

This work is part of a cooperative research program between KTH and Scania CV. The author would like to thank Prof. Henrik Alfredsson for valuable comments and ideas.

# References

- Angele, K. P. & Muhammad-Klingmann, B. 2005a The effect of streamwise vortices on the turbulence structure of a separating boundary layer. *Eur. J. Mech.* B **24**, 539–554.
- Angele, K. P. & Muhammad-Klingmann, B. 2005b A simple model for the effect of peak-locking on the accuracy of boundary layer statistics in digital PIV. *Exp. Fluids* **38**, 341–347.
- COMPTON, D. & JOHNSTON, J. 1992 Streamwise vortex production by pitched and skewed jets in a turbulent boundary layer. AIAA J. 30, 640–647.
- GODARD, G. & STANISLAS, M. 2006 Control of a decelerating boundary layer. part 3: Optimization of round jets vortex generators. *Aerosp. Sci. Tech* 10, 455–464.
- Johnston, J. 1999 Pitched and skewed vortex generator jets for control of turbulent boundary layer separation: a review. In *The 3rd ASME/JSME joint fluids engineering conference*.
- JOHNSTON, J., MOISER, B. & KHAN, Z. 2002 Vortex generating jets; effects of jethole inlet geometry. Int. J. Heat Fluid Flow 23, 744–749.
- JOHNSTON, J. & NISHI, M. 1990 Vortex generator jets, means for flow separation control. AIAA J. 28, 989–994.
- Keane, R. & Adrian, R. 1992 Theory of cross-correlation in PIV. Appl. Sci. Research 49, 191–215.
- Kelso, R. M., Lim, T. T. & Perry, A. E. 1996 An experimental study of round jets in cross-flow. *J. Fluid Mech* **306**, 111–144.
- Khan, Z. U. & Johnston, J. 2000 On vortex generating jets. Int. J. Heat Fluid Flow  ${\bf 21},\,506{-}511.$
- Lim, T. T., New, T. H. & Luo, S. C. 2001 On the development of large-scale structures of a jet normal to a cross flow. *Phys. Fluids* **13**, 770–775.
- LINDGREN, B. & JOHANSSON, A. V. 2004 Evaluation of a new wind-tunnel with expanding corners. *Exp. Fluids* **36**, 197–203.
- LÖGDBERG, O. 2008 Separation control by an array of vortex generator jets. Part 2. Pulsed jet. Paper 5 in the present thesis.
- LÖGDBERG, O., ANGELE, K. & ALFREDSSON, P. H. 2008a On the scaling of turbulent separating boundary layers. *Phys. Fluids* **20** 075104.

- LÖGDBERG, O., ANGELE, K. & HENRIKSSON, P. H. 2008b On the robustness of separation control by streamwise vortices. Paper 3 in the present thesis.
- LÖGDBERG, O., FRANSSON, J. & ALFREDSSON, P. 2008c Streamwise evolution of longitudinal vortices in a turbulent boundary layer. J. Fluid Mech. (in press).
- MILANOVIC, I. & ZAMAN, K. 2004 Fluid dynamics of highly pitched and yawed jets in crossflow. AIAA J. 42 (5), 874–882.
- RAFFEL, M., WILLERT, J. & KOMPENHANS, J. 1997 Particle Image Velocimetry. A practical guide. Springer-Verlag.
- RIXON, S. G. & JOHARI, H. 2003 Development of a steady vortex generator jet in a turbulent boundary layer. *J. Fluids Eng.* **125**, 1006–1015.
- Selby, G., Lin, J. & Howard, F. 1992 Control of low-speed turbulent separated flow using jet vortex generators. *Exp. Fluids* **12**, 394–400.
- Wallis, R. 1952 The use of air jets for boundary layer control. Aero note 110. Aerodynamics Research Laboratories, Australia.
- ZHANG, H.-L., ZHANG, X. & HURST, D. 1996 An LDA study of longitudinal vortices embedded in a turbulent boundary layer. In 8th Int. Symp. App. Laser Tech. Fluid Mech..
- Zhang, X. 2000 An inclined rectangular jet in a turbulent boundary layer-vortex flow. Exp. Fluids 28, 344-354.
- Zhang, X. 2003 The evolution of co-rotating vortices in a canonical boundary layer with inclined jets. *Phys. Fluids* **15**, 3693–3702.

Paper 5

# Separation control by an array of vortex generator jets. Part 2. Pulsed jets.

By O. Lögdberg<sup>1,2</sup>

<sup>1</sup>Linné Flow Centre, KTH Mechanics, S-100 44 Stockholm, Sweden
<sup>2</sup>Scania CV AB, S-151 87 Södertalje, Sweden

The effect of longitudinal vortices produced by an array of steady jets on a separation bubble was examined experimentally. In the experiment an adverse pressure gradient causes the turbulent boundary layer on a flat plate to separate. The jets are originating from orifices in the wall and are directed  $45^{\circ}$  from the wall and  $90^{\circ}$  from the mean flow direction. In the centre of the separated region, particle image velocimetry (PIV) is used to measure the momentum increase near the wall that the vortices produce. The geometry was fixed, but the ratio of jet velocity  $U_{jet}$  to the free stream velocity, the pulsing frequency and the duty cycle were varied. It was shown that to achieve maximum control effect the injected mass flow should be as large as possible, within an optimal range of jet velocity ratios. For a given injected mass flow the important parameter was shown to be the injection time  $t_1$ . A non-dimensional injection time is defined as  $t_1^+ = t_1 U_{jet}/d$ , where d is the jet orifice diameter. Here, the optimal  $t_1^+$  was in the range 100-200.

#### 1. Introduction

Control of separation of boundary layer flows can be achieved through different approaches. One common method, that has proved to be effective, is to introduce longitudinal vortices in the boundary layer. The vortices enhance mixing and transport high momentum flow towards the wall. In the past, the vortices have been produced by vane-type vortex generators, *i.e.* short wings attached to the surface with the wingspan in the wall normal direction and set at an angle towards the mean flow direction. An alternative way of producing the vortices is by jets originating from the wall. Lately several studies have been devoted to research on vortex generator jets (VGJs). This study of VGJs is divided into two parts. Part 1 (Lögdberg (2008)) discusses steady jets and part 2 deals with pulsed jets. The geometry parameters of a VGJ system are defined in figure 1.

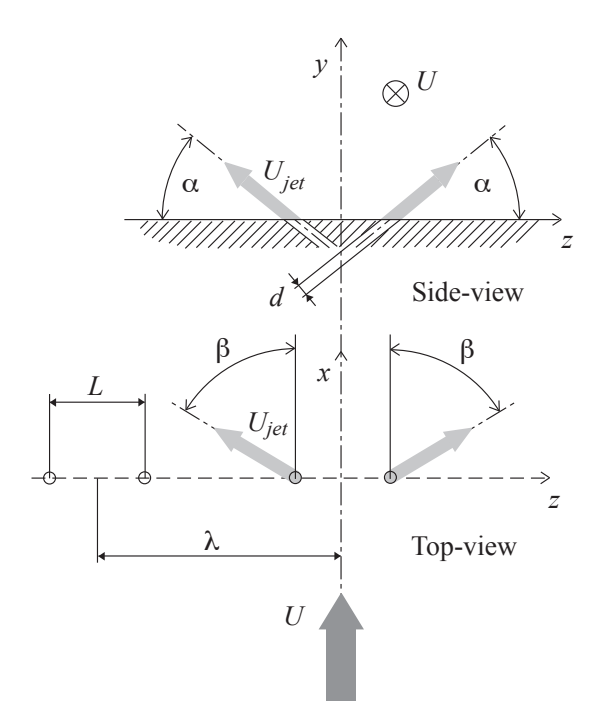


FIGURE 1. Schematic of a VGJ device producing counterrotating vortices. Note that the figure is in first-angle projection. U is the free stream and  $U_{jet}$  is the jet velocity. The direction of the jet is defined by the pitch angle  $\alpha$  and the skew angle  $\beta$ . The jet exit diameter is d, the distance between the jets of a VGJ pair L and the distance between the pairs in an array  $\lambda$ .

# 1.1. Background

The flow control effect of pulsed VGJs can be due to several different physical mechanisms. In a laminar boundary layer they can cause transition to turbulence and thereby delay separation. They can influence the flow by amplifying natural frequencies in the boundary layer, like the shedding of a stalled airfoil. Furthermore, they can function like steady VGJs and produce longitudinal vortices that transport high momentum fluid towards the wall. In the experiment presented in this study the effect of pulsed VGJs of the last category is investigated. Consequently, this introductory reveiw also focus on this type of pulsed VGJs.

1.1a. Previous research. The first experiments on pulsed VGJs were performed by McManus et al. (1994). They demonstrated a significant performance improvement in controlling separation on a ramp when a short (3 jets) spanwise array of VGJs was pulsed. Later McManus et al. (1995) and McManus et al. (1996) successfully applied 1–2 pulsed VGJs on a two-element flat airfoil model. In these experiments force and pressure measurements were performed together with some flow visualisations.

Johari & Rixon (2003) and Tillmann  $et\ al.$  (2003) used LDV to measure the vorticity in cross-planes downstream of single pulsed VGJs in zero pressure gradient boundary layers. Johari & Rixon (2003) studied the vorticity field evolution in time and also the downstream development of vorticity and circulation. Tillmann  $et\ al.$  (2003) varied the frequency (f) and the velocity ratio (VR) to measure how the circulation and the vortex paths develop downstream of the VGJ.

Recently the research group at the Technical University of Braunschweig has contributed with a series of investigations on steady and pulsed VGJs. Ortmanns *et al.* (2006) used stereoscopic PIV to study the vortex structures produced by a skewed slot pulsed VGJ. Scholz *et al.* (2008) equipped an airfoil with an array of skewed slot vortex generators and studied the effect of frequency and duty cycle on the pressure profile.

Also the group at Laboratorie de Mécanique de Lille has extended their studies of vane-type VGs and steady VGJs in an adverse pressure gradient to pulsed VGJs in Kostas *et al.* (2007).

1.1b. The main parameters. If the VGJ geometry is fixed, there are three main parameters that decide the performance of a pulsed VGJ. These are the ratio between the jet velocity and the free stream velocity VR, the pulsing frequency f and the duty cycle  $\Omega$ . The duty cycle is defined as the ratio between the injection time  $(t_1)$  and the period of the pulse (T).

For steady VGJs the generated circulation strongly depends on VR and, the same statement can be made also for pulsed VGJs. This has been shown for arrays of VGJs by McManus  $et\ al.\ (1995)$  and Kostas  $et\ al.\ (2007)$ . Also similar to steady jets is the occurrence of a circulation optimum in VR above which the vortex is translated out of the boundary layer. Outside the boundary layer the vortex quickly dissipates. Tillmann  $et\ al.\ (2003)$  have demonstrated this for a single pulsed VGJ in a zero pressure gradient (ZPG) boundary layer.

The effect of the pulsing frequency is still not completely understood. In McManus et al. (1995) and Scholz et al. (2008) the frequency had little effect on lift and drag, but in McManus et al. (1996) the magnitude of the upper side suction peak on the airfoil was strongly dependent on the pulsing frequency. The optimum frequency Strouhal number was found to be of the same order as that characterizing the natural eddy shedding behind blunt objects. Tillmann et al. (2003) reported a significant variation in circulation due to the frequency.

The frequency can be normalised by the jet diameter d and the jet velocity  $U_{jet}$  to produce a Strouhal number  $St_{jet} = fd/U_{jet}$ . When there are dominant length scales in the flow, like for example the chord of a wing, they can be used together with the free stream velocity to normalise the frequency. Thus there can be optima related both to the VGJs and to the flow field that is to be controlled.

The duty cycle was shown by Scholz et al. (2008) to be of major importance in increasing post-stall lift on an airfoil. They found  $\Omega \leq 0.25$  to be most beneficial. Bons et al. (2001) reported experiments on pulsed vortex generators in a laminar boundary layer that were effective at duty cycles as low as 0.01. However, the authors point out that this would change in a turbulent boundary layer. In the study by Kostas et al. (2007) the wall shear stress increases nearly linearly with increasing  $\Omega$ .

Johari & Rixon (2003) suggested that the maximum jet penetration determines the maximum circulation produced by a pulsed VGJ. Furthermore, they proposed that it is the jet starting vortex ring that is crucial to increase penetration. Gharib  $et\ al.\ (1998)$  showed that only the first 4d of injected fluid contributed to the starting vortex. Hence, the injection time should be of such length that only a fluid cylinder that is 4d long is injected. Based on their data and the results of Gharib  $et\ al.\ (1998)$ , Johari & Rixon (2003) suggested that the optimum injection time is  $4-8\ d/U_{jet}$ 

Synthetic jets are very attractive since they require no air supply and thus make the installation of a flow control system much simpler. Since a synthetic jet has little influence on the boundary layer during its suction phase their flow control mechanism is the same as for non-synthetic jets. In recent years research has been done, both on actuator development and on their use for flow control. One example is the investigation by Amitay et al. (2001).

#### 1.2. Present experiment

The experiments described here is a continuation of the investigations performed in part 1 of this study (Lögdberg (2008)). The experiment is designed to allow a large parameter range to be studied. The wind tunnel test-section and the measurement technique is the same as in part 1 and the reader is referred to that paper for details. In chapter 2 the new pulsating set-up is described and the jet characteristics are presented in some detail. As mentioned above, there are three parameters that can be varied for a given geometrical set-up and the flow control effectiveness for various combinations of these parameters is thoroughly studied in chapter 3. Finally the results are discussed in chapter 4.

TABLE 1. The main features of the VGJ system of the present experiment.  $\alpha$ ,  $\beta$ , d, L and  $\lambda$  are defined in figure 1.  $\delta$  is the boundary layer thickness at the streamwise position of the VGJ array,  $n_{jet}$  is the number of jets in the array, VR is the range of jet velocity ratios and  $\Delta x_{sep}$  is the distance from the VGJs to the separation point.

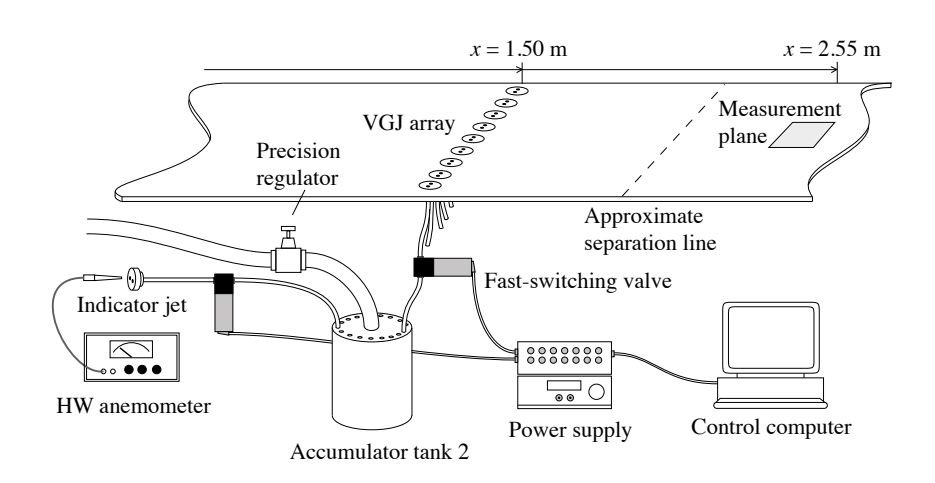


FIGURE 2. Schematic of VGJ setup.

# 2. Pulsating jet

#### 2.1. Experimental set up

The geometry of the VGJ array is the same as in part 1 of this study, and the various parameters are listed in table 1. However, the installation of the VGJs is extended to enable pulsing of the jets. In figure 2 the set-up is shown. Between accumulator tank 2 and the VGJ plugs fast-switching Festo MHE2 solenoid valves, that can be seen in figure 3, are applied. The valves are connected to a 30 A power supply through a 20 channel amplifier that is controlled from a computer. The system is designed to make it possible to control each valve individually, although this feature was not used in the present experiment. The tubing has an inner diameter of 4 mm and the length from the valve to the VGJ device is 0.6 m to make it possible to mount the valves outside the test-section.

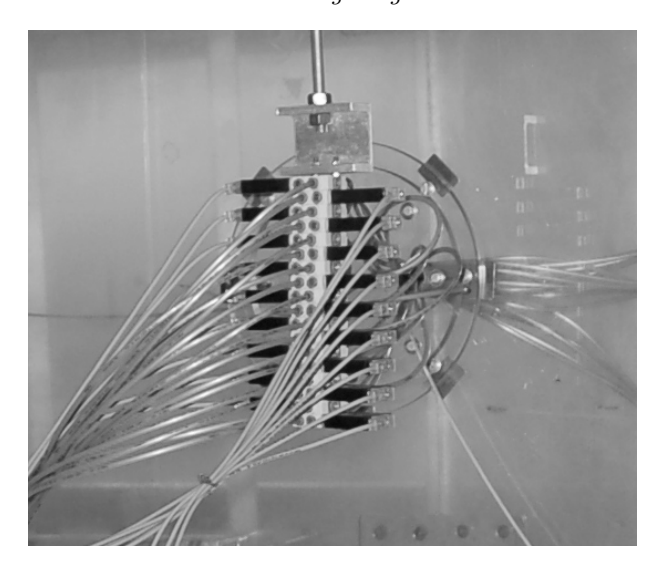


FIGURE 3. The 18 Festo MHE2 valves are located outside the wind-tunnel test-section. Behind the valves there is a hole in the Plexiglas, through which the tubing are lead into the wind-tunnel. The alternating mounting is to improve cooling of the valves.

A test of different tubing lengths between the valves and the jet device showed that the leakage flow when the valve is closed increases with tubing length, but at 0.6 m its impulse is negligible compared to the primary pulse.

One VGJ plug is placed outside the test-section with identical tubing length, to facilitate hot wire measurements of the jet. This is necessary in order to adjust  $\Omega$  and  $VR^1$  while setting up of the configuration. VR is also monitored during the PIV measurements.

### 2.2. Characterization of the jets

In figure 4 a typical jet pulse train ( $VR=3,\,f=100$  Hz and  $\Omega=0.5$ ) is shown. The velocity  $U_{CL}$  is measured at the jet centreline 1 mm from the orifice and the figure is obtained by averaging 30 individual pulse trains. The nominal injection velocity  $U_{jet}$  is the average of the pulse plateau. T is the period time and  $t_1$  is the injection time, defined as the pulse width at  $U_{CL}=0.5U_{jet}$ . Thus  $\Omega=t_1/T$ . There is a leakage flow when the valve is closed, this is due to the fact that when the valve closes the high pressure side, it opens towards the

 $<sup>^1</sup>VR$  is defined as  $VR = U_{jet}/U_{inl}$ , where the test-section inlet velocity  $U_{inl} = 26.5$  m/s. To obtain a VR based on the freestream velocity ( $U_e = 22.0$  m/s) at the position of the VGJ array, the reported VR numbers are to be multiplied by  $26.5/22.0 \approx 1.20$ .

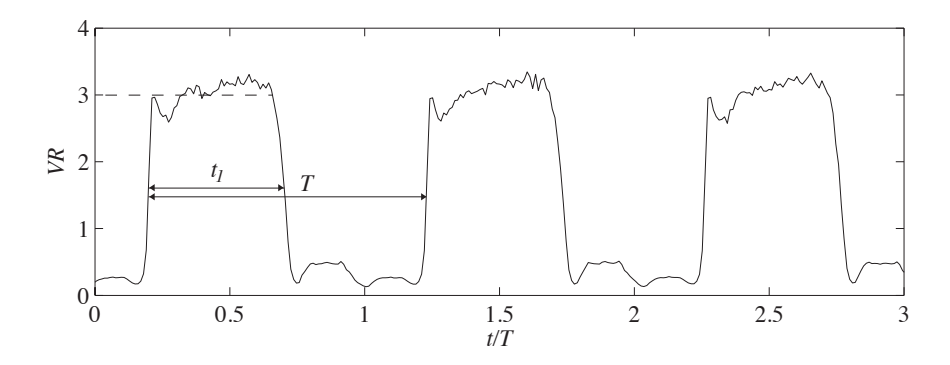


FIGURE 4. Jet pulses at VR = 3 and f = 100 Hz. The data is averaged over 30 cycles.

atmosphere and a small flow enters the test-section through the jet orifice. The volume and impulse of the leakage flow are however low.

To study how the velocity profile is affected when the jet is pulsed, transient profiles of the same configuration as in figure 4 have been measured. The jet velocity was phase averaged at 27 radial positions. At each position 200 jet pulses were measured. The pulsed velocity profile maintains the asymmetric shape of the steady jet as can be seen in figure 5. At its maximum velocity the shape of the pulsed jet shows complete similarity with the steady jet, but also when the velocity is increasing the same asymmetry is shown. However, at the beginning of the pulse the profile is inversely asymmetric.

The shape of the maximum jet profile remains similar to the steady jet at frequencies from 25 Hz up to 400 Hz. In figure 6 this is shown for VR=3. In the same figure profiles at VR=1 and VR=5 are also shown to be similar, although Bremhorst & Harch (1979) studied pulsating jets and concluded that the velocity profile changes with frequency.

According to the specifications of the Festo valves, the maximum switching frequency is 330 Hz, but when the valves were tested it was not until  $f\approx 650-700$  Hz that the valve stopped closing. It was possible to generate acceptable pulses up to 500 Hz, but in this experiment the maximum frequency was chosen to 400 Hz. In figure 7(a) the change of the pulse shape with frequency is shown. At frequencies below 100 Hz the pulse is close to a square wave, but at  $f\geq 100$  Hz the flanks start to become less steep, when scaled with the period time. Note that with the chosen definition of  $t_1$  the kinetic energy of the pulses decreases with frequency, while the volume flow remains approximately constant.

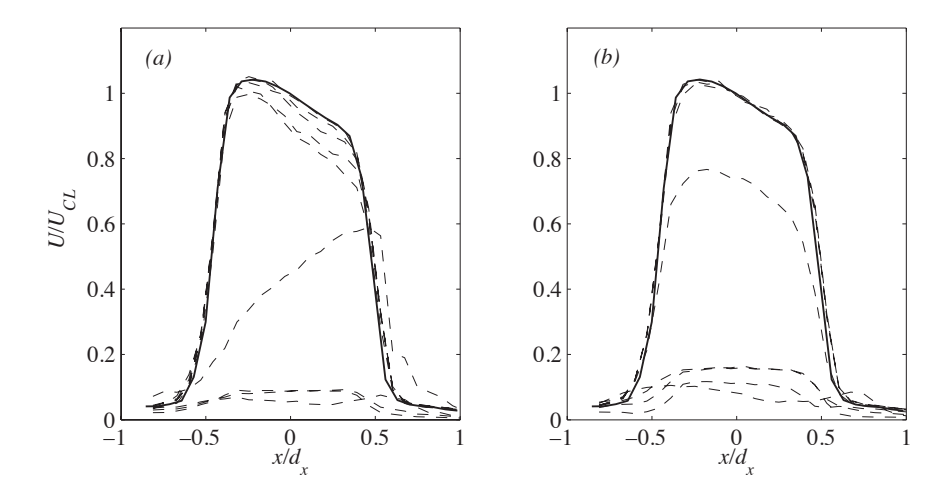


FIGURE 5. Transient velocity profiles at f = 100 Hz and VR = 3. The time step between consecutive profiles are 0.65 ms. In (a) the jet changes from low state to high and in (b) it is the opposite. The full line shows a steady jet profile.

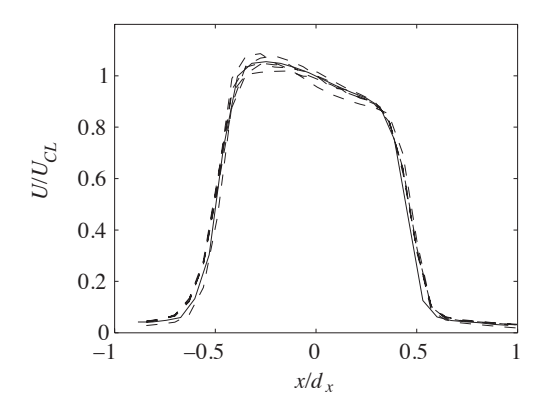
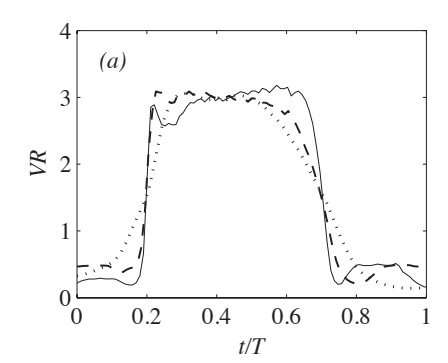


FIGURE 6. The dashed lines show maximum velocity profiles for  $f=25,\,100$  and 400 Hz at VR=3 and VR=1 and 5 at f=100 Hz. The full line shows a steady jet profile.

In figure 7(b) pulses of five different values of  $\Omega$  are shown. The shortest pulse shown has a duty cycle of just 0.05, but that is less than the minimum  $\Omega$  in the control experiments.



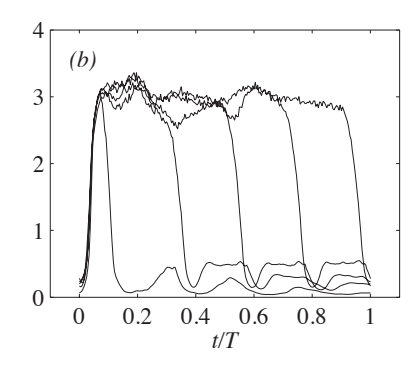


FIGURE 7. (a) Pulses at VR=3 averaged over 100 cycles. Full line is f=100 Hz, dashed line is f=200 Hz and dotted line is f=400 Hz. (b) Pulses of  $\Omega=0.05,\,0.30,\,0.50,\,0.70$  and 0.90 at VR=3, averaged over 40 cycles..

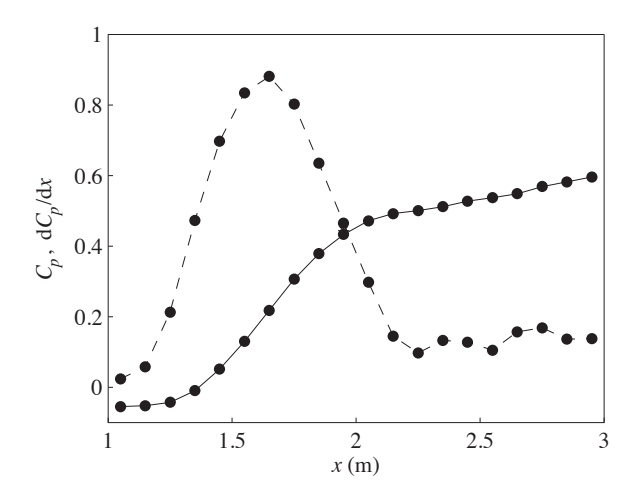


FIGURE 8. The pressure gradient in the test-section. The dashed line show  $C_p$  and the full line show  $\mathrm{d}C_p/\mathrm{d}x$ .

# 3. Separation control

The adverse pressure gradient along the test section flat plate is shown in figure 8. It is identical to APG-4 in the first part of this study and the maximum value of  $\mathrm{d}C_p/\mathrm{d}x$  is 0.88. This causes the turbulent boundary layer to separate at  $x\approx 2.1$  m. The two-dimensionality of the flow around the test plate centreline has been investigated for similar flow cases in the same set-up and was found

Table 2. The parameter range for the pulsed VGJs. In the position indicating a combination of f and  $\Omega$  the tested VRs are given. The configuration marked with  $\dagger$  has been run at yaw angles  $\theta=0^{\circ},10^{\circ},20^{\circ},30^{\circ},40^{\circ},50^{\circ},60^{\circ},70^{\circ}$  and  $90^{\circ}$ . Configurations marked with \* have also been measured in the x-y plane at z=0.

f				Ω			
	0.08	0.15	0.325	0.5	0.675	0.85	1.00
400	-	-	-	1,2,3	-	-	-
260	-	-	-	4	-	-	-
200	-	3	3	$1,2,3^*,4$	3	3	-
100	-	3	3	$1,2,3^{\dagger *},4,5$	3	3	-
50	3	1,2,3,4	1,2,3,4	$1,2,3^*,4,5$	1,2,3,4	1,2,3,4	-
25	-	3	3	$1,2,3^*,4,5$	3	3	-
12.5	-	3	3	1,2,3,4,5	3	3	-
Steady	-	-	-	-	-	-	1:0.5:7

to be adequate. All PIV measurements are taken with the centre of the image at x=2.55 m, which is the approximate position of the maximum backflow in separation bubble. The measurement plane is  $120\times120$  mm, parallel to the plate at y=5 mm. The thickness of the laser sheet is approximately 1.5 mm.

The effect measure used is  $\overline{U}_5$ , which is the streamwise velocity normalised by  $U_{inl}$  and averaged over the measurement plane. The motivation behind the chosen measure of merit is given in part 1. In the uncontrolled case  $\overline{U}_5 = -0.075$ .

#### 3.1. Velocity ratio and frequency

In a first series of experiments VR and f was varied with  $\Omega$  held constant at 0.5. The mid column ( $\Omega=0.5$ ) of table 2 lists the tested configurations. As mentioned above, the maximum frequency of this experiment is 400 Hz. The minimum frequency is chosen to 12.5 Hz with  $\Delta f$  doubling for each step in f. Using suitable length and velocity scales the frequency can be reduced to a Strouhal number of fL/U. Here a Strouhal number based on the jet diameter and velocity  $St_{jet} = fd/U_{jet}$  will be applied and the range of  $St_{jet}$  is  $0.24-38\cdot 10^{-3}$ .

 $<sup>^2</sup>$ In experiments with pulsed VGJs on airfoils the chord is normally used as length scale. Sometimes boundary layer scales are used to produce  $St_{BL}=f\delta/U_e$ .

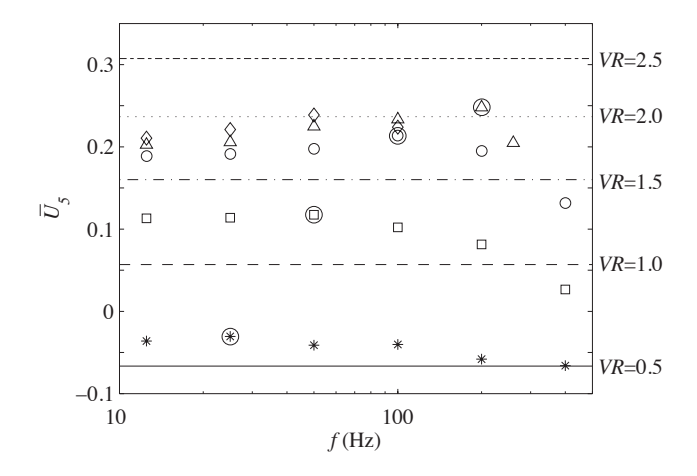


FIGURE 9.  $\overline{U}_5$  vs f at  $VR^*=0.5$  (\*),  $VR^*=1.0$  ( $\square$ ),  $VR^*=1.5$  ( $\circ$ ),  $VR^*=2.0$  ( $\triangle$ ) and  $VR^*=2.5$  ( $\diamond$ ). The maximum  $\overline{U}_5$  for each  $VR^*$ , except  $VR^*=2.5$ , are circumscribed. The horizontal lines indicate  $\overline{U}_5$  for steady jets, with the corresponding VR shown to the right. For all measurements  $\Omega=0.5$ .

Figure 9 summarises the results for  $\Omega=0.5$ . The pulsed jet is run at VR=1, 2, 3, 4 and 5. An effective VR is defined as  $VR^*=\Omega VR$ . Note that for a given  $U_{inl}, VR^*\sim Q$ , where Q is the volume flow. Since  $\Omega=0.5$ , the corresponding  $VR^*$  of the pulsed jet is  $VR^*=0.5, 1.0, 1.5, 2.0$  and 2.5. The control effect of the corresponding steady jet configurations is indicated with horisontal lines in the figure.

At VR=1 the control effect of the pulsed jet is better than the comparable steady jet of VR=0.5 at all frequencies up to 200 Hz and there is a weak maximum of  $\overline{U}_5$  at 25 Hz. At 400 Hz  $\overline{U}_5$  is equal for both cases. However, at no frequency separation is prevented. When VR is increased to 2,  $\overline{U}_5$  is positive at all studied frequencies, but at the highest frequency the pulsed jet is less effective than the steady jet. The limit seems to be at  $f\approx 300$  Hz. At this VR the maximum effect occurs at f=50 Hz. For VR=3 the variation with frequency is approximately the same, except that the maximum is at f=100 Hz. As for the steady jets (see figure 10(a)) the increase of  $\overline{U}_5$  with VR is small when VR>3. This can be seen for VR=4 and VR=5 in figure 9. Due to the smaller rate of increase in  $\overline{U}_5$  it is only at its maximum effectiveness at f=200 Hz that the pulsed VGJ at VR=4 is superior to the comparable steady jet. At VR=5 the result is much worse for the pulsed VGJ compared to the steady VGJ at VR=2.5. The maximum possible pulsing frequency at



# O. Lögdberg

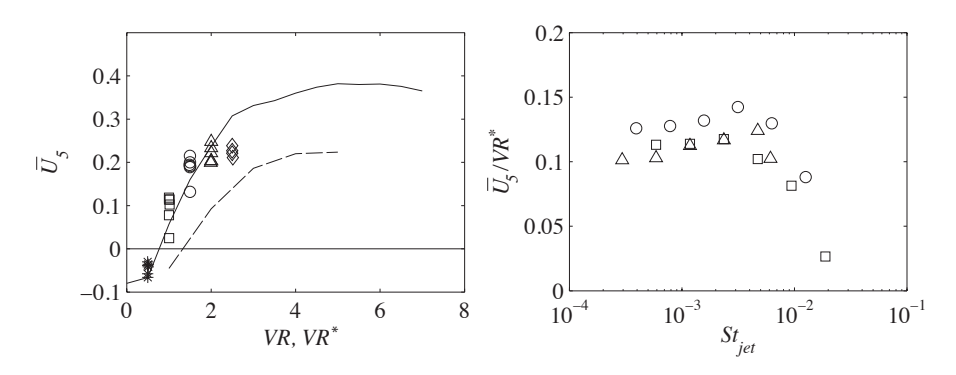


FIGURE 10. (a)  $\overline{U}_5$  vs VR and  $VR^*$ . The full line show steady jet results, the dashed line show average pulsed jet results and the symbols indicate  $\overline{U}_5$  vs  $VR^*$ . (b)  $\overline{U}_5/VR^*$  vs  $St_{jet}$  at  $VR^*=1.0, 1.5$  and 2.0. The data and the symbols are the same as in figure 9.

VR=4 is 260 Hz and at VR=5 it is less than 200 Hz. This is due to the small diameter of the tubing.

In figure 10(a) the control effect variation with VR is compared for steady and pulsed jets. The two lines show that the rate of increase of  $\overline{U}_5$  decreases at  $VR \approx 2.5-3$  for both configurations. The symbols show the data points from figure 9 plotted against  $VR^*$ . When the pulsed data is compensated for the lower flow by using  $VR^*$  the control effect is similar to that of the steady jets. It is also obvious that the VR is more important than the frequency. Furthermore, the range of  $\overline{U}_5$  variation with frequency seems to be larger when the growth of  $\overline{U}_5$  with VR is large.

It was shown above that the optimum frequency changes with VR. If, instead, the control effect is plotted against the jet based Strouhal number  $St_{jet}$ , the optimum is nearly independent of VR, as can be seen in figure 10(b).  $\overline{U}_5$  is normalised by the volume flow Q to reduce the control effect range. A frequency corresponding to  $St_{jet} \approx 4 \cdot 10^{-3}$  produces the maximum effect for VR = 2 - 4.

#### 3.2. Duty cycle and frequency

To study the correlation between the frequency and the duty cycle, these parameters were varied at a constant VR=3. The levels were  $\Omega=0,\,0.15,\,0.325,\,0.5,\,0.675,\,0.85$  and 1, and  $f=12.5,\,25,\,50,\,100$  and 200 Hz. In figure 11(a) the resulting  $\overline{U}_5$  is shown. If the effect of changing the duty cycle is a linear pulsewidth modulation of  $VR,\,\Omega=0$  and  $\Omega=1$  ( $\Omega VR=3$ ) would be connected with a straigth line. This is the dashed line in the figure. This assumption requires that  $\overline{U}_5$  is linear with VR and the dashed line in figure 10 shows that

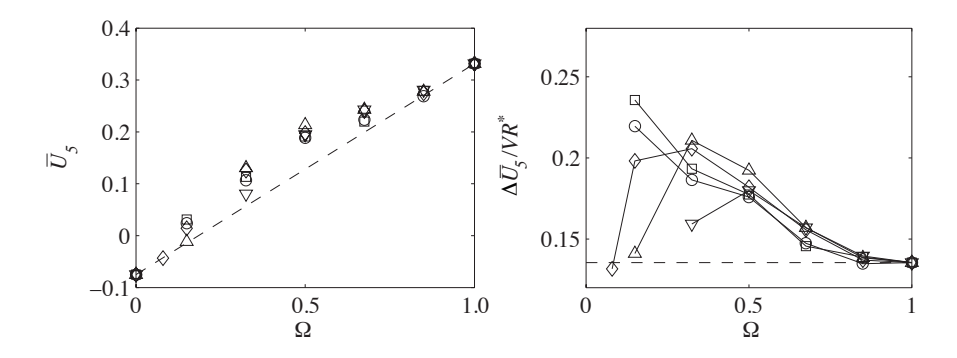


FIGURE 11. (a)  $\overline{U}_5$  vs  $\Omega$  for f=12.5 Hz ( $\circ$ ), f=25 Hz ( $\square$ ), f=50 Hz ( $\diamond$ ), f=100 Hz ( $\triangle$ ) and f=200 Hz ( $\nabla$ ) at VR=3. The dashed line linearly connects  $\overline{U}_5$  ( $\Omega=0$ ) and  $\overline{U}_5$  ( $\Omega=1$ ). (b)  $\Delta \overline{U}_5/VR^*$  vs  $\Omega$  for the same data as in (a).

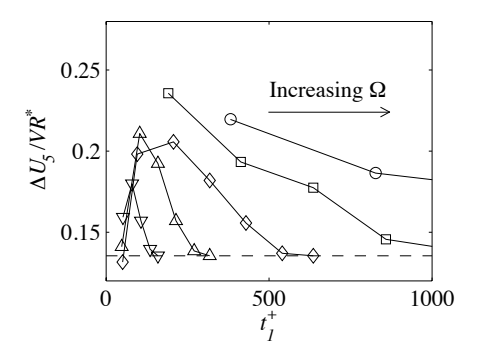


FIGURE 12.  $\Delta \overline{U}_5/VR^*$  vs  $t_1^+$  for the same data as in figure 11.

this is nearly the case for VR < 3. Since the data points for  $0.08 < \Omega < 0.85$  show better effect than the dashed line, there is a positive effect of the pulsing.

In order to study whether there is an optimum volume efficiency duty cycle, the control effect is recalculated as  $\Delta \overline{U}_5/VR^*$ .  $\Delta \overline{U}_5$  is the difference between the measured  $\overline{U}_5$  and the uncontrolled  $\overline{U}_5$ . In figure 11(b) the optimum  $\Omega$  is increasing with frequency. Thus, as proposed by Johari & Rixon (2003) the injection time  $t_1$  may be a more relevant parameter to chraracterize the pulsing. A non-dimensional injection time is defined as  $t_1^+ = t_1 U_{jet}/d$ . The variation of the control efficiency  $\Delta \overline{U}_5/VR^*$  with  $t_1^+$  is shown in figure 12. There seems to be a maximum at  $t_1^+ = 100 - 200$ , even though the two lowest frequencies never reached short enough injection times to be in that region. In figure 10(b)



# O. Lögdberg

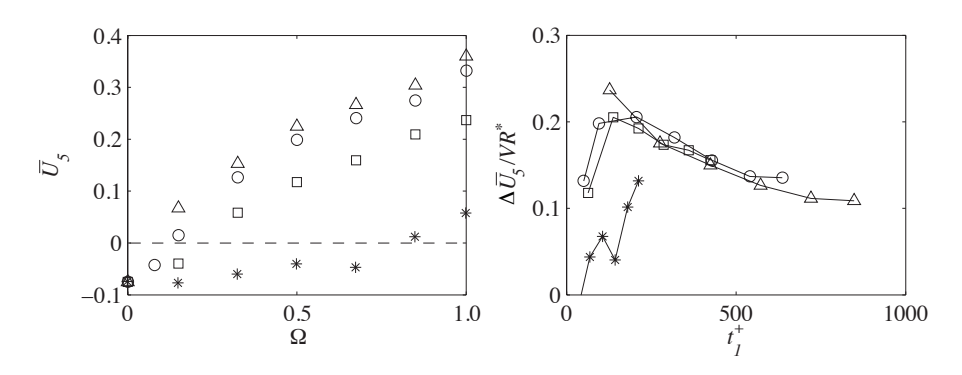


FIGURE 13. (a)  $\overline{U}_5$  vs  $\Omega$  at f=50 Hz, for VR=1 (\*), VR=2 ( $\square$ ), VR=3 ( $\circ$ ) and VR=4 ( $\triangle$ ). (b)  $\Delta \overline{U}_5/VR^*$  vs  $t_1^+$  for the same data as in (a).

the optimum  $St_{jet}$  was  $4\cdot 10^{-3}$  and since  $t_1^+=\Omega/St_{jet}$  the corresponding  $t_1^+=0.5/4\cdot 10^{-3}=125$ .

#### 3.3. Duty cycle and velocity ratio

The correlation between the duty cycle and the VR is investigated at a fixed frequency, f=50 Hz. The jet velocity levels were  $VR=1,\,2,\,3$  and 4, and the duty cycles are as in section 3.2.

Figure 13(a) shows, as expected, that higher VRs and longer duty cycles produce more control effect. If, instead, the variation of  $\Delta \overline{U}_5/VR^*$  with  $t_1^+$  is studied, as shown in figure 13(b), it is possible to identfy a maximum at  $t_1^+ = 100 - 150$  for VR = 2 and 3. For VR = 1 the jet velocity is too low to produce any vortices for  $\Omega < 0.85$  and thus its curve deviates from the other VRs. For VR = 4 it is not possible to establish a maximum, but the data do not contradict the optimum for VR = 2 and 3.

Note that  $VR^* = f dt_1^+/U_{inl}$  and since all parameters except  $t_1^+$  is constant the optimum  $t_1^+$  could be interpreted as an optimum  $VR^*$  of 0.5-0.75.

#### 3.4. Summary of previous results

In the above sections the influence of three different parameters on the control effect of pulsed VGJs have been investigated. In order to summarise the results all reported data is combined to produce the rather complex figure 14. The dashed lines ( $\Omega=0.5$ ) show that the variation with  $t_1^+$  is less pronounced when the duty cycle is kept constant.

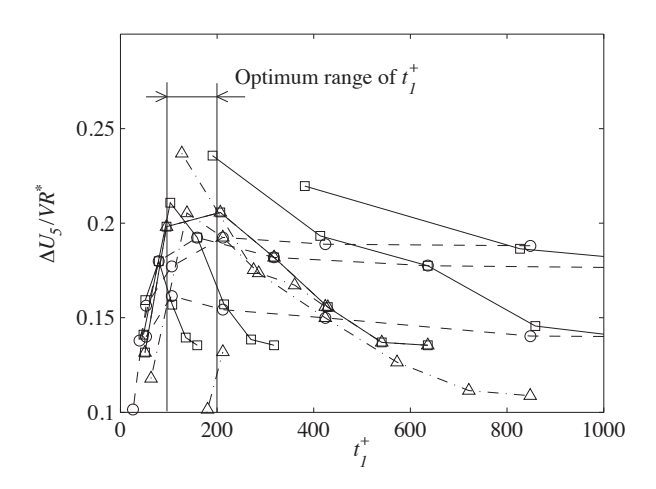


FIGURE 14. The data points from figure 10(b)  $(--\circ --)$ , figure 12  $(-\Box --)$  and figure 13(b)  $(-\cdot \triangle \cdot -)$  is combined.

#### 3.5. Yaw

For steady jets, it was shown in Lögdberg (2008) that the control effect decreases slowly for yaw angles up to  $\theta = 50^{\circ}$ .

In figure 15 the effectiveness of an array of VR=3 pulsed VGJs at yaw is shown compared to steady jets of the same VR. The steady jet is more effective due to its higher  $VR^*$ , but apart from that the main difference is a reduced influence of yaw for the pulsed jet. At  $\theta=40^\circ$  the effectiveness  $\Delta \overline{U}_5$  of the pulsed VGJs is still 86% of the value at  $\theta=0^\circ$ . For the steady jets it is 75%.

# 4. Discussion

The main conclusion from the reported experiments is that the basic mechanism of pulsed VGJs is pulse-width modulation. The control effectiveness is primary a function of  $VR^* = \Omega VR$ . Thus, for maximum effectiveness the duty cycle should be  $\Omega = 1$ . Figure 10(a) shows that the control effect of steady and pulsed jets is approximately the same for the same  $VR^*$ . However, the increase of  $\overline{U}_5$  with VR levels out at approximately the same VR. The existence of a maximum  $\overline{U}_5$  means that in order to achieve the maximum possible control effect from a given geometry the duty cycle should be  $\Omega = 1$ .

When maximum control effect is not necessary, pulsing is a convenient way to be able to run the VGJs at an efficient VR. In part 1 it was shown that for an array of steady jets VR = 0.85 is enough to prevent separation for the same APG boundary layer as here. It was also shown that VR = 2.5 is the most volume flow efficient VR. In figure 13(a) backflow is stopped for VR = 2 and VR = 3 at duty cycles of approximately 0.22 and 0.13, respectively. That

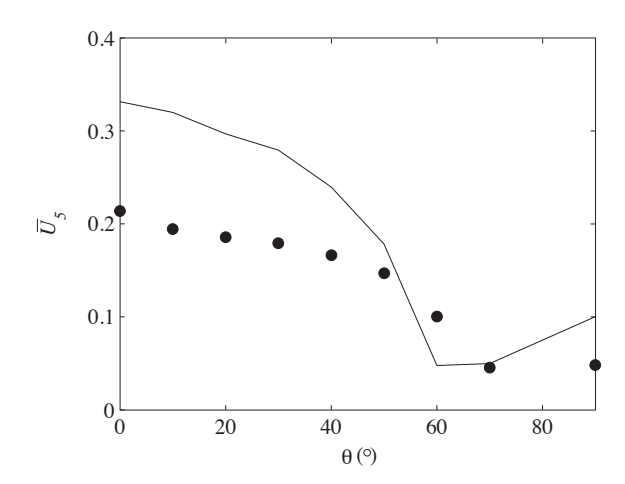


FIGURE 15. Effectiveness at different yaw angles. The circles show pulsed jets at  $VR=3,\ f=100$  Hz and  $\Omega=0.5$ . The line shows steady jet results at the same VR.

corresponds to  $VR^* \approx 0.4$ , which is about half of that for the steady jet.  $\overline{U}_5 = 0$  is not equivalent to attached flow, but the difference in required jet velocity is  $VR^* < 0.05$ .

For a given VR there is an optimum frequency. Real applications of pulsed VGJs should probably not be designed to run at the optimum Strouhal number of figure 10(b). That might produce a sensitive flow control system, due to the rapid decrease in control effect at frequencies higher than the optimum. Instead the optimum  $St_{jet}$  can be seen as a limit for a robust system.

For effectiveness, the optimum duty cycle is  $\Omega=1$ , but for volume flow efficiency there is no optimum  $\Omega$ . The relevant parameter is instead the injection time. In this experimental set-up the optimal injection time span is  $100 < t_1^+ < 200$ . The optimum  $St_{jet}$  mentioned above could also be expressed in  $t_1^+$ . Thus, there are only two non-geometry parameters that determines the efficiency: VR and  $t_1^+$ .

Johari & Rixon (2003) suggested that the optimal injection time for pulsed VGJs is in the range of 4–8  $d/U_{jet}$ . In the present experiment the optimal  $t_1$  has been shown to be approximately 25 times longer. No pulses as short as  $t_1^+ = 4 - 8$  have been tested here, but the trends in figures 12 and 13(b) do not look very promising. When the purpose of the actuators is to excite natural frequencies in the flow it is possible to employ shorter injection times. Then the injection times proposed by Johari & Rixon (2003) might be valid.

# Acknowledgements

This work is part of a cooperative research program between KTH and Scania  ${\rm CV}$ 

# References

- AMITAY, M., SMITH, D., KIBENS, V., PAREKH, D. E. & GLEZER, A. 2001 Aerodynamic flow control over an unconventional airfoil using synthetic jet actuators. *AIAA J.* **39**, 361–370.
- Bons, J. P., Sondergaard, R. & Rivir, R. B. 2001 Turbine separation control using pulsed vortex generator jets. *Transactions of ASME* 123, 198–206.
- BREMHORST, K. & HARCH, W. 1979 Turbulent shear flows I, chap. Near field velocity measurements in a fully pulsed subsonic air jet, pp. 37–54. Spinger Verlag, Berlin.
- Gharib, M., Rambod, E. & Shariff, K. 1998 A universal time scale for vortex ring formation. *J. Fluid Mech.* **360**, 121–140.
- Johari, H. & Rixon, G. S. 2003 Effects of pulsing on a vortex generator jet. AIAA J. 41, 2309–2315.
- Kostas, J., Foucaut, J. M. & Stanislas, M. 2007 The flow structure produced by pulsed-jet vortex generators in a turbulent boundary layer in an adverse pressure gradient. Flow Turbulence and Combustion 78, 331–363.
- LÖGDBERG, O. 2008 Separation control by an array of vortex generator jets. Part 1. Steady jet. Paper 4 in the present thesis.
- McManus, K., Ducharme, A., Goldey, C. & Magill, J. 1996 Pulsed jet actuators for surpressing flow separation, AIAA paper 96-0442.
- McManus, K., Joshi, P., Legner, H. & Davis, S. 1995 Active control of aerodynamic stall using pulsed jet actuators, AIAA paper 95-2187.
- McManus, K., Legner, H. & Davis, S. 1994 Pulsed vortex generator jets for active control of flow separation, AIAA paper 94-2218 .
- ORTMANNS, J., BITTER, M. & KÄHLER, C. J. 2006 Visualization and analysis of dynamic vortex structures for flow control applications by means of 3c2d-piv. In 12th international symposium on flow visualization, September 2006.
- Scholz, P., Casper, M., Ortmanns, J., Kähler, C. J. & Radespiel, R. 2008 Leading-edge separation control by means of pulsed vortex generator jets. AIAA J. 46, 837–846.
- Tillmann, C. P., Langan, K. J., Betterton, J. G. & Wilson, M. J. 2003 Characterization of pulsed vortex generator jets for active flow control. *Tech. Rep.*. Air Force Research Laboratory AFRL-VA-WP-TP-2003-336, Wright-Patterson Air Force Base.